MECHANICAL BEHAVIOUR OF AXIALLY COMPRESSED CIRCULAR CONCRETE-FILLED DOUBLE-SKIN STEEL TUBULAR STUB COLUMNS

Dissertation

Presented to Faculty of Engineering, Kanagawa University in Partial Fulfillment of the Requirements for the Degree of Doctor of Engineering

Submitted by

Xi-Feng Yan

Supervised by

Professor **Yan-gang Zhao**

CONTENTS

ACKNOWLEDGMENTS

I would like to first express my sincere gratitude to my advisor Professor Yan-gang Zhao. His support, encouragement and guidance help me to complete this research. I really appreciate his great patience to discuss with me when we have different opinions about the research. He taught me lots of valuable things, including the professional knowledge, hardworking attitude, and most importantly the way to be a better person. It is great honor to work with him and I would keep those things I have learned in mind and take them as my guideline for my future work.

I would like to express my deep gratitude to Professors Qingxuan Shi and Junfen Yang of Xi'an University of Architecture and Technology (China) for their support, encouragement and kindness over these years.

Special thanks go to assistant Professor Haizhong Zhang. He gave me a lot of useful help in solving the met difficulties. Without his patient help, it is almost impossible for me to get used to the life in Japan so smoothly.

Great thanks go to Professor Yazhou Xu of Xi'an University of Architecture and Technology (China), and Professor Jiongfeng Liang of East China University of Technology (China) for their company, help and kindness to me during their visit in Kanagawa University.

Great thanks go to the review committee members: Professor Mamoru Iwata, Professor Kazushi Shimazaki, Professor Enomoto Takahisa, and Professor Fujita Masanori for their valuable comments and suggestions on this work.

Sincere thanks go to the members of Zhao laboratory for their help in solving the met difficulties in life, work and study, etc.: Dr. Takasuke Saito, Dr. Siqi Lin, Dr. Ru Ren, Dr. Fangwen Ge, Dr. Peipei Li, Dr. Minna Tong, Dr. Xuanyi Zhang, Mr. Jianming Li, Miss Yexuan Yao, Mr. Lixiang Cheng, Mr. Sheng Wu. Specially, I would like to thank Mr. Zenta Hamaguchi, Mr. Shun Noribayashi, Mr. Rei Kuroiwa, and Mr. Kazuki Kuno for their great efforts in the experimental tests.

Finally, I would like to thank my family for their loves and selfness support, and myself for not giving up all these years.

Xi-Feng Yan
January, 2021

概要

コンクリート充填二重鋼管（以下 CFDST）とは、大小異なる径の 2 つの鋼管を同心円状に配置し、両鋼管の間にのみコンクリートを充填した構造形式である。CFDST はコンクリート充填鋼管（以下 CFT）に比べて軽量かつ圧縮強度の点で構造物に適応することによって、地震力が作用した際の自重による慣性力の低下と構造基礎部への負担の軽減を目的に研究が進められている。

今まで、円形 CFDST 柱の圧縮挙動を調べるための実験的研究を行って、円形 CFDST 柱の圧縮強度を予測するためにいくつかの設計モデルを提案した。しかし，高強度コンクリートまたは超高強度コンクリート充填平押し円形 CFDST 柱の実験の研究は非常に乏しかった。コンクリート強度の増加に伴い，コンクリートの有効利用率は脆性により低下することを示した。したがって，材料特性試験から得られたコンクリート強度を直接使用するのではなく，効果的なコンクリート強度を予測モデルに組み込む必要がある。その結果，材料特性試験から得られたコンクリート強度を取り入れた既存の経験モデルの適用性は疑わしい。また、円形 CFDST 柱に関する既存の研究は主に平押し CFDST 柱の軸圧縮性能である。しかし、これまでのところ、コンクリートのみに荷重を受ける CFDST 柱(中押し CFDST 柱)の挙動に関する利用可能な情報は非常に少ない。異なる載荷条件のために、中押し CFDST 柱の圧縮挙動は、平押し CFDST 柱のものと異なることがある。

円形 CFDST 柱に関するもう一つの重要な問題は軸方向荷重-ひずみ関係である。軸方向荷重-ひずみ関係を効率的に得るため，実験データに基づいていくつかのファイバ要素モデルを提案した。ファイバ要素モデルの精度は主に鋼と拘束コンクリートの適切な入力材料モデルに依存する。拘束コンクリートの圧縮強度モデルは，拘束コンクリートの応力-ひずみ関係の構成に重要な役割を果たしていることが示された。しかし，円形 CFDST 柱における拘束コンクリートの既存の圧縮強度モデルを提案し，限られた実験データに基づいて検証した。したがって、広い範囲のパラメータを有する CFDST 柱に対して既存のモデルの適用性は疑わしい。

平押しと中押し円形 CFDST 短柱の圧縮挙動を実験的及び数値的に検討した。CFDST 柱の荷重-変形関係を捕らえるため、一般的なファイバ要素モデルを提案した。主な結論は以下の通り：

1) 平押しと中押し円形 CFDST 短柱の圧縮挙動はいろいろな柱パラメータにより大きく影響される。

2) 中押し CFDST 柱におけるコンクリートの拘束効果は，平押し CFDST 柱よりも強いである。

3) 数値及び試験結果に基づいて，中押し CFDST 柱の圧縮強度を予測する新しいモデルを提案した。

4) 拘束コンクリートの拘束応力経路はいろいろな柱パラメータの変化により変化する、また，閉込め係数が小さい場合の拘束コンクリートの圧縮強度は，拘束応力経路に依存する。

5) 円形 CFDST 柱に対して CFDST 柱効果を考慮した拘束コンクリートの圧縮強度モデルを提案し，高い予測性能を見出した。

6) 平押し CFDST 柱の圧縮強度モデルを提案した。既設モデルと既往試験データに対する既存モデルとの比較は，提案モデルの予測精度を示した。

7) 平押し CFDST 柱の圧縮挙動を予測するため、新しいファイバ要素モデルを提案し、高い予測性能を見出した。

ABSTRACT

Concrete-filled double-skin steel tubular (CFDST) columns with concrete infilled between the two steel tubes not only possess the excellent performance of high stiffness, ductility and load-carrying capacity of concrete-filled steel tubular (CFST) columns, but also have lighter self-weight concerned by seismic design. They can be applied in the sea-bed vessels, legs of offshore platforms in deep water, bridge piers, and transmission tower.

Up to now, some experimental studies on circular CFDST columns have been conducted to investigate their compressive behaviour, and several empirical models were developed to predict the cross-sectional strengths of circular CFDST columns based on the limited experimental data. However, experimental studies on the axially loaded circular CFDST columns with high-strength concrete (HSC) or ultrahigh-strength concrete (UHSC) have been very scarce. It is shown that with the increase of concrete strength, the effective utilization rate of the concrete decreases due to its brittleness. Therefore, an effective concrete strength should be incorporated into the prediction models rather than directly using the concrete strength obtained from material property tests. As a result, the applicability of the existing empirical models incorporating the concrete strength obtained from material property tests is doubtful, and needs to be further assessed for a wider range of column parameters, e.g., HSC or UHSC. Additionally, existing researches on circular CFDST columns have mainly focused on the entire-section of columns under axial compression, however, so far, the available information about the behaviour of concrete axially loaded CFDST columns is very scarce. Owing to different loading conditions, the compressive behavior of concrete axially loaded CFDST columns may differ from that of the entire-section axially loaded ones, especially the confinement effect between the concrete and steel tubes.

Another important issue on circular CFDST columns is the axial load-deflection relationship, to efficiently obtain which, some fiber-beam element (FBE) models were empirically developed based on the experimental data. The accuracy of a FBE model depends mainly on the suitable input material models of the steel and confined concrete. It has been shown that the compressive strength model of confined concrete acts a vital role in the constitution of stress-strain relationship of confined concrete. However, existing compressive strength models of confined concrete in circular CFDST columns were developed and verified based on the limited experimental data (i.e., low concrete and steel strengths, etc..). Therefore, the applicability of these models for the CFDST columns with a wide range of column parameters, especially HSC or UHSC, is doubtful.

The compressive behaviour of the entire-section and concrete axially loaded circular CFDST short columns is experimentally and numerically investigated in this paper. A FBE model incorporating an effective concrete strength was developed for capturing the load-deflection relationships of CFDST columns. The following main conclusions are drawn:

1). The compressive behaviour of the entire-section and concrete axially loaded circular CFDST short columns is significantly affected by the column variables, such as the diameter-to-wall thickness ratios and yield strengths of external and internal steel tubes, concrete strength and hollow ratio.

2). The confinement effect of the concrete in the concrete axially loaded CFDST columns is stronger than that in the entire-section axially loaded CFDST columns.

3). Based on the numerical and test results, a novel formula was suggested to predict the ultimate

strength of the concrete axially loaded CFDST columns. Excellent agreement was found between the predicted strengths and numerical and test strengths.

4). The CSPs of confined concrete in the entire-section axially loaded CFDST columns were experimentally investigated. Results suggest that the CSPs vary with varying the column parameters, and the compressive strength of confined concrete in the column with a smaller confinement coefficient is CSP-dependent.

5). A compressive strength model of confined concrete considering the CSP effect was developed for circular CFDST columns, and high prediction performance is found for the developed model.

6). An ultimate strength model for the entire-section axially loaded CFDST columns, in which an effective concrete strength was introduced, was proposed. Comparison with existing models against the conducted and previous test data indicates a higher accuracy of the predictions for the proposed model.

7). A novel FBE model incorporating an effective concrete strength was developed to predict the compressive behavior of the entire-section axially loaded CFDST columns, which is found to be more accurate than the existing models.

CHAPTER 1. INTRODUCTION

1.1. Background

Concrete-filled double-skin steel tubular (CFDST) members consist of two concentric steel tubes with different diameters, and concrete filled in the annulus between them [1]. Such composite cross-sections not only hold the characteristics of the conventional concrete-filled steel tubes (CFSTs) counterparts, but also achieve lighter self-weight against their central cavity, higher flexural strength and better seismic resistance [2,3]. In addition, thanks to the internal tube being enclosed by external concrete, CFDST columns also possess excellent fire resistance [4]. Accordingly, they can be expected to achieve extensive applications in the sea-bed vessels, legs of offshore platforms in deep water, bridge piers, and transmission tower [5-7].

Various combinations of cross-sections have been declared in Ref. [1]. Of interest here are CFDST columns made of external and internal circular steel tubes, which are deemed to achieve a better confinement effect and ductility than those with other combinations [8,9]. In practical engineering, two items, i.e., the compressive capacity and load–deflection relationship of a CFDST column, are deeply concerned by engineers. Accordingly, several experimental and numerical investigations on circular CFDST columns have been performed by researchers to fully understand both items.

Up to now, some experimental studies on circular CFDST columns have been conducted to investigate their compressive behaviour, and several empirical models were developed to predict the cross-sectional strengths of circular CFDST columns based on the limited experimental data [1]. However, experimental studies on the axially loaded circular CFDST columns with high-strength concrete (HSC) or ultrahigh-strength concrete (UHSC) have been very scarce [1,10-14]. It is shown that with the increase of concrete strength, the effective utilization rate of the concrete strength decreases due to its brittleness. Therefore, an effective concrete strength should be incorporated into the prediction models rather than directly using the concrete strength obtained from material property tests. But, such effect has not been considered in the existing empirical models. As a result, the applicability of the existing empirical models is doubtful, and needs to be further assessed for a wider range of column parameters, especially HSC or UHSC. Additionally, existing researches on circular CFDST columns have mainly focused on the entire-section of columns under axial compression, however, so far, the available information about the behaviour of concrete axially loaded CFDST columns is very scarce [6]. Owing to different loading conditions, the compressive behavior of concrete axially loaded CFDST columns may differ from that of the entire-section axially loaded ones, especially the confinement effect between the concrete and steel tubes that determines the strength and ductility of columns. As a result, the existing empirical models for predicting the cross-sectional strengths of the entire-section axially loaded CFDST columns are incapable of predicting those of the concrete axially loaded CFDST columns accurately. Therefore, it is necessary to investigate the behavior of the concrete axially loaded CFDST columns, and propose a compressive capacity formula suitable for such columns for the purpose of engineering design.

Another important issue on circular CFDST columns is the axial load-deflection relationship, to efficiently obtain which, some fiber-beam element (FBE) models were empirically developed based on the individual experimental database [15,16]. The accuracy of a FBE model depends mainly on the suitable input material models of the steel and confined concrete. It has been shown that the

compressive strength model of confined concrete acts a vital role in the constitution of stress-strain relationship of confined concrete [16]. However, existing compressive strength models of confined concrete in circular CFDST columns were developed and verified based on the limited experimental data (i.e., low concrete and steel strengths, etc..). And as mentioned above, an effective concrete strength should be employed rather than directly using the concrete strength obtained from material property tests. Therefore, the reasonability of these models for the CFDST columns with a wide range of column parameters, especially HSC or UHSC, is doubtful. For well modelling the load-deflection relationships of CFDST columns under axial compression, a general compressive strength model of confined concrete should be developed and incorporated in the FBE model.

1.2. Objectives and organization

The objectives of this dissertation would be:

(1). To experimentally and numerically investigate the compressive behaviour of the entire-section and concrete axially loaded circular CFDST short columns, and ascertain the differences between their behaviours;

(2). To investigate the behaviour of the entire-section axially loaded CFDST short columns with HSC and UHSC, and probe into the effect of concrete strength on its effective utilization rate;

(3). To propose a FBE model for capturing the load-deflection relationship of CFDST columns considering the size effect and the effect of concrete strength on its effective utilization rate.

For the purpose, six chapters will be covered in this dissertation. The organization is given as follows:

In chapter two, a total of 28 the concrete axially loaded circular CFDST short columns was tested, based on which a finite element model was established to generate a wider range of parameters. Utilizing the test and numerical results, a novel formula for predicting the ultimate strength of CFDST columns was proposed.

In chapter three, a total of 28 the entire-section axially loaded circular CFDST short columns was tested, based on which a comparison was made to probe into ascertaining the differences between the compressive behaviour of the entire-section and concrete axially loaded CFDST columns.

In chapter four, the behaviour of the entire-section axially loaded CFDST short columns with HSC and UHSC was investigated, and a novel compressive capacity formula suitable for such columns with a wide range of column parameters was proposed.

In chapter five, a FBE model for modelling the load-deflection relationship of CFDST columns considering the size effect and the effect of concrete strength on its effective utilization rate was proposed.

In chapter six, the conclusions will be summarized.

References

[1] X.F. Yan, Y.G. Zhao, Compressive strength of axially loaded circular concrete-filled double-skin steel tubular short columns, J. Constr. Steel Res. 170 (2020) 106114.

[2] M.L. Lin, K.C. Tsai, Behavior of double-skinned composite steel tubular columns subjected to combined axial and flexural loads. In: Proceedings of the first international conference on steel and composite structures; (2001) 1145–1152.

[3] Y. Yagishita, H. Kitoh, M. Suimoto, T. Tanihira, K. Sonoda, Double skin composite tubular columns subjected to cyclic horizontal force and constant axial force. Conference proceedings of the 6th international conference on steel and concrete composite structures held in USA.

[4] R. Imani, G. Mosqueda, M. Bruneau, Finite element simulation of concrete-filled double-skin tube columns subjected to postearthquake fires, J. Struct. Eng. 141(12) (2015) 04015055.

[5] L.H. Han, H. Huang, Z. Tao, X.L. Zhao, Concrete-filled double skin steel tubular (CFDST) beam–columns subjected to cyclic bending, Eng. Struct. 28(12) (2006) 1698–1714.

[6] X.F. Yan, Y.G. Zhao, Experimental and numerical studies of circular sandwiched concrete axially loaded CFDST short columns, Eng. Struct. 230 (2021) 111617.

[7] W. Li, Q.X. Ren, L.H. Han, X.L. Zhao, Behaviour of tapered concrete-filled double skin steel tubular (CFDST) stub columns, Thin-Walled Struct. 57 (2012) 37–48.

[8] F.C. Wang, L.H. Han, W. Li, Analytical behavior of CFDST stub columns with external stainless steel tubes under axial compression, Thin-Walled Struct. 127 (2018) 756–768.

[9] L.H. Han, Q.X. Ren, W. Li, Tests on stub stainless steel-concrete-carbon steel double-skin tubular (DST) columns, J. Constr. Steel Res. 67(3) (2011) 437–452.

[10] S. Wei, S.T. Mau, C. Vipulanandan, S.K. Mantrala, Performance of new sandwich tube under axial loading: Experiment, J. Struct. Eng. 121(12) (1995) 1806–1814.

[11] X.L. Zhao, R.H. Grzebieta, M. Elchalakani, Tests of concrete-filled double-skin CHS composite stub columns, Steel Compos. Struct. 2(2) (2002) 129–146.

[12] X.L. Zhao, L.W. Tong, X.Y. Wang, CFDST stub columns subjected to large deformation axial loading, Eng. Struct. 32 (2010) 692-703.

[13] T. Ekmekyapar, H.G. Hasan, The influence of the inner steel tube on the compression behavior of the concrete filled double skin steel tube (CFDST) columns, Mar. Struct. 66 (2019) 197–212.

[14] T. Ekmekyapar, O.H. Alwan, H.G. Hasan, B.A. Shehab, B.J.M. Al-Eliwi, Comparison of classical, double skin and double section CFST stub columns: Experiments and design formulations, J. Constr. Steel Res. 155 (2019) 192-204.

[15] Z. Tao, L.H. Han, X.L. Zhao, Behavior of concrete-filled double skin (CHS inner and CHS outer) steel tubular stub columns and beam columns, J. Constr. Steel Res. 60(8) (2004) 1129–1158.

[16] Q.Q. Liang, Nonlinear analysis of circular double-skin concrete-filled steel tubular columns under axial compression, Eng. Struct. 131 (2017) 639–650.

CHAPTER 2. COMPRESSIVE BEHAVIOUR OF CIRCULAR SANDWICHED CONCRETE AXIALLY LOADED CFDST SHORT COLUMNS

2.1. Introduction

Concrete-filled steel tubular (CFST) columns as a member of composite components family are widely utilized in tall buildings and arch bridges, owing to their excellent structural properties, short construction period and low material cost [1-7]. In general, two concepts are commonly adopted for steel tube in CFST columns: (1) The steel tube and concrete core bear axial loads simultaneously, as shown Fig.2.1(a), resulting in the steel tube to be subjected to both longitudinal stress and lateral pressure stress from concrete expansion; (2) The steel tube is only subjected to lateral pressure from concrete expansion, that is, only core concrete is loaded to form a steel tube confined concrete (STCC), as shown Fig.2.1(b). It has been shown that the steel tube in a circular STCC column will provide more effective lateral confining pressure to concrete core. Also, previous studies demonstrated that STCC columns achieve better load-carrying capacity, ductility and energy dissipation owing to higher confinement efficiency compared to the entire-section loaded CFST columns [8-17]. Figs.2.2(a) to (b) show a schematic view of part of two types of CFST columns to steel (S) or reinforced concrete (RC) beam structural systems.

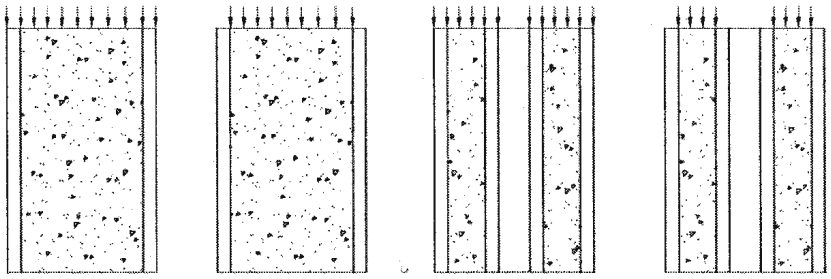

Fig.2.1 Loading modes of different columns

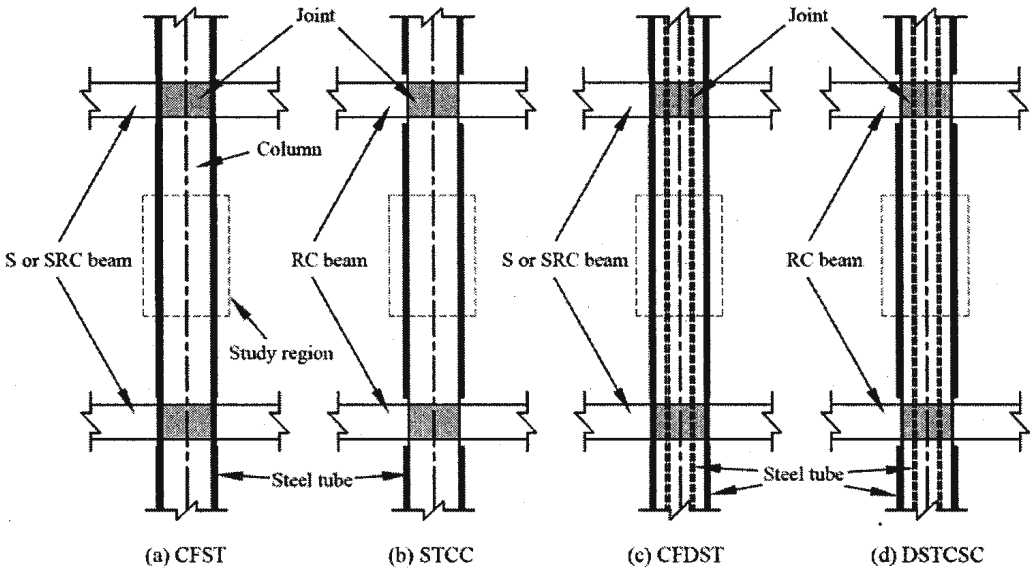

Fig.2.2 A schematic view of different columns to S or RC beam structural systems

However, with the development of high-rise building, long span and heavy load structures, columns with larger cross-sections are required, thus resulting in the frame structures to be too heavy and the foundation to bear excessive load, which is not conducive to seismic resistant design. To address this issue, concrete-filled double-skin steel tubes (CFDSTs) were proposed [18-20]. This type of columns is an innovative composite member filled concrete between the two skins and their center hollow portion offer an accessible dry space for installation. At the same time, outer and inner steel tubes can be used as formwork to facilitate the pouring of concrete. CFDST columns will be more conducive to seismic resistant design than conventional CFST counterparts owing to lower self-weight and convenient construction as well as higher ductility and energy absorption [19,21-23]. Also, previous studies found that the axial load-carrying capacity of such composite stub columns was 10%-30% higher in comparisons with the combined strengths of individual components [24-27]. Three components can work well together to undertake axial loads. The outer steel tube confined the sandwiched concrete well and an outward buckling occurred at the crushed location of concrete. Although the inner steel tube afforded insignificant confinement effect to the sandwiched concrete, it played a key role in compression, bending and shear resistance [19,21].

In general, the research on the compressive behaviour of axially loaded CFDST columns is an essential step to fully understand the mechanical behaviour under different load combinations [23,27]. The constitutive relationship of materials obtained in the study of the fundamental behaviour of short columns subjected to axial load will provide an important theoretical support for the analysis of columns with different loading conditions. Hence, the focus of this paper is on the fundamental behaviour of axially loaded CFDST short columns.

Thus far, however, almost all studies on axially loaded CFDST columns have focused on the entire-section of columns subjected to axial loads [23-39], as depicted in Fig. 1(c). Fig. 2(c) presents a schematic view of part of CFDST columns to S or SRC beam structural system [40,41]. Similar to CFST columns, owing to the outer steel tube bearing both longitudinal and transverse stresses, as a result, a relatively weak confinement efficiency to sandwiched concrete was generated [34]. In order to improve the lateral confinement efficiency of CFDST ones, a novel loading concept, i.e., only the concrete in CFDST columns bears axial load, is conceived by authors, as shown in Fig. 1(d). It is expected that this type of column combines the advantages of both STCC and entire-section loaded CFDST columns. A schematic view of part of concrete loaded CFDST columns to RC beam structural system is illustrated in Fig. 2(d).

Owing to different loading conditions, the compressive behavior of concrete axially loaded CFDST columns may differ from that of the entire-section axially loaded ones, especially the confinement effect between the concrete and steel tubes that determines the strength and ductility of columns. However, up to now, the available information about the behaviour of concrete axially loaded CFDST columns is very scarce. Farajpourbonab [42] employed finite element (FE) method to analyze the effects of different load application, geometry and material parameters on the behaviour of CFDST columns. Three types of load application, i.e., load on the entire section (LFE), load on the both steel tubes (LFS), and load on the sandwiched concrete (LFC), were briefly analysed. It should be noted that the FE models developed by Farajpourbonab were verified against the entire-section axially loaded CFDST columns previously tested. In addition, experimental study on the performance of concrete axially loaded CFDST columns has not been covered in the published literatures. Also, the influence of detailed parameters on the load-carrying capacity and ductility of

such columns is not very clear. Hence, to understand their compressive behavior, further studies on the concrete axially loaded CFDST columns are needed.

The current paper aims to experimentally and numerically investigate the behavior of circular sandwiched concrete axially loaded CFDST short columns. The rest of this paper is outlined as below: In Section 2, a comprehensive experimental investigation on the compressive behavior of CFDST columns, including 28 test specimens, was carried out. The key parameters varied in the experiments (e.g., the hollow ratio, concrete strength, diameter-to-thickness ratio and yield strength of the outer steel tube) were presented in detail. The test apparatus and procedures were also described. In Section 3, the test findings were briefly reported and analyzed. In Section 4, FE models were established and verified by comparing with the test results, and then an extensive parametric analysis was carried out to ascertain the influences of key variables on the compressive behaviour of the studied CFDST short columns. In Section 5, based on the numerical and test results, a novel formula was suggested to estimate the ultimate strength of CFDST columns. Finally, the conclusions were drawn in Section 6.

2.2. Experimental investigation

2.2.1. Test specimens

In total, 28 test experiments were performed to investigate the structural performance of concrete axially compressed CFDST short columns with circular outer and inner steel tubes. The four typical cross-sectional diagrams of CFDST columns were depicted in Fig.2.3. According to JIS G 3444-2015 [43], in this study, six different sectional sizes of circular hollow steel tubes were selected as the outer and inner skins. The STK400 steel tubes with the dimensions of 190.7 × 4.3 mm (diameter × thickness), 190.7 × 5.3 mm and 190.7 × 6.8 mm as well as the STK490 steel tubes with the dimensions of 190.7 × 5.3 mm were employed as the outer skins. The inner skins were STK400 steel tubes with the dimensions of 34.0 × 3.2 mm, 60.5 × 3.8 mm, and 101.6 × 4.2 mm, respectively. The tested specimens were poured using concrete with a nominal cylinder strength of 24 MPa, 36 MPa and 48 MPa. The ratio (L/D_o) of the nominal short column length-to-outside diameter of outer steel tube was maintained at a constant value of 3 to avoid overall buckling, and the nominal length of all specimens is taken as 570 mm [24]. Geometrical measurements were conducted, and the diameter and wall thickness of the cross-sectional size were measured by a Mitutoyo digital caliper. The measured results were listed in Table 2.1.

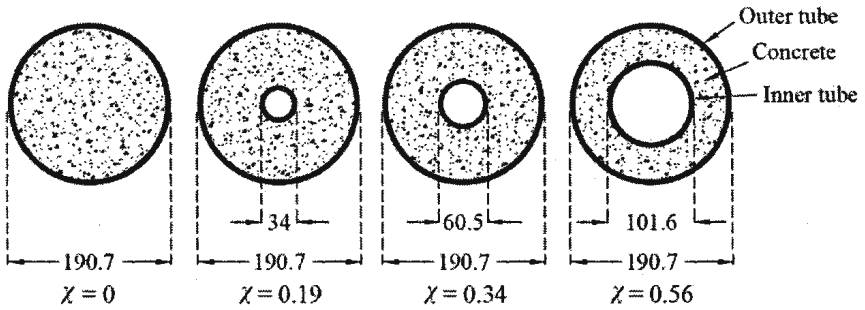

Fig.2.3 Typical cross-sections of specimens (unit: mm)

2.2.2. Specimen labeling

For simplicity, the tested CFDST columns were generally labelled as: section shape of columns, material grade of outer steel tube, nominal strength of concrete, hollow ratio, number of specimens and load condition. For instance, the label "C4-36-0.19-1C" defines the following specimen: The first

Table 2.1. Details of 28 tested circular CFDST short column specimens

Series	Specimens	$D_o \times t_o$ (mm × mm)	f_{syo} (MPa)	$D_i \times t_i$ (mm × mm)	f_{syi} (MPa)	χ	f_c (MPa)	DI	$N_{u,Exp}$ (kN)	$N_{u,Pro.}$ (kN)	$N_{u,FE}$ (kN)	$N_{u,Pro}$ /$N_{u,Exp}$	$N_{u,FE}$ /$N_{u,Exp}$
Series 1	C4-36-0-1C	190.1 × 5.11	46.9	0 × 0	0	0	37.5	3.08	2676	2612	2545	0.976	0.951
	C4-36-0-2C	190.0 × 5.13	346.9	0 × 0	0	0	37.5		2631	2615	2561	0.994	0.973
	C4-36-0.19-1C	189.1 × 5.10	346.9	34.0 × 3.08	348.2	0.19	37.5	3.10	2801	2686	2622	0.959	0.936
	C4-36-0.19-2C	190.1 × 5.11	346.9	33.9 × 3.10	348.2	0.19	37.5		2758	2679	2608	0.971	0.946
	C4-36-0.34-1C	190.5 × 5.15	346.9	59.6 × 3.32	342.1	0.34	37.5	3.58	2473	2545	2358	1.029	0.954
	C4-36-0.34-2C	188.2 × 5.04	346.9	59.1 × 3.28	342.1	0.34	37.5		2422	2469	2332	1.019	0.963
	C4-36-0.56-1C	190.7 × 5.11	346.9	101.6 × 4.03	345.8	0.56	37.5	6.29	1868	1827	1961	0.978	1.050
	C4-36-0.56-2C	189.2 × 5.0	346.9	101.2 × 4.05	345.8	0.56	37.5		1848	1790	1952	0.969	1.056
Series 2	C9-36-0-1C	190.2 × 5.13	464.0	0 × 0	0	0	37.5	5.69	3249	3181	3121	0.979	0.961
	C9-36-0-2C	190.0 × 5.10	464.0	0 × 0	0	0	37.5		3291	3166	3112	0.962	0.945
	C9-36-0.19-1C	188.9 × 5.09	464.0	33.7 × 3.09	348.2	0.19	37.5	5.62	3375	3218	3203	0.953	0.949
	C9-36-0.19-2C	188.9 × 5.12	464.0	33.5 × 3.06	348.2	0.19	37.5		3358	3229	3234	0.962	0.963
	C9-36-0.34-1C	191.0 × 5.15	464.0	59.4 × 3.31	342.1	0.34	37.5	6.53	3042	3132	2846	1.030	0.936
	C9-36-0.34-2C	190.1 × 5.11	464.0	59.1 × 3.29	342.1	0.34	37.5		2997	3097	2822	1.033	0.942
	C9-36-0.56-1C	190.7 × 5.15	464.0	101.1 × 4.10	345.8	0.56	37.5	6.70	2346	2247	2406	0.958	1.026
	C9-36-0.56-2C	190.7 × 5.09	464.0	100.9 × 4.07	345.8	0.56	37.5		2366	2240	2389	0.947	1.010
Series 3	C4-24-0.34-1C	190.4 × 5.15	346.9	59.9 × 3.33	342.1	0.34	29.0	6.04	2129	2347	2122	1.102	0.997
	C4-24-0.34-2C	190.0 × 5.11	346.9	59.1 × 3.31	342.1	0.34	29.0		2111	2335	2109	1.106	0.999
	C4-36-0.34-1C	189.1 × 5.10	346.9	59.4 × 3.35	342.1	0.34	37.5	3.09	2547	2502	2328	0.982	0.914
	C4-36-0.34-2C	190.1 × 5.07	346.9	59.7 × 3.35	342.1	0.34	37.5		2560	2514	2355	0.982	0.920
	C4-48-0.34-1C	189.9 × 5.12	346.9	58.9 × 3.31	342.1	0.34	51.0	1.97	2864	2835	2571	0.990	0.898
	C4-48-0.34-2C	188.6 × 5.08	346.9	58.9 × 3.33	342.1	0.34	51.0		2823	2791	2567	0.989	0.909
Series 4	C4-36-0.33-1C(4.3)	190.3 × 4.26	336.8	59.4 × 3.36	342.1	0.33	37.5	1.92	2133	2258	2073	1.058	0.972
	C4-36-0.33-2C(4.3)	190.1 × 4.21	336.8	59.3 × 3.30	342.1	0.33	37.5		2121	2241	2058	1.057	0.970
	C4-36-0.34-1C(5.3)	189.7 × 5.12	346.9	59.5 × 3.32	342.1	0.34	37.5	3.11	2473	2520	2390	1.019	0.966
	C4-36-0.34-2C(5.3)	188.8 × 5.08	346.9	59.5 × 3.31	342.1	0.34	37.5		2457	2489	2369	1.013	0.964
	C4-36-0.34-1C(6.8)	189.1 × 6.77	327.3	59.7 × 3.34	342.1	0.34	37.5	3.20	3067	2799	2560	0.913	0.835
	C4-36-0.34-2C(6.8)	188.6 × 6.73	327.3	59.8 × 3.33	342.1	0.34	37.5		3053	2776	2542	0.909	0.833
Mean value												0.994	0.955
Standard deviation (SD)												0.048	0.051
Coefficient of variation (CoV)												0.048	0.054

letter "C" means the circular section; number "4" refers to STK400 (and number "9" refers to STK490); number "36" after the first en dash indicates the nominal compressive strength of concrete, 36 MPa; number "0.19" after the second en dash denotes the hollow ratio of column. It should be noted that only the concrete in all tested specimens bears axial compression load, so the hollow ratio of the sandwiched concrete is used as that of column in this paper, and is computed by $D_i/(D_o-2t_o)$; number "1" after the third en dash symbolizes the first test body in the identical set of specimens; the last letter "C" indicates that only the concrete in the tested specimens bears axial compression load. The nominal wall thickness of outer steel tubes in Series 1 to 3 is identical and designed as 5.3 mm, which is not shown in the label. However, unlike other series, because the nominal wall thickness of outer steel tubes in Series 4 is variable, it is indicated in the mark.

Table 2.2. Material properties of external and internal skins

Type of steel	Location	Nominal sectional size (mm)	f_{sy} (MPa)	f_{su} (MPa)	E_s (GPa)	ε_f (%)
STK400	Internal skin	34.0 × 3.2	348.2	401.1	202.1	16.2
		60.5 × 3.8	342.1	406.4	199.6	18.8
		101.6 × 4.2	345.8	407.7	201.1	17.9
	External skin	190.7 × 4.3	336.8	398.8	198.9	18.4
		190.7 × 5.3	346.9	413.2	200.4	19.1
		190.7 × 6.8	327.3	383.9	203.7	17.3
STK490	External skin	190.7 × 5.3	464.0	524.8	197.9	13.1

Table 2.3. Mix design of concrete

Concrete grade	Water/cement ratio	Mix proportions (to the weight of cement)				
		Cement	Water	Fine aggregate	10 mm aggregate	Super plasticizer
C24	0.69	1.00	0.69	2.68	3.83	0.0091
C36	0.57	1.00	0.57	2.09	2.31	0.0012
C48	0.46	1.00	0.46	1.72	1.87	0.0034

Table 2.4. Measured strength of concrete cylinders

Nominal concrete strength (MPa)	Average concrete strength at 28 days (MPa)	Coefficient of variation (CoV)	Number of cylinder tests	Average concrete strength at test day (MPa)	Coefficient of variation (CoV)	Number of cylinder tests
C24	27.1	0.024	2	29.0	0.009	4
C36	34.7	0.008	2	37.5	0.032	4
C48	48.2	0.031	2	51.0	0.016	4

2.2.3. Material properties

The tensile coupon tests on external and internal tube skins were carried out to determine their material properties. The tensile coupons were longitudinally cut from the curved face of the circular hollow steel (CHS) tubes with the same parent material as the test specimens. The material properties of external and internal tube skins are listed in Table 2.2. In this table, f_{sy} represents the yield strength

of CHS tubes, and it is a general term, which is the same as the yield stress f_{syo} of the external tube skin and the yield stress f_{syi} of the internal tube skin; f_{su} denotes the ultimate tensile strength; E_o stands for the Young's modulus; ε_f symbolizes the elongation.

The material properties of the concrete used were determined by performing the standard concrete cylinder tests. According to the American Standard [44], the dimensions of concrete cylinder are 150 mm × 300 mm (diameter × height). The mix design of concrete used, which was achieved from commercially available materials, was listed in Table 2.3. At 28 days, six standard concrete cylinder specimens for C24, C36 and C48 were tested, and their strengths were 27.1 MPa, 34.2 MPa and 48.2 MPa with the coefficients of variation of 0.024, 0.008 and 0.031, respectively. The rest of specimens were tested together with the corresponding CFDST columns on the test day, and their strengths were 29.0 MPa, 37.5 MPa and 51.0 MPa for C24, C36 and C48, respectively, as shown in Table 2.4.

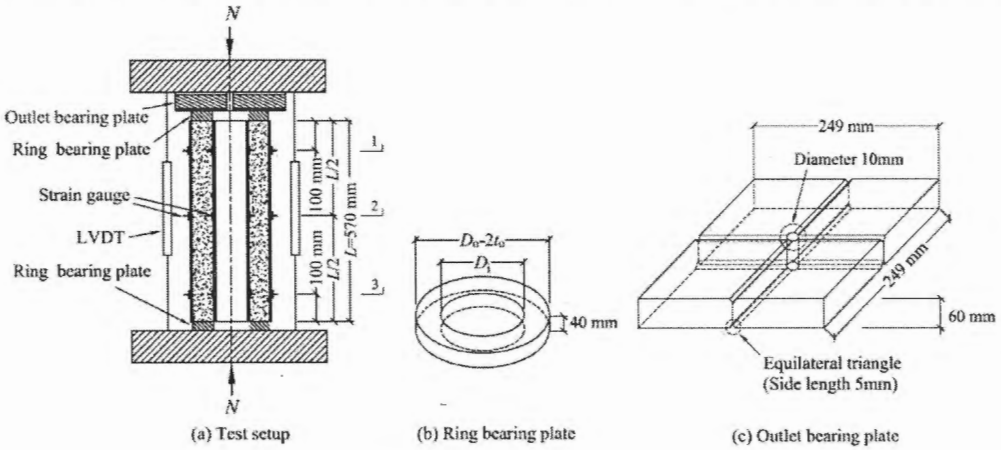

Fig.2.4 Schematics of the loading device

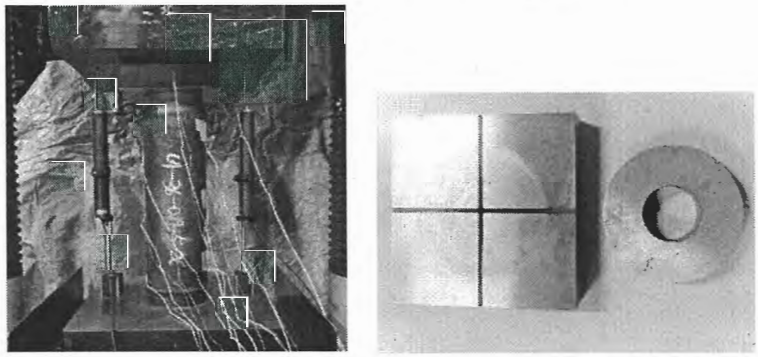

Fig.2.5 Test setup for tested CFDST specimen (e.g. C4-36-0.19-2C)

2.2.4. Column test procedures

All experimental tests were performed in Structural Materials Laboratory, Department of Architecture, Kanagawa University. The schematic diagram of the test apparatus was shown in Fig.2.4. A universal testing machine equipped with 5000 kN compression capacity was utilized for all the experiments. Fig.2.4(a) shows that axial compressive loads through the top and bottom ring bearing plates were applied to both ends of all the specimens. The design of the ring bearing plate with a thickness of 40 mm was illustrated in Fig.2.4(b). The inner diameter and outer diameter of the

ring bearing plate are equal to the outside diameter of the inner steel tube and to the inside diameter of the outer steel tube, respectively.

As shown in Fig.2.4(a), the bottom ring bearing plate is in direct contact with the bottom loading lam of the testing machine; however, there is an outlet bearing plate between the top ring bearing plate and the top loading lam. Through the trench and center hole in the outlet bearing plate, the data lines of the strain gauges pasted to the outside wall of the inner steel tube were pulled out for data collection. Twelve pairs of bidirectional strain gauges were pasted to the different positions of columns to obtain the corresponding longitudinal and transverse strains of outer and inner tube skins, as shown in sections 1, 2 and 3 in Fig.2.4(a). In addition, two LVDTs were used to monitor if the column was distorted in the loading plane during the test, and measure the axial deformation of the column. A data collection system was utilized to count changes in axial loads during the test process as well as the readings of LVDTs and strain gauges. The actual test setup was shown in Fig.2.5.

2.3. Test findings and analysis

2.3.1. Failure modes

From Figs.2.6(a) to 2.6(c), it can be found that the different degrees of shear failure were observed from the front view of the specimens with variable parameters owing to the crushing and cavity effect of the concrete. Fig.2.6(a) shows that the larger the hollow ratio, the more serious the diagonal shear failure. The outward plastic deformation occurred at different locations along the longitudinal direction mainly due to the uneven material density of concrete, which was caused by gravity. In addition, the failure degree of the columns fabricated by C4 steel tubes is more serious compared with that of columns using C9 ones. As shown in Fig.2.6(b), the concrete strength yields a negligible effect on the failure modes of the tested CFDST columns. However, for the different thicknesses (or diameter-to-thickness ratios) of outer steel tubes, different failure modes and scope were observed, as shown in Fig.2.6(c). This demonstrates that the yield stress and wall thickness of outer steel tube significantly affect the failure modes of the specimens.

In addition, the local failure modes of the selected specimens with different hollow ratios of 0.19, 0.34, and 0.56 were also reported and illustrated in Figs.2.7 to 2.9. From Figs.2.7(a), 2.8(a), and 2.9(a), it can be seen that, similar to the overall failure modes, the concrete generally occurs the outward plastic deformation in the form of the diagonal shear failure, and the failure degree becomes more pronounced as the hollow ratio gets larger. However, unlike the infilled concrete, the inner steel tubes in the specimens have almost no deformation, as illustrated in Figs.2.7(b), 2.8(b), and 2.9(b). The above observation indicates that the hollow ratio has an obvious effect on the failure modes of the outer steel tube and sandwiched concrete, but less significant effect on that of the inner steel tube.

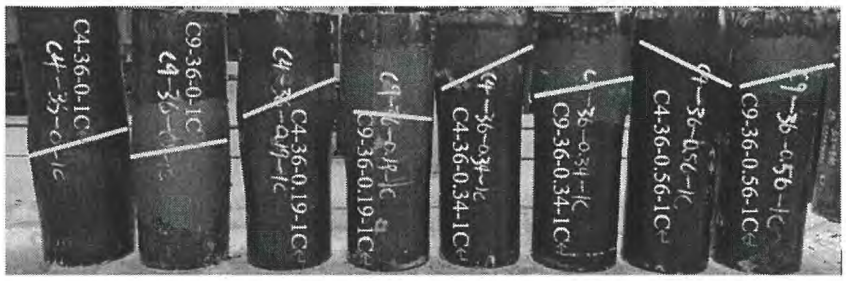

(a) Hollow ratio and yield strength of external skins

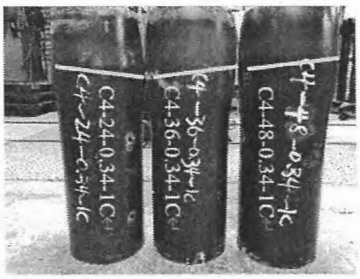

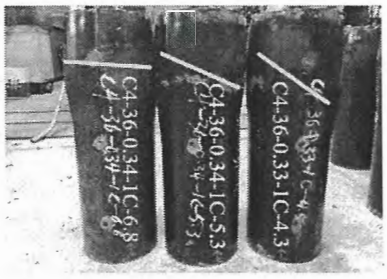

(b) Concrete grades (c) Thickness of external skins

Fig.2.6 Failure modes of the tested CFDST specimens

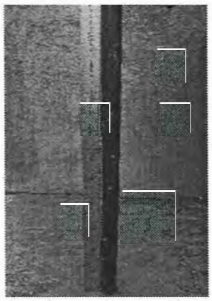

(a) Sandwiched concrete (b) Inner skin

Fig.2.7 Local failure modes of specimen C4-36-0.19-1C

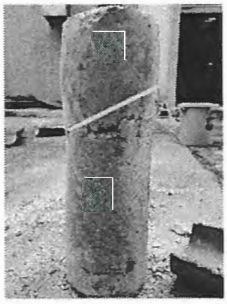

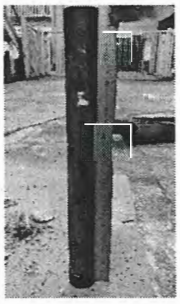

(a) Sandwiched concrete (b) Inner skin

Fig.2.8 Local failure modes of specimen C4-36-0.34-1C

(a) Sandwiched concrete (b) Inner skin

Fig.2.9 Local failure modes of specimen C4-36-0.56-1C

2.3.2. Load versus axial shortening relationship

The experimental load (N) versus axial shortening (ε) curves were illustrated in Fig.2.10. The effects of the various parameters on the initial stiffness and ductility behavior of the tested CFDST columns were discussed in this section. From Fig.2.10, it can be observed that the hollow ratio and

yield stress of outer steel tube yield an insignificant effect on the initial stiffness of columns, whereas the wall thickness of outer tube skin and concrete grade generate clear effects on the initial stiffness. As depicted in Fig.2.10(c), as the concrete strength increases from 24 MPa to 48 MPa, the initial stiffness is increased by 12.8%. While the wall thickness of outer tube skin changes from 4.3 mm to 6.8 mm, the initial stiffness of columns is improved by 39.2%. In addition, Figs.2.10(a) and 2.10(b) show that the residual strength in the post-peak segment of the tested specimens with the hollow ratio ranging from 0 to 0.34 slightly changes, whereas an obvious reduction is observed for the specimens with the hollow ranging from 0.34 to 0.56. This suggests that the hollow ratio has a significant effect on the residual strength, and the inflection point for the change in residual strength may be the hollow ratio of 0.34, which will be an important reference for seismic resistant design. Besides, with an increase in the wall thickness of outer tube skin and concrete grade, the residual strength in the post-peak range of the tested CFDST columns is improved by 16.7% and 50.8%, respectively. This indicates that the wall thickness of outer tube skin and concrete grade have an obvious effect on the residual strength.

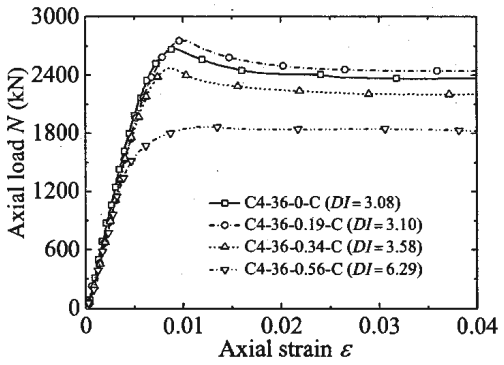

(a) Hollow ratio-STK400

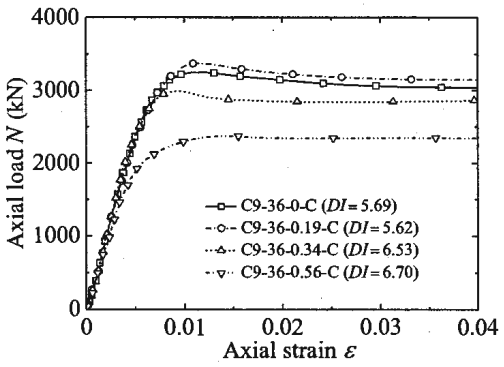

(b) Hollow ratio-STK490

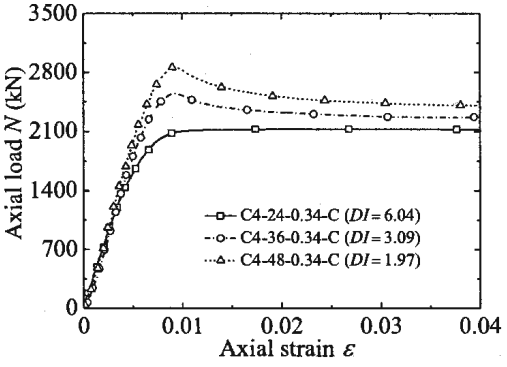

(c) Concrete strength

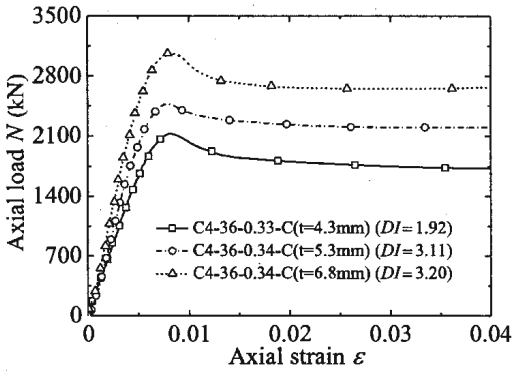

(d) Thickness of outer steel tube (D_o/t_o)

Fig.2.10 Experimental load (N) vs axial shortening (ε) curves

Moreover, the strain ductility index that differs from the displacement ductility index [27,45] is employed to evaluate the strain ductility of a CFDST column [39]:

$$DI = \varepsilon_u / \varepsilon_y \tag{2.1}$$

$$\varepsilon_y = \varepsilon_{0.75} / 0.75 \tag{2.2}$$

where ε_u symbolizes the axial strain of column when the axial load falls to 90% ultimate strength; $\varepsilon_{0.75}$ denotes the axial strain at the 75% ultimate strength before peak stage. For the load vs. axial shortening relationship with strain-hardening behaviour, the axial strain ε_u is specified as 0.04.

From Figs.2.10(a) and 2.10(b), it can be found that the ductility of the tested CFDST columns made by C4 and C9 outer steel tubes has no obvious change for the hollow ratio ranging from 0 to 0.19, while the ductility is increased by 102.9% and 19.2% respectively with the change of hollow ratio from 0.19 to 0.56. Moreover, for the hollow ratio 0, 0.19 and 0.34, the ductility of columns made by C9 outer steel tube is about 80% larger than that of ones made by C4 outer steel tube. However, the ductility of columns with the hollow ratio of 0.56, which is made by C9 outer steel tube, is only 6.5% greater than that of ones made by steel type C4. This finding shows that the hollow ratio and yield stress of outer steel tube have an obvious effect on the ductility of the tested CFDST columns. In addition, with the increase of concrete strength from 24 MPa to 36MPa and 48 MPa, the ductility of columns is decreased by 48.8% and 67.4%, respectively. For the wall thickness of outer tube skin ranging from 4.3 mm to 5.3mm and 6.8 mm, the ductility of columns is increased by 62.0% and 66.7%, respectively. This result demonstrates that wall thickness of outer tube skin and concrete grade affect significantly the ductility of the tested CFDST columns.

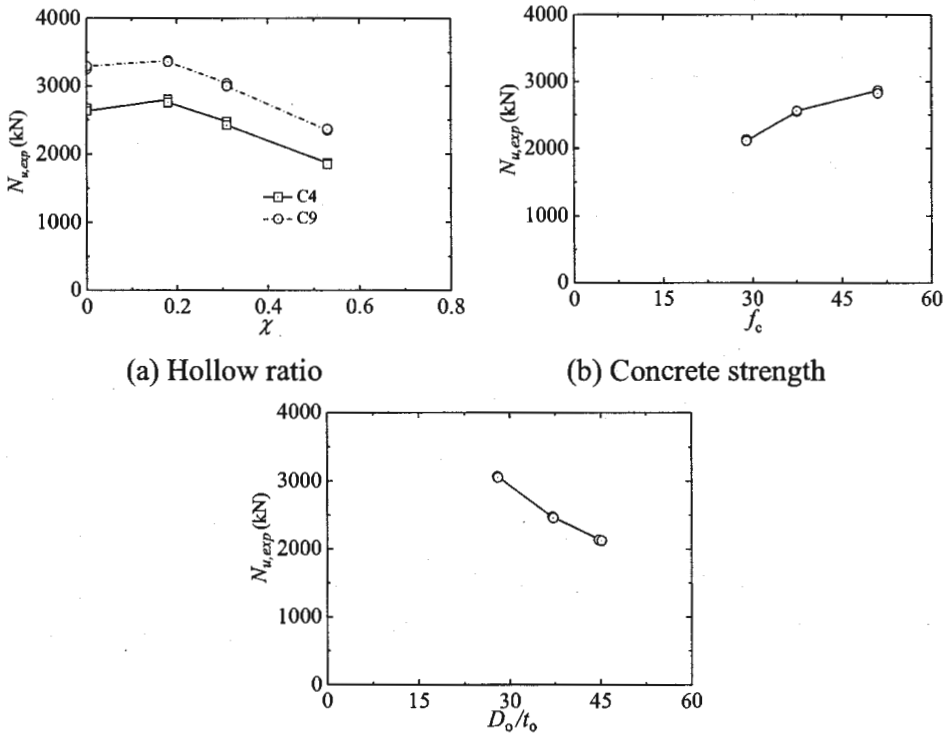

(a) Hollow ratio (b) Concrete strength

(c) Diameter-to-thickness ratio of external steel tube

Fig.2.11 Variations of the load capacities with key parameters

2.3.3. Load capacities

The ultimate strength of the tested CFDST specimens was listed in Table 1 and illustrated in Fig.2.11. In Fig.2.11 and Table 2.1, $N_{u,Exp}$ denotes the ultimate strength of the tested specimens, and C4 and C9 indicate that external tube skins of tested specimens that were made of C4 and C9 steel tubes, respectively. According to Fig.2.11(a) and Table 2.1, it can be found that the ultimate strength of the studied CFDST columns made by STK400 and STK490 steel tubes increases by about 4.7%

and 3.8%, respectively, with the increase of hollow ratio from 0 to 0.19. This may be due to the different confinement effect between the CFDST and STCC columns. As depicted in Fig.2.12, when the specimen C4-36-0.19-1C reaches the ultimate strength, and the corresponding axial strain is 10012 $\mu\varepsilon$, at when the lateral confining pressure of the outer and inner steel tubes is 7.8 MPa and 0.7 MPa, respectively. However, the axial strain of specimen C4-36-0-1C at the ultimate strength is 9109 $\mu\varepsilon$, at when the lateral confining pressure of the outer steel tube is 6.3 MPa. The lateral confining pressure of the outer steel tube in specimen C4-36-0.19-1C is 23.8% greater than that of specimen C4-36-0-1C. However, on the contrary, the ultimate strength of CFDST columns with the χ between 0.19 and 0.56 decreases with an increase in the hollow ratio. This is mainly due to the fact that the increased strength provided by the inner steel tube is less than the strength reduction caused by the reduction of concrete area. Moreover, it can be observed from Figs.2.11(b) and 2.10(c) that the ultimate strength of columns increases by 34.5% with the concrete strength increasing from 24 MPa to 48 MPa. However, as the diameter-to-thickness ratio of outer steel tube increases, the ultimate strength of columns decreases by 30.1%, which is mainly because increasing the diameter-to-thickness ratio of outer tube skin reduces its confinement effect on concrete.

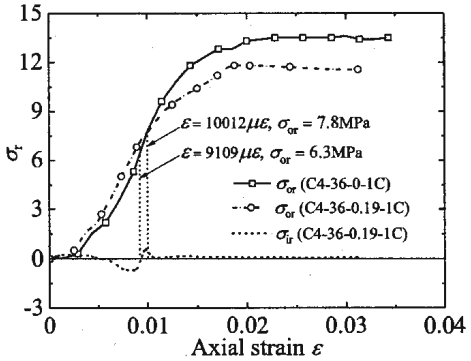

Fig. 2.12 Comparisons of the lateral confining stress for specimen C4-36-0-1C and C4-36-0.19-1C

Table 2.5 Comparisons of weights and capacities for specimens made by STK400 and STK490 outer steel tubes

Specimens	A_s (mm^2)	A_c (mm2)	Density (kN/m^3)		Weight (kg)	Capacity (kN)
			Steel	concrete		
C4-36-0-1C	2969.7	25413.0	76.9	25	0.864	2676
C4-36-0.19-1C	3247.3	24228.9	76.9	25	0.855	2801
C4-36-0.34-1C	3585.8	22713.6	76.9	25	0.844	2473
C4-36-0.56-1C	4214.7	17475.5	76.9	25	0.761	1868
C9-36-0-1C	2982.7	25429.9	76.9	25	0.865	3249
C9-36-0.19-1C	3236.4	24194.3	76.9	25	0.854	3375
C9-36-0.34-1C	3590.2	22874.0	76.9	25	0.848	3042
C9-36-0.56-1C	4251.5	17532.4	76.9	25	0.765	2346

In addition, it is assumed that the density of concrete is 25 kN/m^3 and the density of steel is 76.9 kN/m^3 [47], the weights and capacities of the specimens made by STK 400 and STK 490 outer steel tubes were compared against the test results and were listed in Table 2.5. From Table 2.5, it can be seen that the weights of the specimens decrease with an increase in the hollow ratio, whereas their capacities first increase and then decrease. The inflection point at which the load capacity changes is the hollow ratio of 0.19. The result suggests that in a certain range of hollow ratio, compared with

STCC columns, the concrete axially loaded CFDST columns not only achieve light weight, but also their load capacities are enhanced.

2.3.4. Typical load versus strain relationship at different sections

The axial load (N) versus strain (ε) curves at different cross-sections of the selected four typical CFDST columns were illustrated in Fig.2.13, where the strains were derived from the readings of strain gauges. ε_{yo} represent the corresponding strain (yield strain) at the yield stress of outer tube skin, and it is taken as $1946\mu\varepsilon$. The yield strain ε_{yi} of inner tube skin that is not depicted in Fig.2.13 is taken as $1932\mu\varepsilon$. For the definition of label, "O" and "I" represent the outside surface of outer and inner tube skins, respectively; "L" and "T" denote the capital initial letter of longitudinal and transverse strains, respectively; "numbers 1, 2 and 3" after the en dash indicate the different cross-sections, as shown in Fig.2.4. Fig.2.13(a) shows even if the contact surface between the steel tubes and concrete was coated with a thin layer of grease, the friction between them is inevitable, which causes the steel tubes to undertake a certain degree of axial stress. For example, for the outer steel tube of specimen C4-36-0-1C, the ratios of the longitudinal and transverse strains of section 1, 2 and 3 to yield strain are 2.68, 6.36, 5.83 and 4.05, 7.52, 7.48, respectively. And for the outer steel tube of specimen C4-36-0.19-1C, the ratios of the longitudinal and transverse strains of section 1, 2 and 3 to yield strain are 5.65, 12.33, 0.67 and 7.1, 13.88, 1.01, respectively. This indicates that section 2 (i.e., the mid-height section) for specimens C4-36-0-1C and C4-36-0.19-1C have a large deformation compared with other locations, which is consistent with the failed location observed in Section 3.1. However, the section 1 has a larger deformation than other sections for specimens C4-36-0.34-1C and C4-36-0.56-1C, of which their ratios of the longitudinal and transverse strains to yield strain are 10.28, 16.95 and 5.68, 7.78, respectively. It should be noted that in order to clearly distinguish the sections, a part of the strains in Figs.2.13(a-1), (b-1), (c-1) is beyond the scope of the horizontal axis, but their ratios to the yield strain are given as described above.

In addition, Figs.2.13(b-2), (c-2) and (d-2) show that the inner steel tubes of specimens C4-36-0.19-1C, C4-36-0.34-1C and C4-36-0.56-1C have a smaller strain that is located within the yield strain ($\varepsilon_{yi} = 1932\mu\varepsilon$). From Fig.2.12, it can be found that the lateral confining stress induced by the outer steel tube of specimen C4-36-0.19-1C has generated larger variety and is far from zero with an increase in the axial strain, whereas that of the inner steel tube is almost unchanged and is close to zero. This result confirms that the inner steel tube in the tested CFDST columns provide an insignificant lateral confining pressure on the infilled concrete in comparison with the outer steel tube.

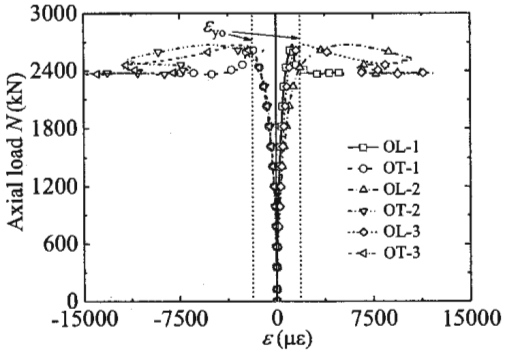

(a) C4-36-0-1C

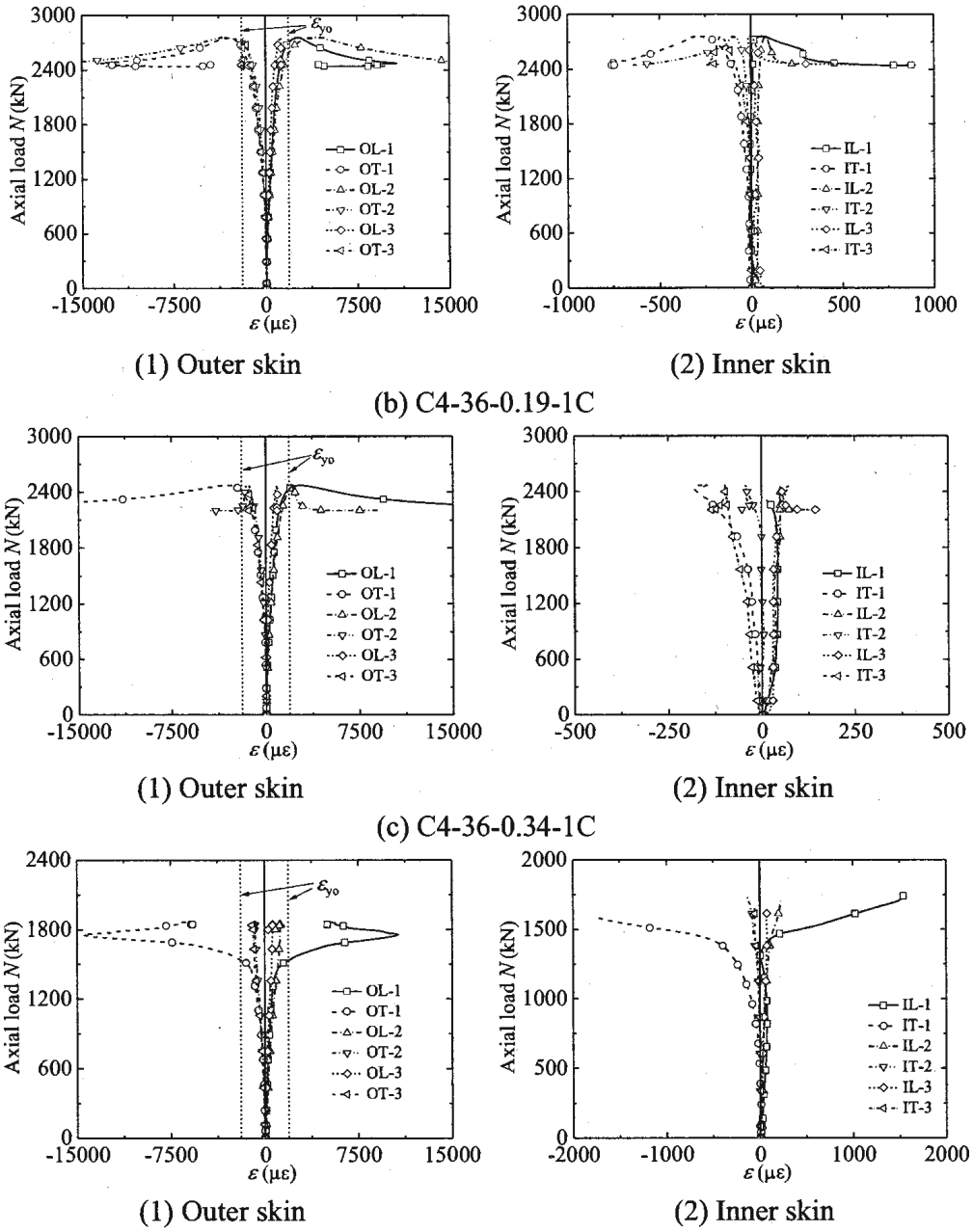

(1) Outer skin (2) Inner skin

(b) C4-36-0.19-1C

(1) Outer skin (2) Inner skin

(c) C4-36-0.34-1C

(1) Outer skin (2) Inner skin

(d) C4-36-0.56-1C

Fig.2.13 Typical load vs strain relation at different sections

2.3.5. Transverse-to-longitudinal strain ratios

As mentioned in the previous section, the lateral confining pressure induced by inner steel tube on the sandwiched concrete is almost negligible compared with that of outer steel tube. Therefore, in the current study, the degree of confinement afforded only by outer steel tube to the sandwiched concrete in CFDST columns with different hollow ratios is assessed by utilizing the transverse-to-longitudinal strain ratios from outer tube skin [48]. Herein, the strains used derived from the mid-height section of the column. Because the maximum deformation of specimens with the hollow ratio of 0.34 and 0.56 deviated from the mid-height section seriously, the specimens C4-36-0-1C and C4-36-0.19-1C were selected as the examples. The typical relations of the normalized axial load versus

mean transverse-to-longitudinal strain ratio were shown in Fig.2.14. It should be noted that the ratio of $N/N_{u,exp}$ starts from 0.01 rather than 0, mainly due to some uncontrollable factors in the initial loading phase, such as the gap between the tested specimens and the loading device.

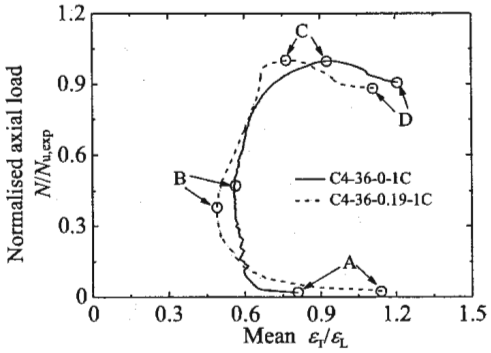

Fig.2.14 Relations of normalized axial load vs mean transverse-to-longitudinal strain ratio

From Fig.2.14, it can be seen that the initial strain ratios in point A may be approximately 0.8 for specimen C4-36-0-1C and 1.1 for specimen C4-36-0.19-1C in the early loading phase (i.e., $N/N_{u,Exp}=0.01$), respectively. This indicates that a certain confinement is generated by the outer steel tube and afforded to the infilled concrete at this stage. It is mainly due to the fact that, in the early loading phase, the effective Poisson's ratio of concrete in the tested specimens with only concrete axially loaded has already exceeded that of outer tube skin. As the axial shortening increases, a part of the axial load is transferred to the outer tube skin owing to the friction between the outer tube skin and infilled concrete. This gradually increases the axial deformation of the outer steel tube, which makes the strain ratio to decrease until point B, at which the $N/N_{u,Exp}=0.45$ and $\varepsilon_T/\varepsilon_L=0.6$ for specimen C4-36-0-1C, and the $N/N_{u,Exp}=0.37$ and $\varepsilon_T/\varepsilon_L=0.5$ for specimen C4-36-0.19-1C. With the maximum friction being reached and the development of concrete microcracks, the lateral expansion of outer tube skin is faster than the axial shortening due to the squeezing effect of concrete. This makes the strain ratio to increase from point B with an increase in the axial load. At this stage, the confinement induced by the outer tube skin on infilled concrete increases slowly. When the axial load reaches $0.9N_{u,Exp}$, the strain ratio increases rapidly until point C, at which the strain ratios of specimens C4-36-0-1C and C4-36-0.19-1C are 0.97 and 0.75, respectively. It's mainly at this time that the microcracks of concrete develop into macrocracks, which increases the transverse strain and enhances the lateral confinement. After point C, although an increase in strain ratio indicates a stronger confinement, the effective area of concrete gradually decreases owing to the development of macrocracks. This is the reason why the overall cross-sectional load capacity is reduced. The experimental tests were terminated until point D ($N/N_{u,Exp}=0.9$), where the strain ratios of specimens C4-36-0-1C and C4-36-0.19-1C are 1.24 and 1.1, respectively. The different strain ratios at point D indicate different confinement effect. This shows that, at this time, the confinement induced by the outer steel tube for specimen C4-36-0-1C on infilled concrete is slightly better than that of specimen C4-36-0.19-1C. In generally, increasing the mean transverse-to-longitudinal strain ratio is equivalent to increasing the confinement level.

2.4. Numerical modelling

In order to optimize the current test data pool, a comprehensive numerical study was conducted utilizing the general-purpose FE analysis package ABAQUS [46]. FE models were validated by comparing with the axial load-shortening curves, ultimate load and failure modes from the

experimental results. Using the verified FE models, an extensive parametric analysis was performed to further ascertain the effects of various parameters on the structural performance of circular concrete axially loaded CFDST stub columns.

2.4.1. Material modelling

(1) Carbon steel

An idealized multi-linear elastic-plastic stress-strain model suggested by Han et al. [49] as depicted in Fig.2.15 is adopted herein to model steel. This model is widely utilized by many researchers, such as Huang et al. [34], Wang et al. [37], Li et al. [38] and Yu et al. [50]. The stress-strain relationship of carbon steel suggested by Han et al. [49] is expressed by:

$$\sigma_s = \begin{cases} E_s\varepsilon & \varepsilon \le \varepsilon_1 \\ -A\varepsilon^2 + B\varepsilon + C & \varepsilon_1 \le \varepsilon \le \varepsilon_2 \\ f_{sy} & \varepsilon_2 \le \varepsilon \le \varepsilon_3 \\ f_{sy}\left[1+0.6\dfrac{\varepsilon-\varepsilon_3}{\varepsilon_4-\varepsilon_3}\right] & \varepsilon_3 \le \varepsilon \le \varepsilon_4 \\ 1.6f_{sy} & \varepsilon \ge \varepsilon_4 \end{cases} \tag{2.3}$$

where E_s and f_{sy} denote the elastic modulus and yield stress of the steel, and E_s is taken as 2.0×10^5 MPa; $A = 0.2f_{sy}/(\varepsilon_2-\varepsilon_1)^2$, $B = 0.2A\varepsilon_2$, $C = 0.8f_{sy} + A\varepsilon_1^2 - B\varepsilon_1$, $\varepsilon_1 = 0.8f_{sy}/E_s$, $\varepsilon_2 = 1.5\varepsilon_1$, $\varepsilon_3 = 10\varepsilon_2$, $\varepsilon_4 = 100\varepsilon_2$.

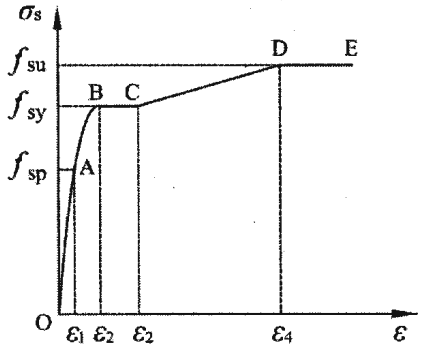

Fig.2.15 Stress (σ) - strain (ε) relationship for steel

(2) Concrete

The concrete material model developed by Han et al. [49] performed well in modeling the behavior of CFST members under various conditions, e.g., axial compression, torsion, bending and shearing. Yu et al. [50] confirmed that Han's model can be used to model the concrete in both CFST and STCC columns under axial compression. In addition, Huang et al. [34] and Li et al. [38] suggested that the passive confinement of concrete in CFST and CFDST columns shows insignificant difference, and Han's model [49] can be used to model the behaviour of concrete in CFDST columns. In this paper, the model for CFST columns is tentatively adopted and its expressions are given by:

$$\sigma_c = \begin{cases} 2x - x^2 & x \le 1 \\ \dfrac{x}{\beta_0(x-1)^\eta + x} & x > 1 \end{cases} \tag{2.4}$$

where $x = \varepsilon / \varepsilon_0$, $y = f / f_c$, ε denotes the axial strain of concrete at axial stress f; f_c denotes the standard concrete strength; ε_0 is the axial strain at which the stress f_c is reached; η and β_0 represent the parameters related to the section type. For circular section, η is taken as 2, and β_0 is expressed as below:

$$\beta_0 = 0.5\left(2.36\times10^{-5}\right)^{\left[0.25+(\xi-0.5)^7\right]}\left(f_c\right)^{0.5} \geq 0.12 \tag{2.5}$$

where ξ represents the nominal confinement factor.

In addition, the concrete damage plasticity model (CDPM) is employed in this paper, and the details of the CDPM can be found in Refs. [1,37,49].

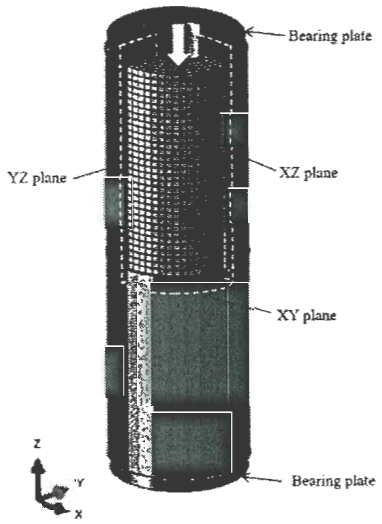

Fig.2.16 FE model in ABAQUS

2.4.2. Element, boundary condition and method of loading

Due to the symmetry of load and geometry of the studied CFDST short columns, only one eighth of column is modelled in this paper, as shown in Fig.2.16. In Fig.2.16, the 8-node linear brick elements with reduced integration (C3D8R) and shell elements (S4R) are adopted to model the sandwiched concrete and steel tube [33-34,38]. The element size for a circular section is taken as $D/20$ based on mesh convergence studies [36,37]. For boundary condition, the displacement of concrete and steel tubes in the normal direction of cutting YZ plane, XZ plane and XY, and the Z rotation of steel tubes are restricted. All free degrees of top surface of concrete are restricted except for longitudinal translation, and the top surfaces of outer and inner steel tubes are free. A uniform displacement instead of directly loading is applied to the top surface of concrete.

2.4.3. Contact modelling

In order to model the contact behaviors between the steel tubes and concrete, a surface-to-surface contact is employed. The inner surface of outer steel tube and the outer surface of inner steel tube are specified as the master surfaces, whereas the concrete surfaces in contact with the steel tubes are defined as slave surfaces. The Coulomb friction model incorporating a friction coefficient of 0.6 and hard-contact relation are employed in the tangent and normal directions [33,37,38].

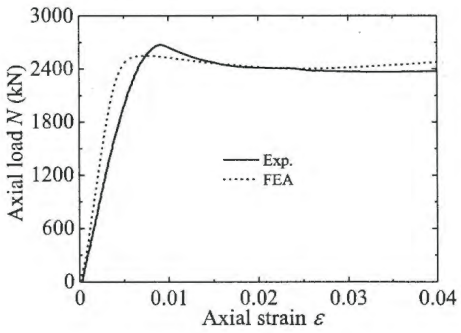

(a) C4-36-0-C

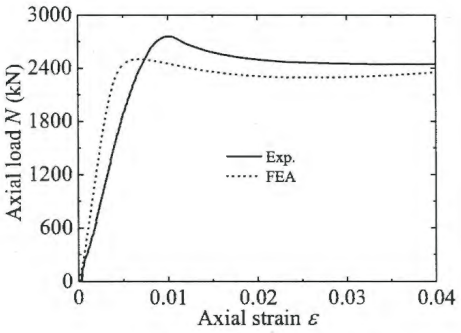

(b) C4-36-0.19-C

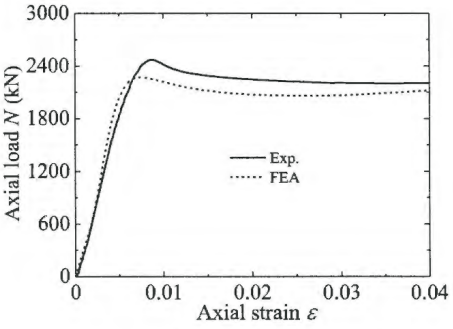

(c) C4-36-0.34-C

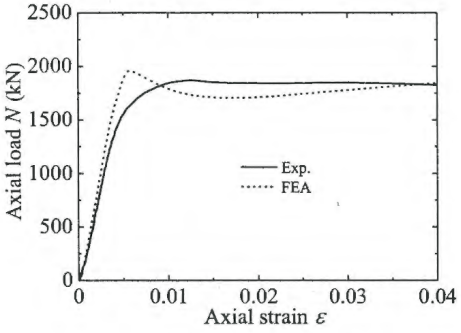

(d) C4-36-0.56-C

Fig.2.17 Comparisons of predicted and measured axial load N-shortening (ε) curves

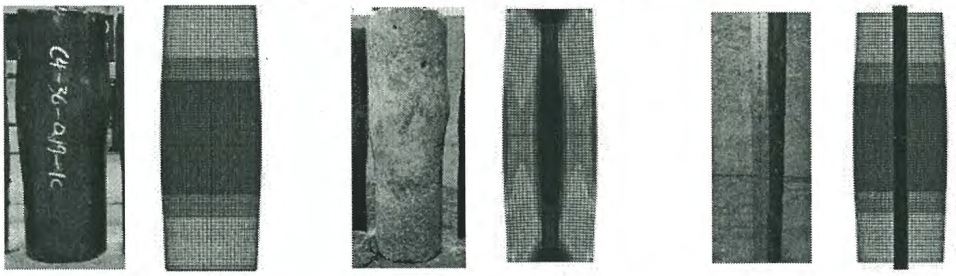

Outer steel tube Sandwiched concrete Inner steel tube

(a) C4-36-0.19-C

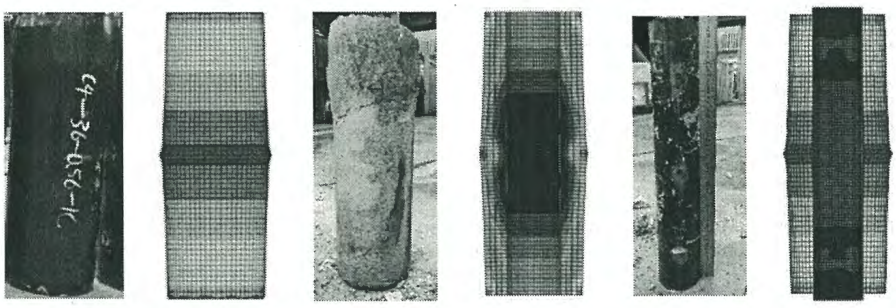

Outer steel tube Sandwiched concrete Inner steel tube

(b) C4-36-0.56-C

Fig.2.18 Comparisons of predicted and observed typical failure modes of specimens

Table 2.6. The details of parametric study

Parameters	$D_o \times t_o$ (mm × mm)	D_o/t_o	$D_i \times t_i$ (mm × mm)	D_i/t_i	f_{syo} (MPa)	f_{syi} (MPa)	f_c (MPa)	χ	DI	$N_{u,FE}$ (kN)	$N_{u,Pro.}$ (kN)	$N_{u,Pro.}/N_{u,FE}$
Yield stress of outer steel tube	300 × 6	50	145 × 6	24	275	275	50	0.5	1.78	4473	4474	1.000
	300 × 6	50	145 × 6	24	355	275	50	0.5	1.74	5078	5069	0.998
	300 × 6	50	145 × 6	24	460	275	50	0.5	1.81	5607	5849	1.043
	500 × 10	50	240 × 8	30	275	275	50	0.5	1.84	12341	12501	1.013
	500 × 10	50	240 × 8	30	355	275	50	0.5	1.86	14105	14163	1.004
	500 × 10	50	240 × 8	30	460	275	50	0.5	1.80	16292	16345	1.003
Yield stress of inner steel tube	300 × 6	50	145 × 6	24	275	355	50	0.5	1.77	4486	4474	0.997
	300 × 6	50	145 × 6	24	275	460	50	0.5	1.78	4499	4474	0.995
Compressive strength of concrete	300 × 6	50	145 × 6	24	275	275	30	0.5	2.21	3390	3502	1.033
	300 × 6	50	145 × 6	24	275	275	50	0.5	1.78	4473	4474	1.000
	300 × 6	50	145 × 6	24	275	275	70	0.5	1.52	5411	5447	1.007
	300 × 6	50	145 × 6	24	275	275	90	0.5	1.33	5845	6420	1.098
Hollow ratio	300 × 6	50	28 × 4	7	275	275	50	0.1	2.52	5457	5831	1.069
	300 × 6	50	86 × 4	22	275	275	50	0.3	2.42	5039	5547	1.101
	300 × 6	50	145 × 4	36	275	275	50	0.5	2.28	4254	4474	1.052
	300 × 6	50	201 × 4	50	275	275	50	0.7	1.97	3285	2643	0.805
Diameter-to-thickness ratio of outer steel tube	300 × 10	30	145 × 6	24	275	275	50	0.5	1.92	5436	5373	0.988
	300 × 6	50	145 × 6	24	275	275	50	0.5	1.78	4473	4474	1.000
	300 × 4.3	70	145 × 6	24	275	275	50	0.5	1.69	4001	4026	1.006
Diameter-to-thickness ratio of inner steel tube	300 × 6	50	145 × 9.7	15	275	275	50	0.5	1.75	4319	4474	1.036
	300 × 6	50	145 × 5.8	25	275	275	50	0.5	1.75	4292	4474	1.043
	300 × 6	50	145 × 4.1	35	275	275	50	0.5	1.73	4457	4474	1.004
Mean value												1.013
Standard deviation (SD)												0.063
Coefficient of Variation (CoV)												0.057

2.4.4. Verification of FE modelling

The established FE models are verified against comparing with the test results in terms of axial load vs. shortening curves, ultimate strengths and failure modes. The comparisons of axial load vs. shortening curves between FE modelling and experiments were depicted in Fig.2.17. From Fig.2.17, it can be found that FE models can almost replicate axial load-deformation histories of the tested specimens. A comparison of ultimate strengths between the FE modelling and experimental tests was listed in Table 2.1. The mean value of $N_{FE}/N_{u,exp.}$ is 0.955, with a standard deviation (SD) of 0.051 and a coefficient of variation (CoV) of 0.054. This indicates that the FE models perform well in predicting the axial shortening histories and ultimate strength of the tested CFDST columns. In addition, comparisons of failure modes between FE models and experimental tests were shown in Fig.2.18. From Fig.2.18, it can be observed that good agreements were achieved between numerical and test failure modes. It should be noted that that the failure modes of outer steel tube and concrete in the specimen C4-36-0.56-C deviated slightly from the mid-height section. This is mainly due to the uneven density of concrete caused by gravity, while FE modelling is difficult to simulate this situation. In general, the developed FE models can almost replicate the axial compression response and failure modes of the studied CFDST columns.

2.4.5. Parametric study

Utilizing the validated FE models, the effects of the key geometric parameters and material properties on the compressive behaviour of the studied CFDST columns are investigated. In this study, the variables investigated include the yield stresses and diameter-to-thickness ratios of outer and inner steel tubes, concrete strengths, hollow ratios. The details of the parametric study are listed in Table 2.6. The axial load (N) - axial strain (ε) curves of the calculated specimens are depicted in Fig.2.19 to Fig.2.24.

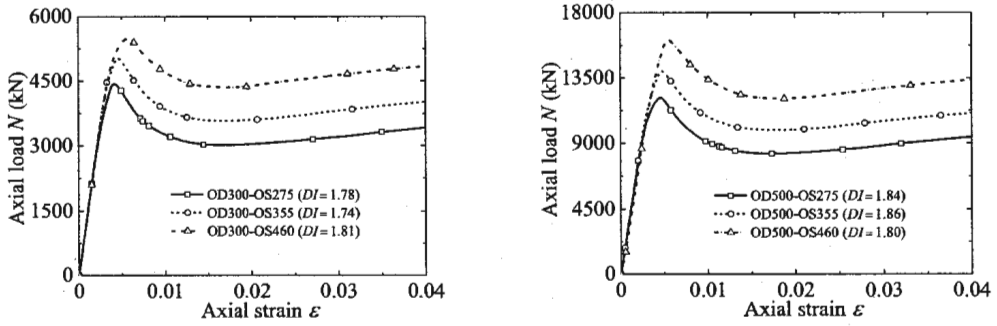

Fig.2.19 The effects of yield stress of outer steel tube on the behavior of CFDST columns

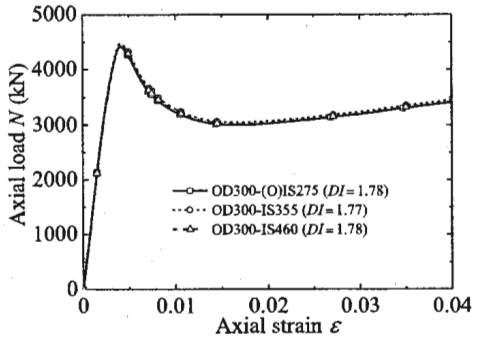

Fig.2.20 The effects of yield stress of inner steel tube on the behavior of CFDST columns

2.4.5.1. Effects of yield stresses of outer and inner steel tubes

Fig.2.19 and Fig.2.20 show the effects of yield stresses of outer and inner steel tubes on the N - ε curves of columns. In the two figures, the label 'OD300' denotes the diameter of outer steel tube is 300 mm, and the label 'OS275' and 'IS275' denote the yield stresses of outer and inner steel tubes are 275 MPa. Fig.2.19 shows that with the increase of yield stress of outer steel tube, the initial stiffness and ductility of columns have an insignificant change, but the ultimate strength is considerably improved. According to Table 2.6, the ultimate strength of columns with the outer tube diameter of 300 mm and 500 mm is increased by 25.4% and 32.1%, respectively, when the yield stress increases from 275 MPa to 460 MPa. This is mainly because the increase of steel strength increases the confinement effect of steel tube. However, from Fig.2.20, it can be found that the yield stress of inner steel tube yields an insignificant effect on the N - ε curves of columns. Therefore, the above finding suggests that the high-strength outer steel tube can be used to improve the ultimate strength of columns.

2.4.5.2. Effects of concrete strength

Fig.2.21 shows the effect of concrete strength on the N - ε curves of columns, and the corresponding ultimate strengths are listed in Table 2.6. According to Fig.2.21 and Table 2.6, it can be found that as the concrete strength increases from 30 MPa to 50 MPa, 70 MPa, and 90 MPa, the initial stiffness is increased by 34.5%, 55.6% and 72.1%, respectively, and the ultimate strengths are enhanced by 31.9%, 59.6% and 72.4%, respectively. However, the ductility of columns is reduced by 19.5%, 31.2% and 39.8%, respectively. This indicates that increasing the concrete strength can improve the initial stiffness and ultimate strength of the columns, but reduce the ductility.

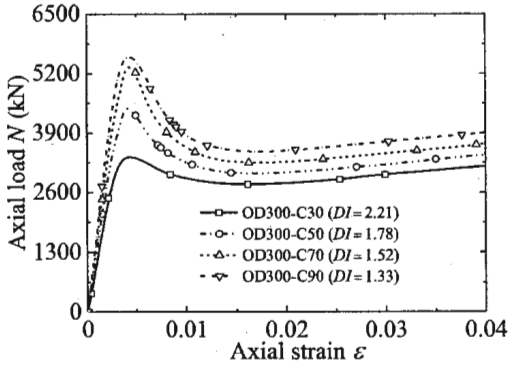

Fig.2.21 The effects of concrete strength on the behavior of CFDST columns

2.4.5.3. Effects of hollow ratio

Fig.2.22 presents the effect of hollow ratio on the N - ε curves of columns, and the corresponding ultimate strengths are listed in Table 2.6. In Fig.2.22, the label 'H0.1' denotes the hollow ratio of column is 0.1. From Fig.2.22, it can be seen that the initial stiffness and ultimate strength of columns are reduced by 47.9% and 39.8%, respectively, with the change of hollow ratio from 0.1 to 0.7. It is mainly because the inner steel tube provides less confinement effect to concrete, and the cross-sectional area of concrete is reduced with an increase in the hollow ratio. In addition, the ductility of columns is decreased by 4.0%, 9.5% and 21.8%, respectively, along with the hollow ratio varying from 0.1 to 0.3, 0.5 and 0.7. The above result suggests that the hollow ratio has an obvious effect on the axial response of the studied CFDST columns.

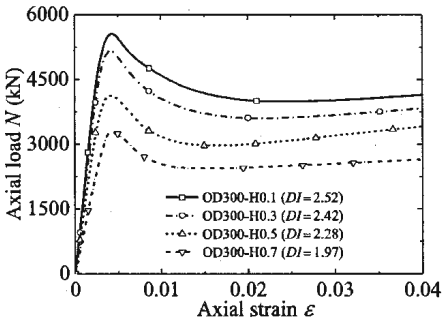

Fig.2.22 The effects of hollow ratio on the behavior of CFDST columns

2.4.5.4. Effects of diameter-to-thickness ratios of outer and inner steel tubes

Fig.2.23 and Fig.2.24 show the effects of diameter-to-thickness ratio of outer and inner steel tubes on the N - ε curves of columns, and the corresponding ultimate strengths are listed in Table 2.6. In Fig.2.23 and Fig.2.24, the label 'OR30' and 'IR15' represent the diameter-to-thickness ratios of outer and inner steel tubes are 30 and 15, respectively. According to Fig.2.23 and Table 2.6, it can be found that with the increase of diameter-to-thickness ratio of outer steel tube, the initial stiffness, ultimate strength and ductility of columns are reduced by 6.7%, 26.4% and 12.0%, respectively. This may be mainly due to the increase of diameter-to-thickness ratio of outer steel tube decreases the thickness and steel ratio, leading to a lower confinement efficiency. However, the diameter-to-thickness ratio of inner steel tube has an insignificant effect on the axial response of the studied CFDST columns. It is mainly because the inner steel tube provides less confinement effect on the concrete, as described in Section 3.3.

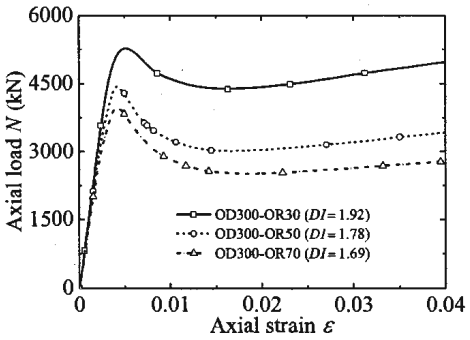

Fig.2.23 The effects of diameter-thickness ratio of outer tube skin on the behavior of CFDST columns

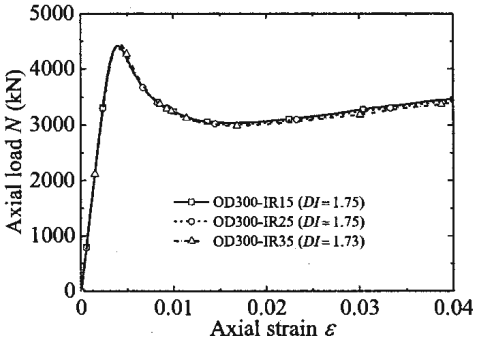

Fig.2.24 The effects of diameter-thickness ratio of inner tube skin on the behavior of CFDST columns

2.5. Proposed formula for the ultimate strength of CFDST columns

As mentioned in the literature review, up to now, there is little research on the concrete axially loaded CFDST members, resulting in no suitable design method for them. Thus, in current study, a novel formula for predicting the ultimate strength of such columns was proposed. Because only sandwiched concrete in CFDST columns bears axial load, in this paper, it is assumed that the ultimate strength of the studied CFDST columns can be determined by:

$$N_u = f_{cc} A_{sc} \tag{2.6}$$

in which f_{cc} denotes the strength of confined concrete, and A_{sc} symbolizes the area of sandwiched concrete. From Eq.(2.6), it should be noted that if f_{cc} is given, the ultimate strength of the studied CFDST columns will be obtained.

From the analysis results described in Section 3 and Section 4, it can be clearly seen that the ultimate strength N_u, (i.e., f_{cc} according to Eq.(2.6)) is mainly affected by the hollow ratio (χ), concrete strength (f_c), yield stress (f_{syo}) and diameter-to-thickness ratio (D_o/t_o) of outer steel tube. On the basis of the experimental and numerical results conducted in Section 3 and Section 4, a database was built. On the basis of nonlinear regression analysis of this database, an enhancement coefficient η_c is proposed to reflect the increase in concrete strength, and it can be expressed as a function of the various parameters such as χ, f_c, f_{syo} and D_o/t_o, as shown in the following equation:

$$\eta_c = \frac{f_{cc}}{f_c} = 1 + 7\left(1 - 2.5\chi^4 + 0.5\chi\right)\frac{t_o}{D_o}\frac{f_{syo}}{f_c} \tag{2.7}$$

It is easy to comprehend that when the hollow ratio $\chi = 0$, the η_c becomes

$$\eta_c = \frac{f_{cc}}{f_c} = 1 + 7\frac{t_o}{D_o}\frac{f_{syo}}{f_c} \tag{2.8}$$

where f_{cc} is referred as to the compressive strength of confined concrete in a circular STCC columns. This indicates that the Eq.(2.6), which incorporates the proposed η_c, can be also applicable for the strength prediction of STCC columns.

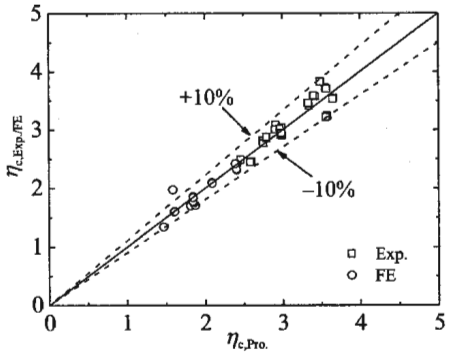

Fig.2.25 Comparisons of the proposed enhancement coefficient of concrete strength with test one

A comparison of the predictions by Eq.(2.7) with the numerical and test results was shown in Fig.2.25. It can be found from Fig.2.25 that excellent agreement is achieved between the proposed η_c and numerical and test results. In addition, comparisons of the strengths predicted by Eq.(2.6) and test and numerical strengths are shown in Table 2.1 and Table 2.6, respectively. From Table 2.1 and

Table 2.6, it can be found that the mean value of $N_{u,Pro.}/N_{u,Exp}$ is 0.994 with a SD of 0.048 and a CoV of 0.048, and the mean value of $N_{u,Pro.}/N_{u,FE}$ is 1.013 with a SD of 0.063 and a CoV of 0.057. In addition, a comprehensive comparison between the predicted strengths and strengths from numerical and test results is shown in Fig.2.26. From Fig.2.26, it can be seen that mean ratio of the predicted-to-numerical and test strengths is 0.1.002 with a SD of 0.053, which indicates that a high prediction performance is achieved in the proposed formula. Overall, the abovementioned investigation demonstrates that the proposed formula is not only suitable for estimating the ultimate strength of circular CFDST short columns, but can be also applied to estimate that of circular STCC ones.

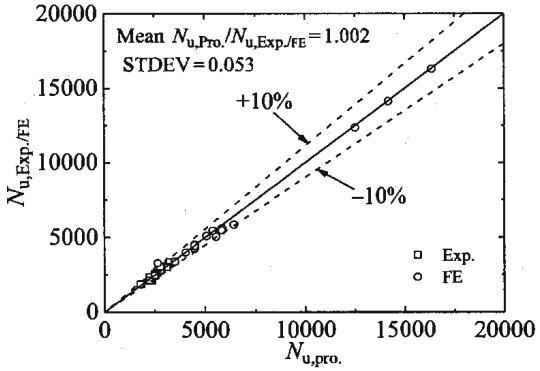

Fig.2.26 Comparisons of the proposed formula with test and numerical results

2.6. Conclusions

A comprehensive experimental and numerical studies on the behavior of the circular sandwiched concrete axially loaded CFDST short columns were conducted in the present paper. In total, 28 CFDST columns were loaded axially, of which the axial load vs. shortening curves, ultimate strengths and failure modes were briefly discussed. The obtained test results were utilized to verify the established FE models, and then an extensive parametric analysis was performed to further ascertain the effects of key variables on the behavior of the studied CFDST columns. Finally, depending on the numerical and test results, a novel formula was developed to estimate the ultimate strength of CFDST columns. The following conclusions can be drawn within the scope of this study:

(1) The concrete strength generates a negligible effect on the failure mode. With the increase of the wall thickness and yield stress of outer steel tube, the failure mode of the specimens gradually changes from diagonal shear failure to axial compression failure.

(2) The tested CFDST columns show good ductility performance similar to that of circular STCC columns.

(3) The ultimate strength of specimens with C9 outer steel tube is about 20% to 26% than that of ones with C4 outer steel tube. With an increase in the wall thickness of outer steel tube and concrete strength, the ultimate strength of specimens is improved by 32% and 43%, respectively. The ultimate strength of specimens first increases and then decreases with the increase of the hollow ratio. Generally, the concrete strength, wall thickness and yield stress of outer steel tube, and hollow ratio affect significantly the ultimate strength of columns.

(4) A material model suggested by Han et al. was adopted in this study to model the behavior of concrete in the concrete axially loaded CFDST columns. It can be found that established FE model can almost replicate the axial compression response and failure modes of the columns.

(5) Based on the numerical and test results, a novel formula was suggested to predict the ultimate strength of the studied CFDST columns. Excellent agreement was found between the predicted strengths and numerical and test strengths.

(6) The proposed formula can accurately predict the ultimate strength of concrete axially loaded CFDST short columns. By setting the hollow ratio as zero, it can be also applicable for the strength prediction of STCC short column.

References

[1] Y.G. Zhao, X.F. Yan, S.Q. Lin, Compressive strength of axially loaded circular hollow centrifugal concrete-filled steel tubular short columns, Eng. Struct. 201 (2019) 109828.

[2] L.H. Han, W. Li, R. Bjorhovde, Developments and advanced applications of concrete-filled steel tubular (CFST) structures: members, J. Constr. Steel Res. 100 (2014) 211–228.

[3] F.X. Ding, Q. Fu, B. Wen, Q.S. Zhou, X.M. Liu, Behavior of circular concrete-filled steel tubular columns under pure torsion, Steel Compos. Struct. 26(4) (2018) 501–511.

[4] H.B. Ge, T. Usami, Strength of concrete-filled thin-walled steel box columns: experiment, J. Struct. Eng. 118(11) (1992) 3036–3054.

[5] S.Q. Lin, Y.G. Zhao, L.S. He, Stress paths of confined concrete in axially loaded circular concrete-filled steel tube stub columns, Eng. Struct. 173 (2018) 1019–1028.

[6] S.Q. Lin, Y.G. Zhao, Numerical study of the behaviors of axially loaded large-diameter CFT stub columns, J. Constr. Steel Res. 160 (2019) 54–66.

[7] J.F. Yang, X.F. Yan, P.P. Hu, G.P. Zhang, Z.H. Xi, Study on the bending performance of cantilever concrete-filled circular steel tubular long columns, J. Xi'an Univ. of Arch. & Tech. (Natural Science Edition) 48(5) (2016) 654–660.

[8] Y. Sun, Proposal and application of stress-strain model for concrete confined by steel tubes, Proceeding of the 14th World Conference on Earthquake Engineering, October 12-17, 2008 (Beijing, China).

[9] L.H. Han, G.H. Yao, Z.P. Chen, Q. Yu, Experimental behavior of steel tube confined concrete (STCC) columns, Steel Compos. Struct. 5(6) (2005) 459–484.

[10] N.J. Gardner, E.R. Jacobson, Structural behavior of concrete-filled steel tubes, ACI Struct. J. 64 (7) (1967) 404–412.

[11] M. Tomii, K. Sakino, K. Watanabe, Y. Xiao, Lateral load capacity of reinforced concrete short columns confined by steel tube, Proceeding of the International Specialty Conference on Concrete Filled Steel Tubular Structures, ASCCS, 1985, pp. 19–26 Harbin, China.

[12] Y.G. Zhao, S.Q. Lin, Z.H. Lu, T. Saito, L.S He, Loading paths of confined concrete in circular concrete loaded CFT stub columns subjected to axial compression, Eng. Struct. 156 (2018) 21–31.

[13] Y. Orito, Y. Sato, N. Tanaka, K. Watanabe, Study on the unbonded steel tube concrete structure. Engineering Foundation Conf. on Composite Constructions, Henniker, New Hampshire, USA, (1987) 786–804.

[14] S.P. Schneider, Axially loaded concrete-filled steel tubes, J. Struct. Eng. 124(10) 1998 1125–1138.

[15]L.H. An, E Fehling, Numerical analysis of circular steel tube confined concrete (STCC) stub columns, J. Constr. Steel Res. 136 (2017) 238–255.

[16]M.D. O'Shea, R.Q. Bridge, Design of circular thin-walled concrete filled steel tubes, J. Struct. Eng. 126(11) (2000) 1295–1303.

[17]F. Huang, X Yu, B. Chen, The structural performance of axially loaded CFST columns under various loading conditions, Steel Compos. Struct. 13(5) (2012) 451–471.

[18]S. Wei, S.T. Mau, C. Vipulanandan, S.K. Mantrala, Performance of new sandwich tube under axial loading: Experiment, J. Struct. Eng. 121(12) (1995) 1806–1814.

[19]M.L. Lin, K.C. Tsai, Behavior of double-skinned composite steel tubular columns subjected to combined axial and flexural loads. In: Proceedings of the first international conference on steel and composite structures; (2001) 1145–1152.

[20]M. Elchalakani, X.L. Zhao, R. Grzebieta, Tests on concrete filled double-skin (CHS outer and SHS inner) composite short columns under axial compression, Thin-Walled Struct. 40(5) (2002) 415–441.

[21]Y. Yagishita, H. Kitoh, M. Suimoto, T. Tanihira, K. Sonoda, Double skin composite tubular columns subjected to cyclic horizontal force and constant axial force. Conference proceedings of the 6th international conference on steel and concrete composite structures held in USA.

[22]R. Imani, G. Mosqueda, M. Bruneau, Finite element simulation of concrete-filled double-skin tube columns subjected to postearthquake fires, J. Struct. Eng. 141(12) (2015) 04015055.

[23]L.H. Han, H. Huang, Z. Tao, X.L. Zhao, Concrete-filled double skin steel tubular (CFDST) beam-columns subjected to cyclic bending, Eng. Struct. 28 (2006) 1698–1714.

[24]X.F. Yan, Y.G. Zhao, Compressive strength of axially loaded circular concrete-filled double-skin steel tubular short columns, J. Constr. Steel Res. 170 (2020) 106114.

[25]X.L. Zhao, R. Grzebieta, Strength and ductility of concrete filled double skin (SHS inner and SHS outer) tubes, Thin-Walled Struct. 40 (2002) 199–213.

[26]F.Y. Wang, B. Young, L. Gardner, Experimental study of square and rectangular CFDST sections with stainless steel outer tubes under axial compression, J. Struct. Eng. 145(11) (2019) 04019139.

[27]Z. Tao, L.H. Han, X.L. Zhao, Behavior of concrete-filled double skin (CHS inner and CHS outer) steel tubular stub columns and beam columns, J. Constr. Steel Res. 60(8) (2004) 1129–1158.

[28]L.H. Han, Q.X. Ren, W. Li, Tests on stub stainless steel-concrete-carbon steel double-skin tubular (DST) columns, J. Constr. Steel Res. 67(3) (2011) 437–452.

[29]Y.F. Yang, L.H. Han, B.H. Sun, Experimental behavior of partially loaded concrete filled double-skin steel tube (CFDST) sections, J. Constr. Steel Res. 71 (2012) 63–73.

[30]K. Uenaka, H. Kitoh, K Sonoda, Concrete filled double skin circular stub columns under compression, Thin-Walled Struct. 48 (2010) 19-24.

[31]Y. Essopjee, M. Dundu, Performance of concrete-filled double skin circular tubes in compression, Compos. Struct. 133 (2015) 1276–1283.

[32]T. Ekmekyapar, H.G. Hasan, The influence of the inner steel tube on the compression behavior of the concrete filled double skin steel tube (CFDST) columns, Mar. Struct. 66 (2019) 197–212.

[33]F.Y. Wang, B. Yong, L. Gardner, Compressive testing and numerical modelling of concrete-filled double skin CHS with austenitic stainless steel outer tubes, Thin-Walled Struct. 141 (2019)

345–359.

[34] H. Huang, L.H. Han, Z. Tao, X.L. Zhao, Analytical behavior of concrete-filled double skin steel tubular (CFDST)stub columns, J. Constr. Steel Res. 66(3) (2010) 542–555.

[35] M. Pagoulatou, T. Sheehan, X.H. Dai, D. Lam, Finite element analysis on the capacity of circular concrete-filled double-skin steel tubular (CFDST) stub columns, Eng. Struct. 72 (2014) 101–112.

[36] M.F. Hassanein, O.F. Kharoob, Q.Q. Liang, Circular concrete-filled double skin tubular short columns with external stainless steel tubes under axial compression, Thin-Walled Struct. 73 (2013) 252–263.

[37] F.C. Wang, L.H. Han, W. Li, Analytical behavior of CFDST stub columns with external stainless steel tubes under axial compression, Thin-Walled Struct. 127 (2018) 756–768.

[38] W. Li, Y.X. Cai, Performance of CFDST stub columns using high-strength steel subjected to axial compression, Thin-Walled Struct. 141 (2019) 411–422.

[39] Q.Q. Liang, Nonlinear analysis of circular double-skin concrete-filled steel tubular columns under axial compression, Eng. Struct. 131(15) (2017) 639–650.

[40] W. Li, Y.F. Cheng, D. Wang, L.H. Han, X.L. Zhao, Behaviour of high-strength CFDST chord to CHS brace T-joint: Experiment, Eng. Struct. 219 (2020) 110780.

[41] J.F. Wang, L. Guo, Experimental and analytical behavior of square CFDST column blind bolted to steel beam connections, Int. J. Steel Struct. 20 (2020) 612–635.

[42] E. Farajpourbonab, Effective parameters on the behavior of CFDST columns, J. Applied Eng. Sci. 15(1) (2017) 99–108.

[43] JIS G 3444-2015. Carbon steel tubes for general structure. Japanese Standards Association, 2015 [In Japanese].

[44] ACI 318-11. Building code requirements for reinforced concrete. ACI Committee 318, Detroit (MI); 2011.

[45] E. Farajpourbonab, Development of a new steel section for reinforcing of steel-reinforced concrete-filled steel tubular columns, Struct. Concr. 20(2) (2019) 689–706.

[46] ABAQUS Standard User's Manual. The Abaqus Software is a product of Dassault Systemes Simulia Corp. Providence, RI, USA Dassault Systemes, Version 6.8, USA, 2008.

[47] AS/NZS 1170.1:2002. Structural design actions Part 1: Permanent, imposed and other actions, Sydney, New South Wales, Australia: Standards Australia; 2002.

[48] B. Uy, Z. Tao, L.H. Han, Behavior of short and slender concrete-filled stainless steel tubular columns, J. Constr. Steel Res. 67(3) (2011) 360–378.

[49] L.H. Han, G.H. Yao, Z. Tao, Performance of concrete-filled thin-walled steel tubes under pure torsion, Thin-Walled Struct. 45 (2007) 24–36.

[50] Q. Yu, Z. Tao, W. Liu, Z.B. Chen, Analysis and calculations of steel tube confined concrete (STCC) stub columns, J. Constr. Steel Res. 66(1) (2010) 53–64.

CHAPTER 3. COMPRESSIVE BEHAVIOUR OF CIRCULAR ENTIRE-SECTION AXIALLY LOADED CFDST SHORT COLUMNS

3.1. Introduction

Concrete-filled steel tubes (CFSTs) are widely employed in various modern building structures, especially in high-rise buildings, owing to their excellent structural performance, which includes large energy-absorption capacity, high ductility and stiffness [1–5]. To achieve the purpose of narrowing the weight of CFST column without affecting its load-carrying capacity, concrete-filled double skin steel tubes (CFDSTs) were developed [6–7]. It has been reported that CFDSTs not only share the characteristics of CFSTs, but also supply a possible dry space for facilities depending on their hollow portion.

Several section types have been declared in Ref. [2], as shown in Fig. 1. Of interest here are circular CFDST columns (both inside and outside skins are circular steel tubes), which are deemed to achieve a better confinement effect and ductility than CFDST columns with other cross-section combinations [8–10].

In practical engineering, two items, i.e., the compressive capacity and load–deformation relationship of a CFDST column, are deeply concerned by engineers. Accordingly, several experimental and numerical investigations on CFDST columns with the entire section axially compressed have been conducted by researchers. Zhao et al. [11-12], Han et al. [13,23], Tao et al. [14-15], Uenaka et al. [16], Essopjee and Dundu [17], Ekmekyapar and Hasan [18], and Wang et al. [24] experimentally investigated the effects of different sectional dimensions and combinations on the strength and ductility of CFDST columns in bending or compression, and developed the corresponding strength prediction models. Huang et al. [8], Wang et al. [10], Li and Cai [19], Hu and Su [20], Hassanein and Kharoob [21], Liang [22], and Hassanein et al. [25] numerically investigated the effects of the key variables on the strength and ductility of circular CFDST columns concentrically compressed by using the ABAQUS software [26]. The above investigations have indicated that a well-established compressive strength model of confined concrete is of critical importance to accurately estimate the compressive capacity and load–deformation relationship of the CFDST columns.

So far, many researchers have made a lot of contributions to compressive strength models of confined concrete, of which the models of Richard [27] and Mander [28] are widely used in the research of fiber-reinforced polymer (FRP) confined concrete and CFST columns [29-30]. Incorporating the confinement effect of internal tube, the modified models of Richard [27] and Mander [28] are adopted in the analysis of the CFDST columns [20-21,25]. It should be noted that such models are developed based on the experimental tests of actively confined concrete, in which specimens are exposed to a constant hydrostatic lateral confining pressure. However, the concrete in CFDST columns is in passive confinement state, thus it undergoes rising lateral confining stress with the increase of axial compressive stress. Here, the relationship between the lateral confining stress and axial compressive stress is called the confining stress path (CSP) of concrete [29-30].

Previous investigations have shown that the confining stress paths (CSPs) of confined concrete significantly affected the compressive behavior of confined concrete in fiber-reinforced polymer (FRP) confined concrete or CFST columns [29-30]. Unlike the concrete in FRP-confined concrete or CFST columns, which is only confined by external materials, e.g., FRP sheet or steel tube, the

concrete in concrete-filled double-skin steel tubular CFDST columns is confined by both the external and internal steel tubes. Due to different confinement mechanisms, the CSPs of confined concrete in CFDST columns may be different from those in FRP-confined concrete or CFST ones, which, however, have not been investigated so far. Therefore, in this paper, the CSPs of confined concrete in circular entire-section axially loaded CFDST stub columns were experimentally investigated, and their corresponding influences on the compressive strength were also discussed.

Additionally, owing to different loading conditions, the compressive behavior of the concrete axially loaded CFDST columns may differ from that of the entire-section axially loaded ones, especially the confinement effect between the concrete and steel tubes that determines the strength and ductility of columns. In order to well understand the behaviour of concrete axially loaded CFDST columns, Farajpourbonab [31] employed finite element (FE) method to analyze the effects of different load application, geometry and material parameters on the behaviour of CFDST columns. Three types of load application, i.e., load on the entire section (LFE), load on the both steel tubes (LFS), and load on the sandwiched concrete (LFC), were briefly analysed. It should be noted that the FE models developed by Farajpourbonab were verified against the entire-section axially loaded CFDST columns previously tested. Recently, Yan and Zhao [7] experimentally and numerically investigated the behavior of the circular sandwiched concrete axially loaded CFDST short columns. Based on the numerical and test results, a novel formula was suggested to estimate the ultimate strength of CFDST columns.

Generally, the above studies only present the individual compressive behaviour of the entire-section and sandwiched concrete axially loaded CFDST short columns, respectively. However, up to now, research on the comparison between them is very scarce. Therefore, this paper aims to experimentally and numerically investigate the behaviour of circular CFDST stub columns under axial loading conditions. This paper is organized as below: In Section 2, the comprehensive experimental tests on the behavior of the entire-section axially loaded CFDST columns, including 28 test specimens, were carried out. The test findings were briefly reported and analyzed; In Section 3, comparison between the compressive behaviours of the entire-section and sandwiched concrete axially loaded CFDST stub columns was made based on the experimental and numerical results; In Section 4, the CSPs of confined concrete in circular entire-section axially loaded CFDST stub columns were experimentally investigated.

3.2. Experimental investigation on the entire-section axially loaded CFDST columns

3.2.1. Test specimens and procedure

In total, 28 the entire-section concentrically compressed CFDST short columns fabricated using both outer and inner circular carbon steel tubes were tested in this section, and the details of the tested specimens were shown in Table 3.1. The specimens were divided into four batches to discuss the effects of key parameters on the compressive behaviour of circular CFDST short columns. The specimens in batches 1 and 2 were utilized to analyze the effects of the hollow ratio and yield strength of external steel tube, and those in batches 3 and 4 were employed to study the effects of the concrete strength and ratio of outer steel tube diameter to wall thickness, respectively.

In order to achieve a result as accurate as possible, each type of circular CFDST short columns consisted of two identical specimens. The outer steel tube has a nominal diameter (D_o) of 190.7 mm

Table 3.1. Details of 28 tested circular CFDST short column specimens

Batches	Specimens	$D_o \times t_o$ (mm × mm)	D_o/t_o	f_{syo} (MPa)	$D_i \times t_i$ (mm × mm)	D_i/t_i	f_{syi} (MPa)	χ	f_c (MPa)	$N_{u,Exp}$ (kN)	$N_{u,FE}$ (kN)	$N_{u,FE}/N_{u,Exp}$
Batch 1	C4-36-0-1E	190.1 × 5.11	37.2	346.9	0 × 0	/	0	0	37.5	2396	2299	0.960
	C4-36-0-2E	190.0 × 5.13	37.0	346.9	0 × 0	/	0	0	37.5	2344	2299	0.981
	C4-36-0.19-1E	189.1 × 5.10	37.0	346.9	34.0 × 3.08	11.0	348.2	0.19	37.5	2718	2589	0.953
	C4-36-0.19-2E	190.1 × 5.11	37.1	346.9	33.9 × 3.10	10.9	348.2	0.19	37.5	2724	2589	0.950
	C4-36-0.34-1E	190.5 × 5.15	37.0	346.9	59.6 × 3.32	18.0	342.1	0.34	37.5	2718	2535	0.933
	C4-36-0.34-2E	188.2 × 5.04	37.3	346.9	59.1 × 3.28	18.0	342.1	0.34	37.5	2482	2535	1.021
	C4-36-0.56-1E	190.7 × 5.11	37.3	346.9	101.6 × 4.03	25.2	345.8	0.56	37.5	2626	2500	0.952
	C4-36-0.56-2E	189.2 × 5.0	37.2	346.9	101.2 × 4.05	25.0	345.8	0.56	37.5	2462	2500	1.015
Batch 2	C9-36-0-1E	190.2 × 5.13	37.1	464.0	0 × 0	/	0	0	37.5	3104	2956	0.952
	C9-36-0-2E	190.0 × 5.10	37.3	464.0	0 × 0	/	0	0	37.5	3111	2956	0.950
	C9-36-0.19-1E	188.9 × 5.09	37.1	464.0	33.7 × 3.09	10.9	348.2	0.19	37.5	3182	3055	0.960
	C9-36-0.19-2E	188.9 × 5.12	36.9	464.0	33.5 × 3.06	10.9	348.2	0.19	37.5	3232	3055	0.945
	C9-36-0.34-1E	191.0 × 5.15	37.1	464.0	59.4 × 3.31	17.9	342.1	0.34	37.5	3286	3100	0.943
	C9-36-0.34-2E	190.1 × 5.11	37.2	464.0	59.1 × 3.29	18.0	342.1	0.34	37.5	3242	3100	0.956
	C9-36-0.56-1E	190.7 × 5.15	37.0	464.0	101.1 × 4.10	24.7	345.8	0.56	37.5	3082	3010	0.977
	C9-36-0.56-2E	190.7 × 5.09	37.5	464.0	100.9 × 4.07	24.8	345.8	0.56	37.5	3192	3010	0.943
Batch 3	C4-24-0.34-1E	190.4 × 5.15	37.0	346.9	59.9 × 3.33	18.0	342.1	0.34	29.0	2460	2380	0.967
	C4-24-0.34-2E	190.0 × 5.11	37.2	346.9	59.1 × 3.31	17.9	342.1	0.34	29.0	2494	2380	0.954
	C4-36-0.34-1E	189.1 × 5.10	37.1	346.9	59.4 × 3.35	17.7	342.1	0.34	37.5	2623	2555	0.974
	C4-36-0.34-2E	190.1 × 5.07	37.5	346.9	59.7 × 3.35	17.8	342.1	0.34	37.5	2588	2555	0.987
	C4-48-0.34-1E	189.9 × 5.12	37.1	346.9	58.9 × 3.31	17.8	342.1	0.34	51.0	2950	2856	0.968
	C4-48-0.34-2E	188.6 × 5.08	37.1	346.9	58.9 × 3.33	17.7	342.1	0.34	51.0	3026	2856	0.944
Batch 4	C4-36-0.33-1E(4.3)	190.3 × 4.26	44.7	336.8	59.4 × 3.36	17.7	342.1	0.33	37.5	2376	2311	0.973
	C4-36-0.33-2E(4.3)	190.1 × 4.21	45.2	336.8	59.3 × 3.30	18.0	342.1	0.33	37.5	2406	2311	0.961
	C4-36-0.34-1E(5.3)	189.7 × 5.12	37.1	346.9	59.5 × 3.32	17.9	342.1	0.34	37.5	2611	2540	0.973
	C4-36-0.34-2E(5.3)	188.8 × 5.08	37.2	346.9	59.5 × 3.31	18.0	342.1	0.34	37.5	2579	2540	0.985
	C4-36-0.34-1E(6.8)	189.1 × 6.77	27.9	327.3	59.7 × 3.34	17.9	342.1	0.34	37.5	2894	2789	0.964
	C4-36-0.34-2E(6.8)	188.6 × 6.73	28.0	327.3	59.8 × 3.33	18.0	342.1	0.34	37.5	2928	2789	0.953
Mean value												0.964
Standard deviation (SD)												0.021
Coefficient of variation (CoV)												0.021

and corresponding nominal wall thicknesses (t_o) of 4.3 mm, 5.3 mm and 6.8 mm, respectively. The inner circular steel tube's nominal diameters (D_i) are 34 mm, 60 mm and 101.6 mm and corresponding nominal wall thicknesses (t_i) are 3.1 mm, 3.35 mm and 4.1 mm, respectively. To avoid overall buckling of specimens, the slenderness ratio of each specimen was considered as $L/D_o = 3$. In addition, the initial imperfections and residual stresses were generated on the steel tube sections owing to the uncontrollable factors in the manufacturing process [32]. However, due to the filling of concrete, their influences on the strength of stub columns are insignificant [33]. So, about their measurement procedures were omitted in this paper. The outer steel tubes were fabricated using two different steel (STK400 and STK490), whereas the inner steel tubes consisted of only one kind of steel (STK400). By means of the tensile tests of coupons extracted from the same steel plate prior to manufacture, the material properties of steel were obtained. On the test day, the average compressive strength values of the 100×200 mm concrete cylinders were 30.2 MPa, 39.1 MPa, and 53.1 MPa, respectively. They were converted to standard 150×300 mm concrete cylinder compressive strengths ($f_{cyl,150}$) of 29.0 MPa, 37.5 MPa, and 51.0 MPa, respectively. For simplicity, the columns are marked as: section type of steel tube + type of external steel tube + design strength of concrete + hollow ratio + number of the specimen + loading type.

A schematic of the loading device was depicted in Fig.3.1. A universal testing machine that provides a maximum compressive capacity of 5000 kN was employed for all experimental tests. Axial compressive loads through the top and bottom bearing plates were applied to both ends of all specimens. Two LVDTs were employed to measure whether the specimens were twisted in the loading plane during the test. Additionally, to measure the longitudinal and transverse strains of the external and internal steel tubes, twelve pairs of bidirectional strain gauges were attached to the symmetrical positions at the mid-height and 100 mm from both two ends of the specimens. The axial deformation and load variations of the specimens were obtained directly from the universal testing machine.

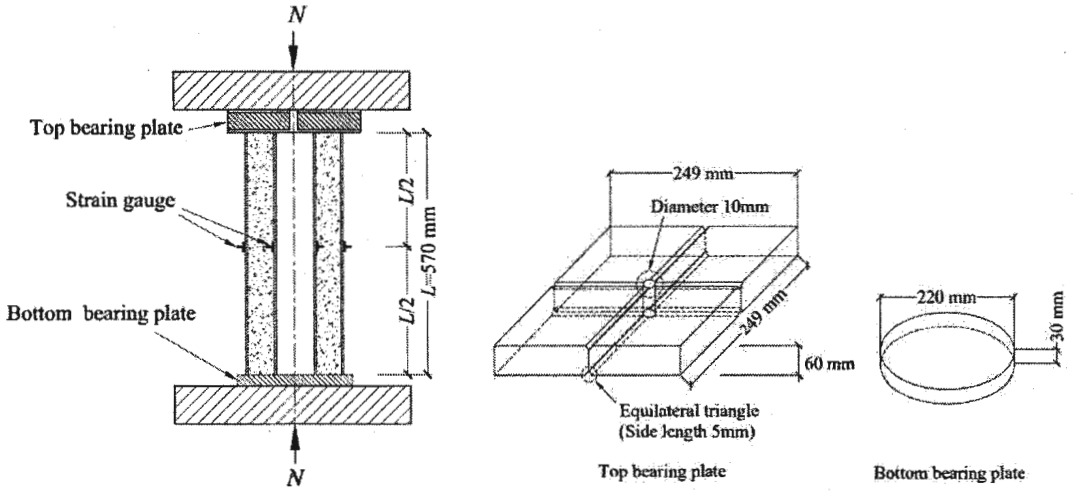

Fig.3.1 Schematic of test device

3.2.2. Experimental results and discussion

The average axial load (N) vs strain (ε) curves for each set of specimens were depicted in Figs.3.2(a) to 3.2(d), and the corresponding axial compressive strengths were shown in Table 3.1.

From Figs.3.2(a) to 3.2(d), it can be noticed that the axial load vs strain curves did not drop abruptly after the ultimate load, but instead proceed through a long ductility stage. This result indicates that the tested specimens exhibited good ductility performance. As shown in Table 3.1, the axial compressive strengths of the CFDST short circular columns with STK400 external steel tubes first increased and then decreased as the hollow ratio χ (D_i/D_o) increased. This finding implies that the hollow ratio χ considerably affected the ultimate axial strengths of CFDST short circular columns. For CFDST short circular columns with STK490 outer steel tubes, it can be found that the axial compressive strengths of columns, which the hollow ratio χ ranged from 0 to 0.34, increased with increasing χ. However, the axial compressive strengths of columns with the hollow ratio χ between 0.34 and 0.56 decreased with increasing χ. The axial compressive strengths of the circular CFDST short columns with STK400 outer steel tubes are obviously smaller than those of specimens with STK490 outer steel tubes. These observations indicate that the yield strength of the outer steel tube strongly affected the axial compressive strengths of circular CFDST short columns. In addition, with increasing the unconfined concrete strength and wall thickness of external steel tube, the axial compressive strengths of circular CFDST short columns were increased. This result suggests that increasing the concrete strength and wall thickness of outer steel tube can improve the axial compressive strengths of CFDST short circular columns.

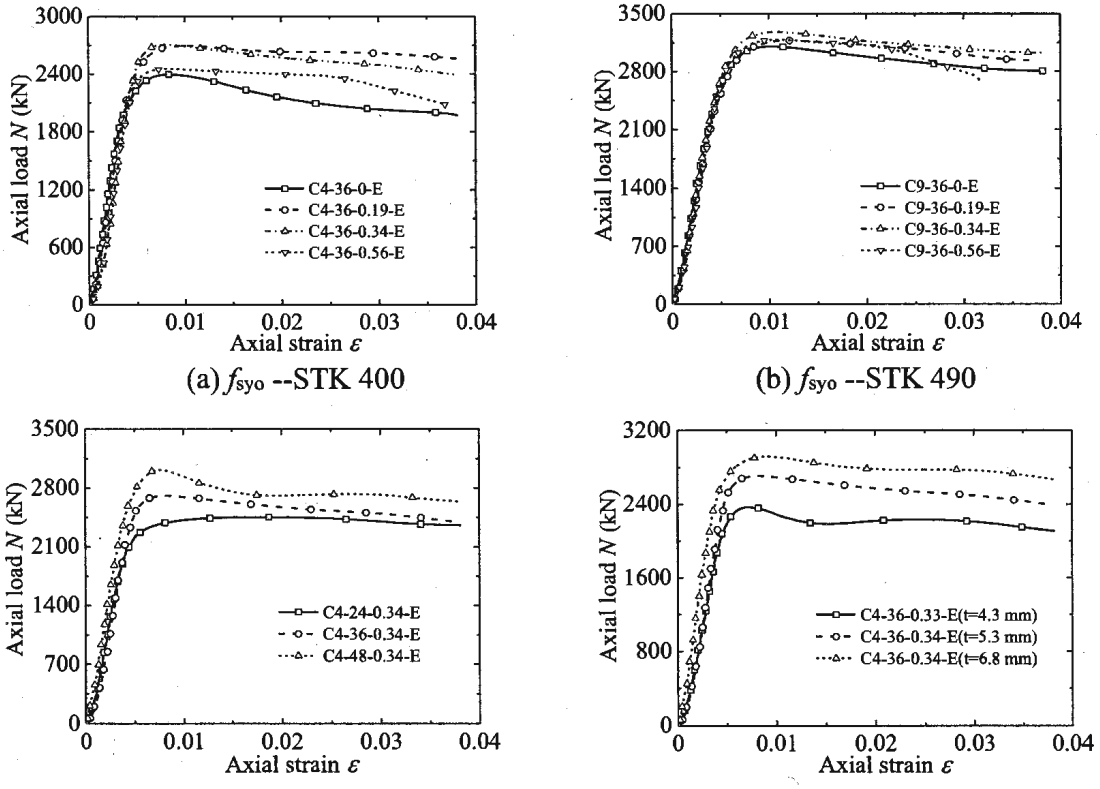

(a) f_{syo} --STK 400 (b) f_{syo} --STK 490

(c) f_c = 24, 36, 48 MPa (d) t_o = 4.3, 5.15, 6.8 mm

Fig.3.2 Axial load vs shortening curves of circular CFDST stub columns

The failure modes of the tested specimens mainly include two aspects, and here specimen C9-36-0.31-5-1 was taken as an example and its failure modes were shown in Fig. 9. Fig. 9(a) shows that the external steel tube failed in the form of outward local buckling and that the main failure locations were at the mid-height and 40 mm from both two ends of the specimens. However, Fig. 9(b) shows

that the inner steel tube failed by inward local buckling at the mid-height of the specimens. This phenomenon is consistent with previously reported results in Refs. [6,14].

3.3. Comparison of the behaviors of CFDST columns under different loading conditions

3.3.1. Comparison based on the test results

Fig.3.3 shows the comparison of the axial load vs. strain curves of the selected CFDST column specimens under different loading conditions. From this figure, it can be seen that for the specimens with the hollow ratio of 0 and 0.19, the axial load of the entire-section axially loaded specimens is larger than that of the concrete axially loaded ones. However, the opposite result is found after the axial load reaches the ultimate strength. For the specimens with the hollow ratio of 0.34 and 0.56, in the initial loading phase, the axial load of the entire-section axially loaded specimens is almost equal to that of the concrete axially loaded ones. As the axial strain increases, the axial load of the entire-section axially loaded specimens become smaller than that of the concrete axially loaded ones.

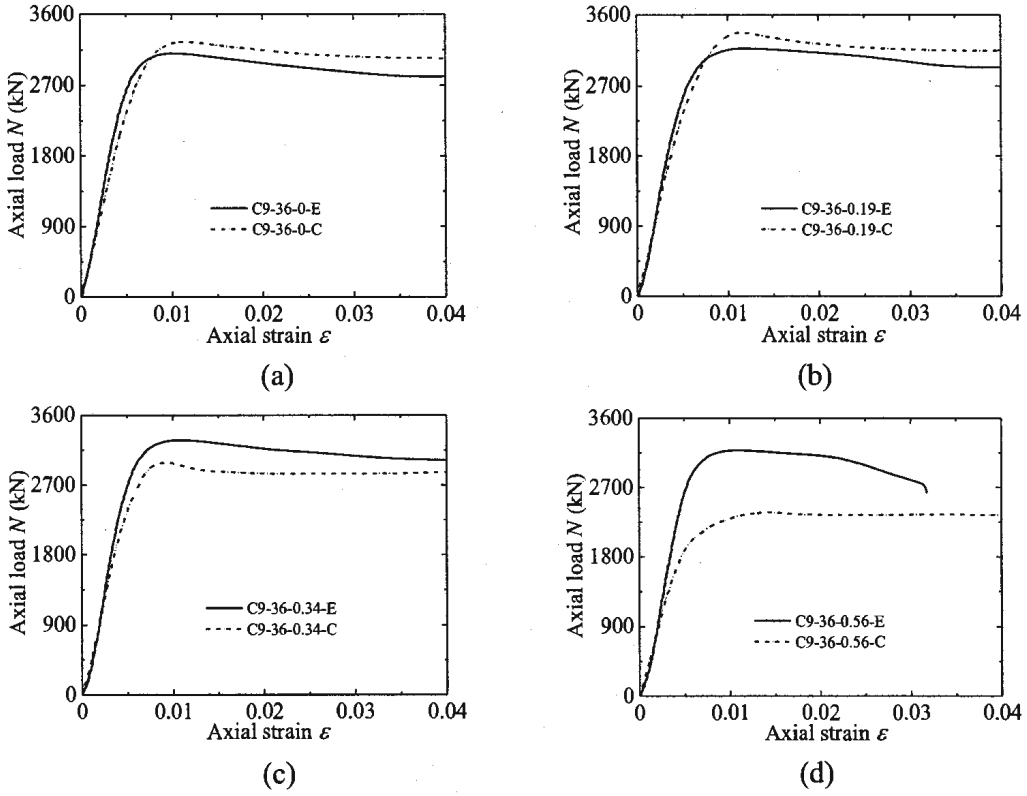

Fig.3.3 Comparison of axial load vs. strain curves of CFDST columns

Fig.3.4 shows the comparison of the ultimate strength of CFDST column specimens under different loading conditions. Fig.3.4(a) shows that the ultimate strength of the specimens first increases and then decreases. Additionally, it can be also seen that for the specimens with the hollow ratio of 0 and 0.19, the ultimate strength of the entire-section axially loaded specimens is larger than that of the concrete axially loaded ones, while the opposite result is found for the specimens with the hollow ratio of 0.34 and 0.56. This indicates that the lateral confinement effect of outer and inner steel tubes to sandwiched concrete decreases as the hollow ratio increases. Fig.3.4(b) shows that the ultimate strength of the specimens increases with the increase of the concrete strength. The ultimate strength of the entire-section axially loaded specimens with the hollow ratio of 0.34 is larger than that

of the concrete axially loaded ones. Fig.3.4(c) shows that the ultimate strength of the specimens decreases with the increase of the D_o/t_o ratio. The ultimate strength of the entire-section axially loaded specimens is smaller than that of the concrete axially loaded ones at first, and then larger than that of the concrete axially loaded ones with the increase of the D_o/t_o ratio. This is mainly due to the stronger lateral confinement effect of the specimens with smaller D_o/t_o ratio (thicker wall thickness).

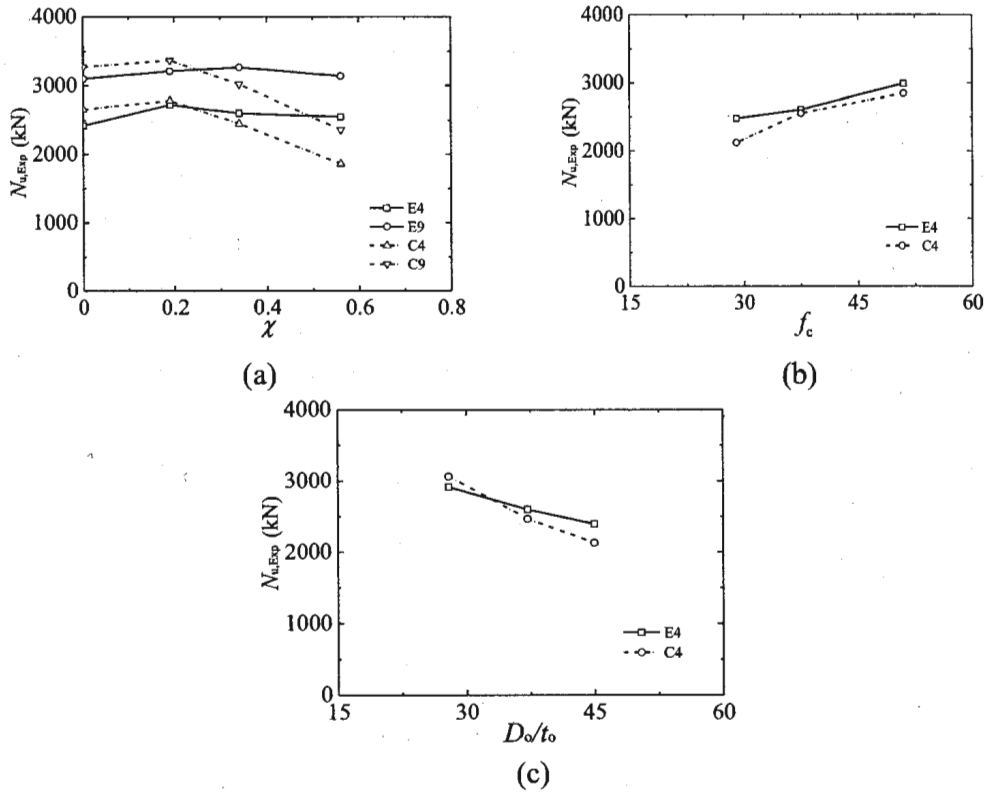

Fig.3.4 Comparison of ultimate strengths of CFDST columns

3.3.2. Comparison based on the numerical results

3.3.2.1. Establishment and verification of the FE models

In this section, FE models are established and verified by the conducted experimental results, and the verified FE models are then used to investigate the mechanical behaviors of the entire-section and the sandwiched concrete axially loaded CFDST columns. The details of the FE models can be found in Chapter 2. Note that loading types of the entire-section and the sandwiched concrete axially loaded CFDST columns are different. The FE models on the concrete axially loaded CFDST columns have been verified in Chapter 2, which will not be repeated here. Accordingly, only the FE models on the concrete axially loaded CFDST columns need to be verified. Herein, FE models are validated by comparing with the axial load-shortening curves, ultimate load and failure modes from the experimental results.

Fig.3.5 shows the comparison of the predicted to experimental axial load vs strain curves of the selected CFDST specimens. It can be seen from this figure that FE models can almost replicate axial load-deformation histories of the tested specimens. A slight discrepancy is found in the prediction of the axial load vs strain curves. This discrepancy may have been resulted from the interaction between steel and concrete simulated in ABAQUS which is not completely consistent with the actual test

conditions. Moreover, the real fc values of the concrete infill may also differ from those obtained from the cylindrical material tests due to differences in the curing methods used in both specimens. A comparison of ultimate strengths between the FE modelling and experimental tests was listed in Table 3.1. The mean value of $N_{FE}/N_{u,exp.}$ is 0.964, with a standard deviation (SD) of 0.021 and a coefficient of variation (CoV) of 0.021. This indicates that the FE models perform well in predicting the axial shortening histories and ultimate strength of the tested CFDST columns. In addition, comparisons of failure modes between FE models and experimental tests were shown in Fig.3.6. From Fig.3.6, it can be observed that good agreements were achieved between numerical and test failure modes. In general, the developed FE models can be used to predict the behaviour of the the entire-section axially loaded CFDST columns with a reasonable accuracy.

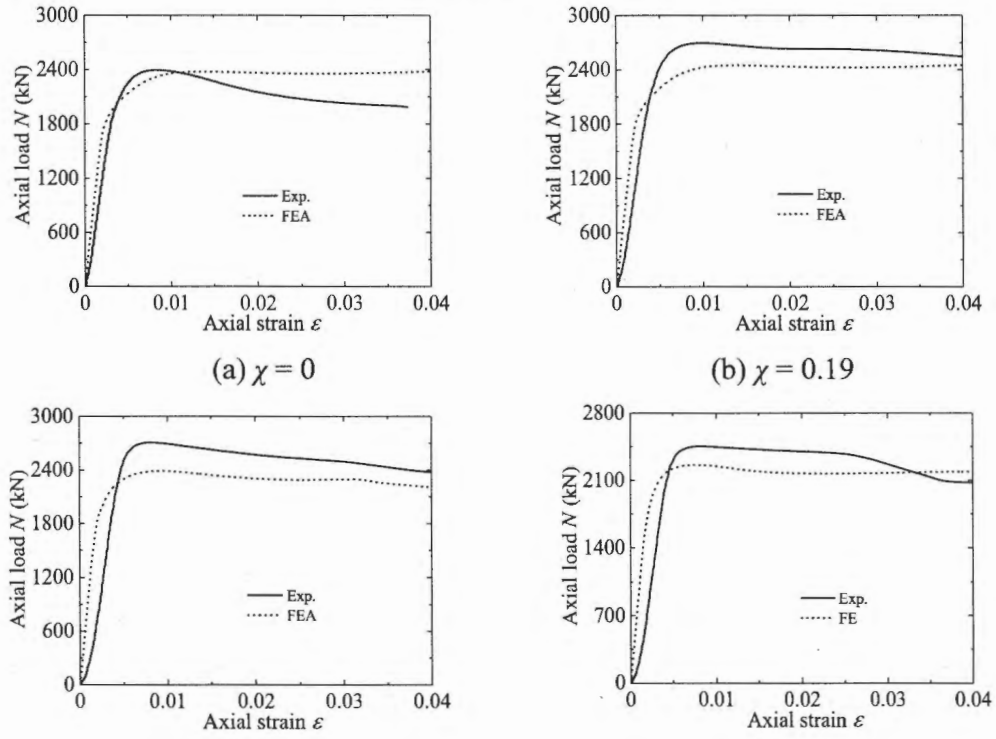

(a) $\chi = 0$ (b) $\chi = 0.19$

(c) $\chi = 0.34$ (d) $\chi = 0.56$

Fig.3.5 Comparison of the predicted to experimental axial load vs strain curves

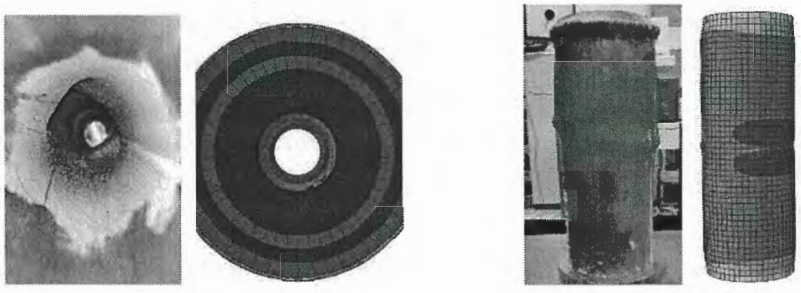

(a) Outer tube (b) Inner tube

Fig.3.6 Comparison of the predicted to experimental failure modes

3.3.2.2. Mechanical behaviours

Based on the verified FE model, the load distribution and lateral confining stress of CFDST columns under different axial loading conditions were investigated. The parameters in the columns investigated are given as: $D_o \times t_o = 300$ mm × 8 mm, $D_i \times t_i = 85.2$ mm × 4 mm, $f_{syo} = f_{syi} = 275$ MPa, $f_c = 50$ MPa, $L = 900$ mm, $\chi = 0.3$.

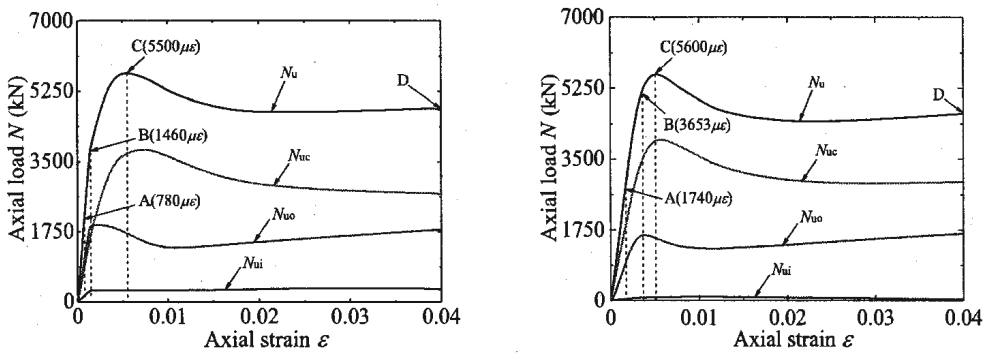

(a) Entire-section (b) Sandwiched concrete

Fig.3.7 Load distribution of different components

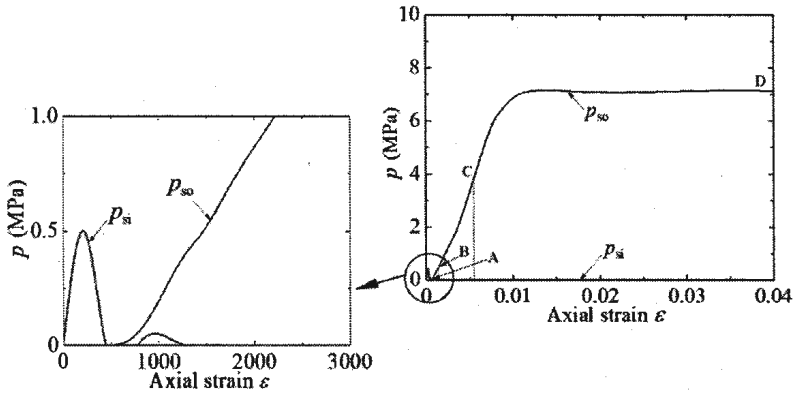

(a) Entire-section

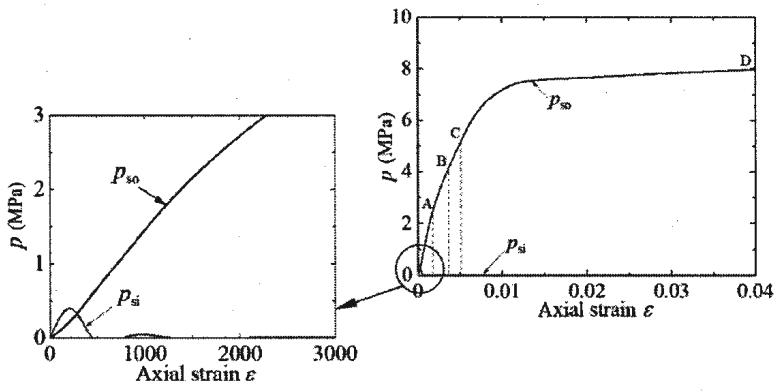

(b) Sandwiched concrete

Fig.3.8 Lateral confining stresses of outer and inner steel tubes

Fig.3.7 shows the load distribution of different components in the entire-section and sandwiched concrete axially loaded CFDST short columns. In Fig.3.7, N_u represents the ultimate axial load of the

columns; N_{uc}, N_{uo}, and N_{ui} denote the ultimate axial loads of the sandwiched concrete, outer and inner steel tubes, respectively. From this figure, it can be seen that the axial load of the columns fisrt increases and then decreases with the increase of the axial strain, and the similar phenomenon is found for sandwiched concrete. For outer steel tube, its axial load first decreases and then continues to increase in the post-peak stage, which is mainly due to the strain hardening of the steel tube. For inner steel tube in the entire-section axially loaded CFDST columns, the axial load first increases linearly and then keeps almost constant. Because of the inevitable friction referring to the tests, the inner steel tube in the concrete axially loaded CFDST columns also bears a certain axial load, which first increases and then decreases.

Fig.3.8 presents the lateral confining stresses of the outer and inner steel tubes to concrete in the entire-section and sandwiched concrete axially loaded CFDST short columns. In Fig.3.8, p_{so} and p_{si} stand for the lateral confining stresses of outer and inner steel tubes to concrete, respectively. From this figure, it can be seen that in the initial loading stage, the lateral confining stress of outer steel tube to concrete in the entire-section axially loaded CFDST columns is almost equal to zero, while the inner steel tube provides a certain lateral confining stress. This is mainly due to the Poisson's ratio of steel tube larger than that of the concrete infilled. As the axial compression continues, the effective Poisson's ratio of the concrete infilled become larger than that of steel tube. As a result, the lateral confining stress of the outer steel tube begins to appear and gradually increase, and finally approaches a constant. On the contrary, the lateral confining stress of the inner steel tube begins to decrease and finally approaches zero. Unlike the entire-section axially loaded CFDST columns, in the initial loading stage, the outer steel tube in the concrete axially loaded CFDST columns yields the lateral confining stress to concrete infilled. It is mainly due to the fact that, in the early loading phase, the effective Poisson's ratio of concrete in the tested specimens with only concrete axially loaded has already exceeded that of outer steel tube. As the axial deformation increases, the lateral confining stress of the outer steel tube gradually increases, and finally approaches a constant. The change trend in the lateral confining stress of the inner steel tube is similar to that of the entire-section axially loaded CFDST columns.

Fig.3.9 shows the longitudinal stress distribution of the sandwiched concrete in the entire-section and sandwiched concrete axially loaded CFDST short columns. Points A, B, C, and D denote the different stages in the loading process, respectively, as shown in the Fig.3.7. From this figure, it can be observed that the longitudinal stresses of the concrete in Points A, B, C, and D in concrete axially loaded CFDST columns are larger than those of concrete in the entire-section axially loaded CFDST short columns except for the edge of the concrete at point D. This is mainly due to the concrete in concrete axially loaded CFDST columns that is only loaded.

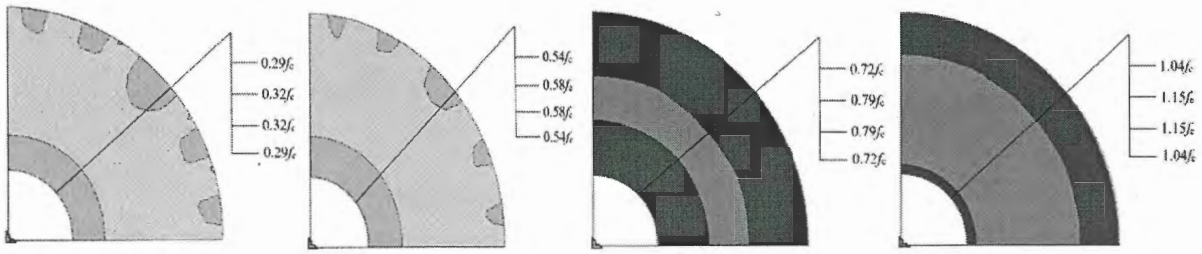

Point A Point B Point A Point B

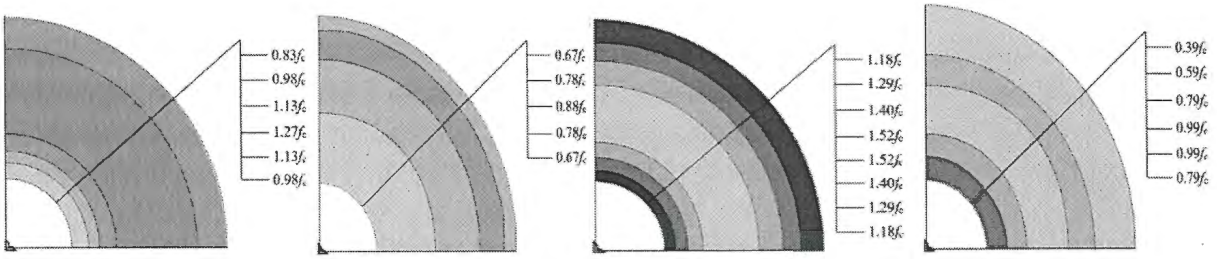

Point C Point D Point C Point D

(a) Entire-section loaded (b) Concrete loaded

Fig.3.9 Lateral confining stresses of outer and inner steel tubes

3.4. CSPs of confined concrete in the entire-section axially loaded CFDST columns

Previous investigations have shown that the CSPs of confined concrete significantly affected the compressive behavior of confined concrete in FRP-confined concrete or concrete-filled steel tube CFST columns. Unlike the concrete in FRP-confined concrete or CFST columns, which is only confined by external materials, e.g., FRP sheet or steel tube, the concrete in CFDST columns is confined by both the external and internal steel tubes. Due to different confinement mechanisms, the CSPs of confined concrete in CFDST columns may be different from those in FRP-confined concrete or CFST ones, which, however, have not been investigated so far. In the present paper, the CSPs of confined concrete in circular CFDST stub columns were experimentally investigated, and their corresponding influences on the compressive strength were also discussed. The current work is organized as: In Section 3.4.1, CSP's determination and its relevant effect are defined in detail. The details of 28 axially loaded CFDST short column specimens and the corresponding experimental tests are also described. In Section 3.4.2, the CSPs of confined concrete in circular CFDST columns and the relevant CSP effect on the compressive strength of confined concrete are investigated. In Section 3.4.3, a CSP-based compressive strength model for estimating the ultimate strength of CFDST columns is proposed.

3.4.1. Experimental tests to investigate the confining stress paths (CSPs)

3.4.1.1. Determination of CSPs

The determination of CSPs is the basis of describing the CSPs. As defined in the previous studies presented by the authors [29-30], the CSP of confined concrete is commonly specified as the relationship between the lateral confining stress (σ_r) and the ratio of axial concrete compressive stress divided by unconfined concrete strength (f_{cz}/f_c). A typical stress state diagram for circular CFDST columns is given in Fig. 3.10. It should be noted that, unlike the concrete in a circular FRP-confined concrete or CFST columns, which is only confined by external FRP-sheet or steel tube, the concrete in a circular CFDST column are confined by both the external and internal steel tubes. Therefore, in a CFDST column, two different CSPs may be yielded based on the confinement mechanisms of the external and internal tubes. The lateral confining stresses σ_{or} and σ_{ir} induced by the external and internal tubes and the corresponding axial concrete compressive stress f_{cz} can be determined by Eqs. (3.1) to (3.3)

$$\sigma_{or} = \frac{-2\sigma_{o\theta}t_o}{D_o - 2t_o} \tag{3.1}$$

$$\sigma_{ir} = \frac{2\sigma_{i\theta} t_i}{D_i} \tag{3.2}$$

$$f_{cz} = \frac{N - \sigma_{oz} A_{os} - \sigma_{iz} A_{is}}{A_{sc}} \tag{3.3}$$

where N represents the measured axial load of the column; D_o and D_i symbolize respectively the outer diameters of the external and internal tubes with the wall thickness of t_o and t_i; A_{os} and A_{is} represent respectively the cross-sectional areas of the external and internal tubes; A_{sc} stands for the cross-sectional area of the sandwiched concrete; σ_{oz} and $\sigma_{o\theta}$ denote the axial and circumferential stresses of the external tube, respectively; σ_{iz} and $\sigma_{i\theta}$ symbolize respectively the axial and circumferential stresses of the internal tube. Through the following procedures, the axial and circumferential stresses could be computed by using the readings from the measured strains pasted on the surfaces of steel tubes.

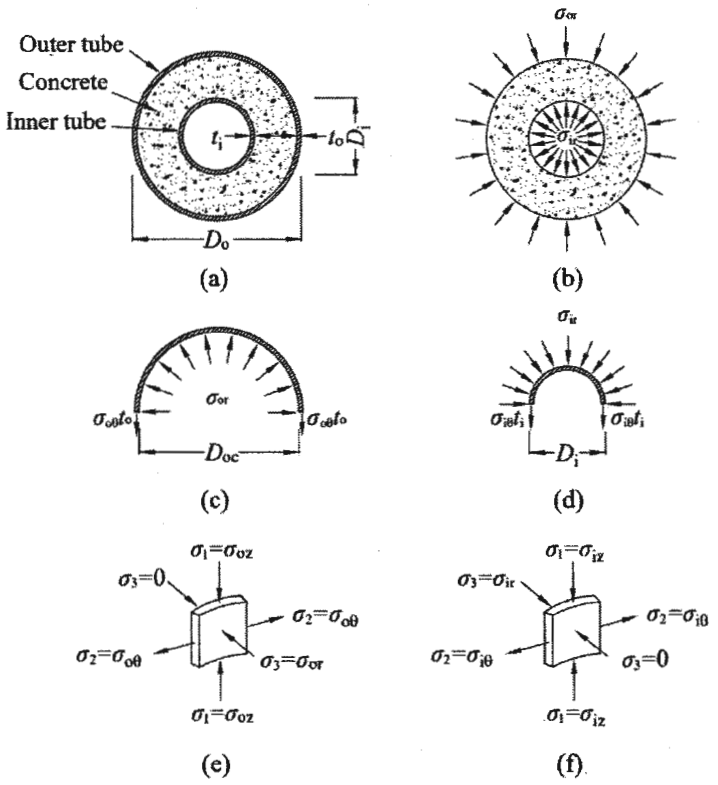

Fig.3.10 Stress state between steel tubes and concrete

The von Mises stress (or the equivalent stress) σ_e is introduced to identity the stress state of the steel tube:

$$\sigma_e = \sqrt{\sigma_z^2 - \sigma_z \sigma_\theta + \sigma_\theta^2} \tag{3.4}$$

In the elastic phase ($\sigma_e < f_y$), the stress components of the steel tube can be computed by the generalized Hooke's Law:

$$\begin{Bmatrix} d\sigma_z \\ d\sigma_\theta \end{Bmatrix} = \frac{E_s}{1-\upsilon_s^2}\begin{bmatrix} 1 & \upsilon_s \\ \upsilon_s & 1 \end{bmatrix}\begin{Bmatrix} d\varepsilon_z \\ d\varepsilon_\theta \end{Bmatrix} \tag{3.5}$$

where $d\varepsilon_z$ and $d\varepsilon_\theta$ denote respectively the axial and circumferential strain increments of steel tube; υ_s and E_s represent respectively the Poisson's ratio and tangent moduli of steel tube, and they can be determined by:

$$\upsilon_s = \begin{cases} 0.283 & \sigma_e < f_p \\ 0.217\dfrac{\sigma_e - f_p}{f_y - f_p} + 0.283 & f_p \le \sigma_e \le f_y \\ 0.5 & \sigma_e > f_y \end{cases} \tag{3.6}$$

$$E_s = \begin{cases} E & \sigma_e < f_p \\ \dfrac{(f_y - \sigma_e)\sigma_e}{(f_y - f_p)f_p}E & f_p \le \sigma_e \le f_y \end{cases} \tag{3.7}$$

where E denotes the elastic moduli, f_y symbolizes the steel yield stress, and f_p represents the proportional limit, herein, assumed to be $0.75f_y$.

In the plastic phase ($\sigma_e \ge f_y$), the stress of the steel tube can be computed by the incremental Prandtl-Reuss equations:

$$\begin{Bmatrix} d\sigma_z \\ d\sigma_\theta \end{Bmatrix} = \frac{E_s}{Q}\begin{bmatrix} S_\theta^2+2q & -S_zS_\theta+2\upsilon_s q \\ -S_zS_\theta+2\upsilon_s q & S_z^2+2q \end{bmatrix}\begin{Bmatrix} d\varepsilon_z \\ d\varepsilon_\theta \end{Bmatrix} \tag{3.8}$$

$$Q = S_\theta^2 + S_z^2 + 2\upsilon_s S_\theta S_z + 2H(1-\upsilon_s)\sigma_e^2/(9G) \tag{3.9}$$

$$q = \frac{2H}{9E_s}\sigma_e^2 \tag{3.10}$$

in which H denotes the gradient of equivalent plastic stress–strain curve obtained from the tensile coupon tests of the steel tube; G symbolizes the shear moduli, computed by $G = E_s/(2(1+\upsilon_s))$; S_z and S_θ represent respectively the deviatoric stresses in axial and circumferential directions, and are computed by:

$$S_z = (2\sigma_z - \sigma_\theta)/3 \tag{3.11}$$

$$S_\theta = (2\sigma_\theta - \sigma_z)/3 \tag{3.12}$$

Accordingly, using Eqs. (3.4) to (3.12), the axial and circumferential stresses can be derived from the read axial/circumferential strain at each loading process. The axial stress σ_z and circumferential stress σ_θ of the steel tube at each loading process are substituted into Eqs. (3.1) to (3.3), the lateral confining stresses induced by the external and internal tubes as well as the axial compressive stress of the sandwiched concrete will be obtained. In the current paper, the compressive stress is assumed to be positive, naturally, the tensile stress is negative. Note that the stress of steel tube computed by

Eqs. (3.4) to (3.12) is average stress along the circumferential of the steel tube. Additionally, the CSP is an average of the two identical specimens that are employed in each subset.

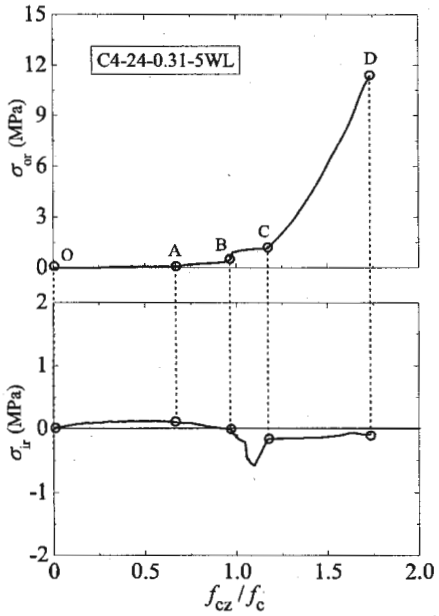

Fig.3.11 CSPs of confined concrete in a CFDST column

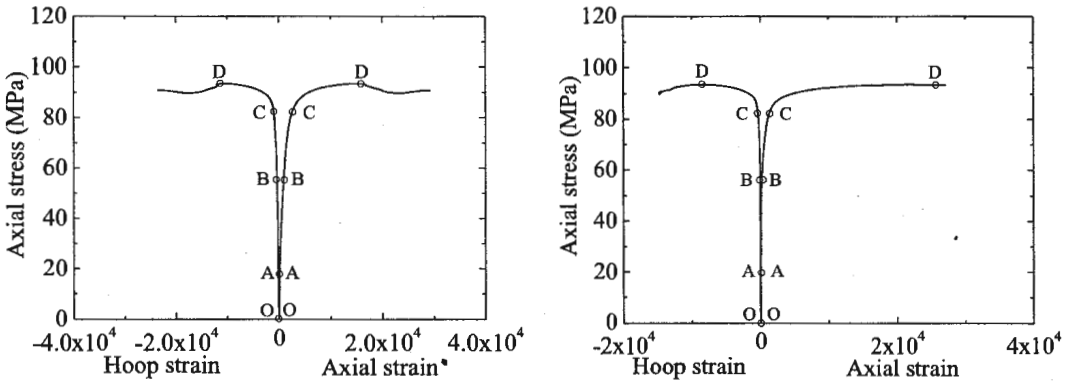

(a) Outer tube skin (b) Inner tube skin

Fig.3.12 Axial stress-strain curves for specimen C4-24-0.31-5WL

A typical the CSP graph of confined concrete in a circular CFDST column is presented in Fig.3.11, in which the specimen C4-24-0.31-5WL is taken as an example. The corresponding axial stress versus axial or circumferential strain curves of the external and internal tubes are described in Fig. 3.12. From Fig.3.11, one can clearly see that two different CSPs appear in CFDST columns owing to different confinement mechanisms of the external and internal tubes. Thereinto, the σ_{or} vs. f_{cz}/f_c curve represents the CSP induced by external tube, referred to as the 'external CSP', while the σ_{ir} vs. f_{cz}/f_c curve stands for the CSP yielded by internal tube, called the 'internal CSP'.

First of all, for the external CSP, its changing characteristics are similar to the CSP of confined concrete in a CFST column previously reported by the authors [29]. Generally, the external CSP consists of four stages. For stage OA, due to the Poisson's ratio of the steel tube larger than that of the concrete, the sandwiched concrete experiences no or less the lateral confining stress (σ_{or}). When

the f_{cz}/f_c exceeds point A (about 0.65), the microcracks in the sandwiched concrete propagate rapidly, which results in its lateral expansion larger than that of the steel tube. As a result, the lateral confining stress afforded to the sandwiched concrete raise smoothly. Then, an abrupt lateral expansion of the concrete owing to its fracture at point B triggers a sharp rise in the lateral confining stress. Further, the steel tube yields at point C with the increase of the f_{cz}/f_c. After undergoing a short plateau, owing to the strain hardening of steel tube, the lateral confining stress keeps on raising and ends at the point D of the ultimate state. Generally, the stages OB and BD in external CSP suggest that the concrete in a CFDST column experiences the pre- and post-fracture stages, which are similar to the state of concrete in a CFST column [29].

Secondly, different from the external CSP, the internal CSP exhibits insignificant change and mainly fluctuates around horizontal zero axis. Corresponding to the external CSP, the internal CSP also consists of four stages. For stage OA, owing to the Poisson's ratio of the steel tube larger than that of the concrete, the slight interaction between the internal tube and the concrete is yielded. As a result, the internal tube provides a slight lateral confining stress (σ_{ir}) to the inner surface of the sandwiched concrete. When the f_{cz}/f_c exceeds point A, the microcracks in the sandwiched concrete propagate rapidly. Because of different crack growth speed on the inner and outer surfaces of the sandwiched concrete, the lateral expansion from its the outside to the inside gradually becomes larger than that of the internal tube. As a result, the lateral confining stress induced by the internal tube decreases smoothly. Also for the internal tube, the compressive stress is taken as a positive as defined above, naturally, the tensile stress is negative. For OAB phase, the CSP is above the horizontal axis due to the extrusion of steel tube and concrete. As the f_{cz}/f_c continues to increase, the Poisson's ratio of the inner surface of the sandwiched concrete begins to be greater than that of internal tube, causing the separation tendency of the contact surface between the internal tube and concrete. However, with the slow progress of the separation, the mutual tensile action is generated due to the adhesion between the concrete and internal tube, and it ends at point D of the ultimate state. As a result, the CSP in the stage BCD is below the horizontal zero axis.

3.4.1.2. Evaluation index of CSPs

Three typical CSPs of concrete under different restricted conditions, i.e., the paths P_0(OB), P_i(OCG) and P_a(OAH), are illustrated in Fig.3.13. Among them, the path P_0(OB) is the CSP of the plain concrete, and the path P_a(OAH) stands for the CSP of the actively confined concrete. However, the path P_i(OCG) represents the CSP of the passively confined concrete. Such CSP is usually generated in the passively confining concrete structures, e.g., CF(D)ST columns, FRP-confined concrete and steel-reinforced concrete (RC) columns. Compared with the typical CSP of the confined concrete in FRP-confined concrete given by Lin et al. [33], the obvious difference of the studied path in this paper is only BC stage due to the yield of the steel tube, while other stages are similar. The detailed elucidation for the three typical CSPs can be found in Ref. [30].

In the current paper, two assessment indices developed by the authors [29-30] were employed to quantify the performance of the CSPs and the relationship between the CSP and the concrete compressive strength.

First of all, the domination extent of the lateral confining stress in a CSP (P_i) is represented by a dominance index determined by:

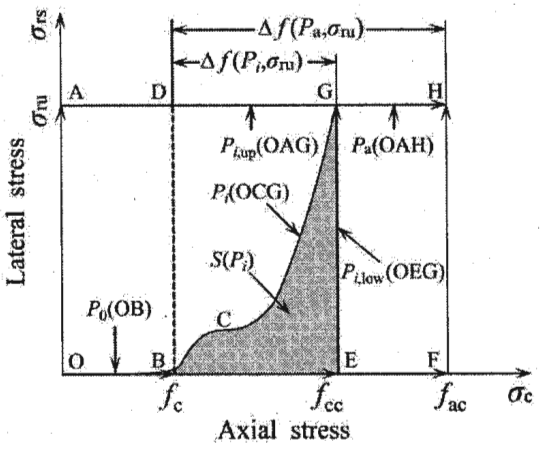

Fig.3.13 Typical CSPs of concrete under different confining conditions

$$SI(P_i)=\frac{S(P_i)}{S(P_{i,up})} \tag{3.13}$$

in which $S(P_i)$ symbolizes the area enclosed by the paths P_i and $P_{i,low}$(OEG). $S(P_{i,up})$ denotes the area enclosed by the paths $P_{i,up}$ (OAG) and $P_{i,low}$ (OEG). Noticeably, a larger value of SI means that the path P_i is closer to path P_a, which indicates that a more remarkable lateral confining stress is achieved. In other words, for CSP with a larger SI value, the lateral confining pressure stress acts a leading part in the confined concrete.

It should be noted that a CSP P_i in a CFST column is only generated by the external steel tube, while two different CSPs in a CFDST column are induced by the external and internal tubes, respectively. Accordingly, in this paper, an equivalent lateral confining stress was suggested to represent the overall confinement effect of the external and internal tubes to confined concrete in a CFDST column. For instance, the lateral confining stress (σ_{rs}) in Fig. 3.13 is an equivalent stress, which is defined as the vector sum of the stresses σ_{or} and σ_{ir} induced by the external and internal tubes, respectively. According to Fig.3.10, the expression of the equivalent stress σ_{rs} is determined by:

$$\sigma_{rs}=\sigma_{or}-\sigma_{ir}=\frac{-2\sigma_{o\theta}t_o}{D_o-2t_o}-\frac{2\sigma_{i\theta}t_i}{D_i} \tag{3.14}$$

Secondly, to assess the CSP effect on the compressive strength of confined concrete in a CFDST column, an effect index λ was introduced as:

$$\lambda(P_i)=\frac{\Delta f(P_i,\sigma_{ru})}{\Delta f(P_a,\sigma_{ru})} \tag{3.15}$$

in which, $\Delta f(P_i,\sigma_{ru})$ is the increment of the concrete strength under path P_i; that is to say, $\Delta f(P_i,\sigma_{ru})=f_{cc}-f_c$, where f_{cc} is the compressive strength of confined concrete; $\Delta f(P_a,\sigma_{ru})=f_{ac}-f_c$, stands for the increment of the concrete strength under path P_a, and was taken as $2.2f_c^{0.3}\sigma_{ru}^{0.81}$ proposed by authors in Ref.[29]. Noted that the CSP under path P_a is only affected by the ultimate lateral stress, i.e., $\Delta f(P_a,\sigma_{ru})=\Delta f(\sigma_{ru})$ [33]. Accordingly, the Eq.(3.15) can be written as:

$$\lambda(P_i)=\frac{\Delta f(P_i,\sigma_{ru})}{\Delta f(\sigma_{ru})} \tag{3.16}$$

In Eq. (3.16), $\lambda \neq 1.0$ means the increments of the concrete strength under different CSPs are different, which suggests that the compressive strength of confined concrete is CSP-dependent. The larger the deviation between the λ value and unity, the more remarkable the CSP effect. Instead, $\lambda=1.0$, i.e., $\Delta f(P_i,\sigma_{ru})=\Delta f(\sigma_{ru})$, means that the increments of the concrete strength under different CSPs are same, which demonstrates that the CSP makes little contribution to the change of concrete strength (i.e., so called CSP-independent).

3.4.1.3. Experimental program

In this section, in order to investigate the CSPs and the relevant CSP effects on the compressive strength of confined concrete in the studied CFDST columns, an experimental program that consists of 28 specimens was performed. 24 CFDST specimens were compiled from the previous paper published by the authors [6], and 4 additional CFST specimens (a special case; the hollow ratio of CFDST column is equal to zero) were added and taken as compared counterparts. The details of all specimens that were divided into 4 groups, i.e., G1, G2, G3 and G4, are listed Table 3.2. G1 and G2 were employed to check the effects of hollow ratio (χ) and outer tube yield stress (f_{syo}), whereas G3 and G4 were utilised to check the effects of concrete strength (f_c) and outer tube diameter-to-wall thickness ratio (D_o/t_o), respectively. For definition of 'label', take C4-36-0.18-5WL-1 as an example; 'C4' indicates that the column is made by the circular hollow tube with steel type STK400 (C9; steel type STK490) [6]; '36' represents the nominal concrete cylinder strength (150 × 300 mm), 36MPa; '0.18' symbolizes the column with a hollow ratio of 0.18, calculated by D_i/D_o; '5WL' indicates that the nominal outer tube wall thickness is 5 mm and the whole section of the column (both concrete and steel tubes) suffers the axial loading; '1' stands for the first test objective of the identical specimens in each subset. All specimens are 570 mm in height. A schematic of the test device is presented in Fig.3.14, and the detailed description can be found in Ref. [6]. It should be noted that the strain gauges attached to the section 2 will be used to obtain the CSP.

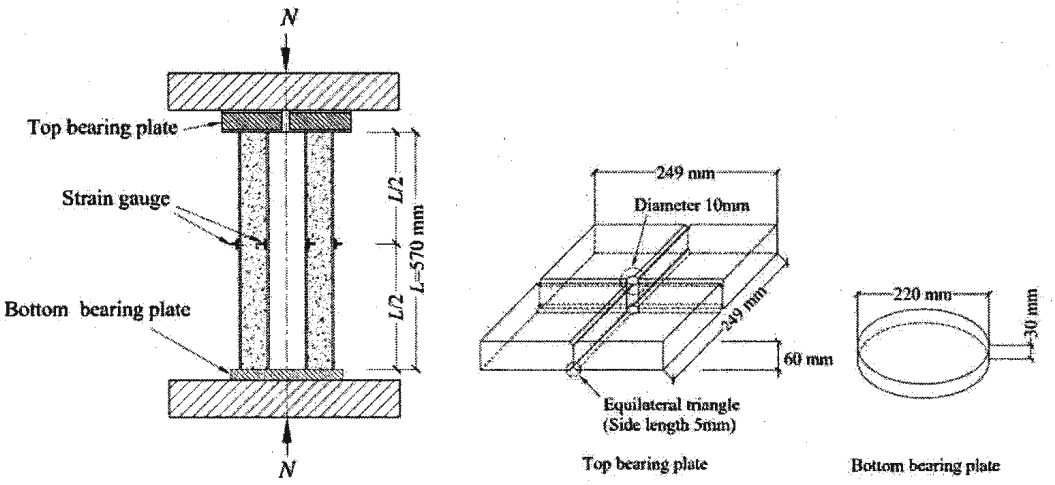

Fig.3.14 Schematic of test device

Table 3.2. Details of 28 circular CFDST short column specimens

Groups	Specimens	External steel tube				Internal steel tube				f_c (MPa)	$N_{u,exp}$	CI	η	SI	λ
		D_o (mm)	t_o (mm)	D_o/t_o	f_{syo} (MPa)	D_i (mm)	t_i (mm)	D_i/t_i	f_{syi} (MPa)						
G1	C4-36-0-5WL-1	189.2	5.11	37.0	346.9	0.0	0.00	0.0	0.0	37.5	2374	1.21	0.53	0.18	0.57
	C4-36-0-5WL-2	187.7	5.09	36.9	346.9	0.0	0.00	0.0	0.0	37.5	2390	1.23	0.53	0.17	0.60
	C4-36-0.18-5WL-1	190.6	5.15	37.0	346.9	34.0	3.08	11.0	348.2	37.5	2718	1.31	0.51	0.17	0.51
	C4-36-0.18-5WL-2	190.5	5.13	37.1	346.9	33.9	3.10	10.9	348.2	37.5	2724	1.32	0.51	0.16	0.43
	C4-36-0.31-5WL-1	190.5	5.15	37.0	346.9	59.6	3.32	18.0	342.1	37.5	2718	1.30	0.48	0.13	0.33
	C4-36-0.31-5WL-2	188.2	5.04	37.3	346.9	59.1	3.28	18.0	342.1	37.5	2482	1.22	0.47	0.14	0.35
	C4-36-0.53-5WL-1	190.7	5.11	37.3	346.9	101.6	4.03	25.2	345.8	37.5	2626	1.24	0.38	0.09	0.25
	C4-36-0.53-5WL-2	189.2	5.08	37.2	346.9	101.2	4.05	25.0	345.8	37.5	2462	1.18	0.37	0.09	0.26
G2	C9-36-0-5WL-1	189.6	5.09	37.2	464.0	0.0	0.00	0.0	0.0	37.5	3168	1.37	0.70	0.23	0.65
	C9-36-0-5WL-2	190.1	5.07	37.5	464.0	0.0	0.00	0.0	0.0	37.5	3138	1.35	0.70	0.22	0.60
	C9-36-0.18-5WL-1	188.9	5.09	37.1	464.0	33.7	3.09	10.9	348.2	37.5	3182	1.34	0.68	0.21	0.47
	C9-36-0.18-5WL-2	188.9	5.12	36.9	464.0	33.5	3.06	10.9	348.2	37.5	3232	1.36	0.69	0.2	0.45
	C9-36-0.31-5WL-1	191.0	5.15	37.1	464.0	59.4	3.31	17.9	342.1	37.5	3286	1.34	0.64	0.18	0.36
	C9-36-0.31-5WL-2	190.1	5.11	37.2	464.0	59.1	3.29	18.0	342.1	37.5	3242	1.34	0.64	0.16	0.34
	C9-36-0.53-5WL-1	190.7	5.15	37.0	464.0	101.1	4.10	24.7	345.8	37.5	3082	1.24	0.51	0.12	0.28
	C9-36-0.53-5WL-2	190.7	5.09	37.5	464.0	100.9	4.07	24.8	345.8	37.5	3192	1.29	0.50	0.09	0.27
G3	C4-24-0.31-5WL-1	190.4	5.15	37.0	346.9	59.9	3.33	18.0	342.1	29.0	2460	1.30	0.62	0.23	0.52
	C4-24-0.31-5WL-2	190.0	5.11	37.2	346.9	59.1	3.31	17.9	342.1	29.0	2494	1.32	0.61	0.19	0.51
	C4-36-0.31-5WL-1	189.1	5.10	37.1	346.9	59.4	3.35	17.7	342.1	37.5	2623	1.27	0.48	0.17	0.41
	C4-36-0.31-5WL-2	190.1	5.07	37.5	346.9	59.7	3.35	17.8	342.1	37.5	2588	1.25	0.47	0.13	0.43
	C4-48-0.31-5WL-1	189.9	5.12	37.1	346.9	58.9	3.31	17.8	342.1	51.0	2950	1.24	0.35	0.09	0.33
	C4-48-0.31-5WL-2	188.6	5.08	37.1	346.9	58.9	3.33	17.7	342.1	51.0	3026	1.29	0.35	0.08	0.35
G4	C4-36-0.31-4WL-1	190.3	4.26	44.7	336.8	59.4	3.36	17.7	342.1	37.5	2376	1.24	0.38	0.13	0.45
	C4-36-0.31-4WL-2	190.1	4.21	45.2	336.8	59.3	3.30	18.0	342.1	37.5	2406	1.27	0.38	0.14	0.52
	C4-36-0.31-5WL-1	189.7	5.12	37.1	346.9	59.5	3.32	17.9	342.1	37.5	2611	1.26	0.48	0.17	0.47
	C4-36-0.31-5WL-2	188.8	5.08	37.2	346.9	59.5	3.31	18.0	342.1	37.5	2579	1.26	0.47	0.15	0.56
	C4-36-0.31-6WL-1	189.1	6.77	27.9	327.3	59.7	3.34	17.9	342.1	37.5	2894	1.27	0.61	0.16	0.64
	C4-36-0.31-6WL-2	188.6	6.73	28.0	327.3	59.8	3.33	18.0	342.1	37.5	2928	1.30	0.60	0.19	0.63

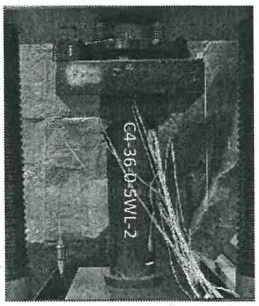

(1) C4-36-0-5WL-2

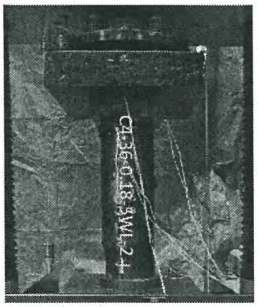

(2) C4-36-0.18-5WL-2

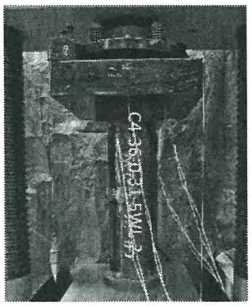

(3) C4-36-0.31-5WL-2

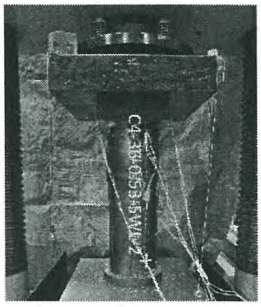

(4) C4-36-0.53-5WL-2

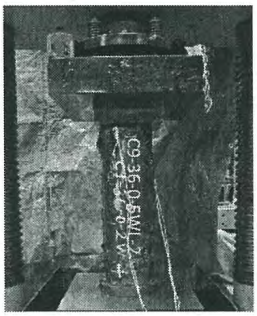

(5) C9-36-0-5WL-2

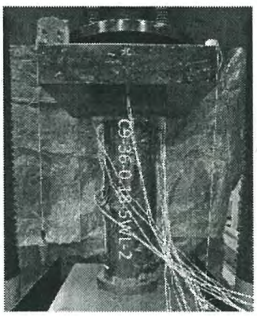

(6) C9-36-0.18-5WL-2

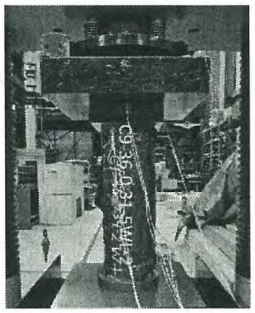

(7) C9-36-0.31-5WL-2

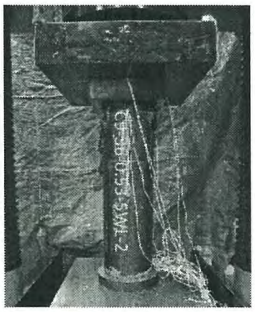

(8) C9-36-0.53-5WL-2

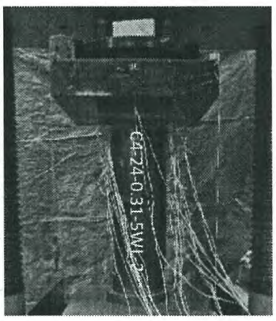

(9) C4-24-0.31-5WL-2

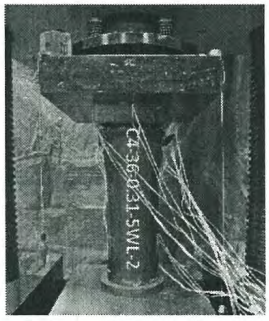

(10) C4-36-0.31-5WL-2

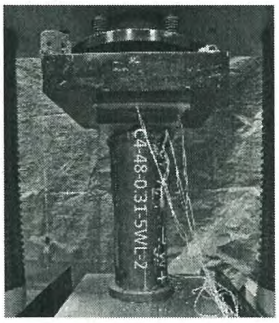

(11) C4-48-0.31-5WL-2

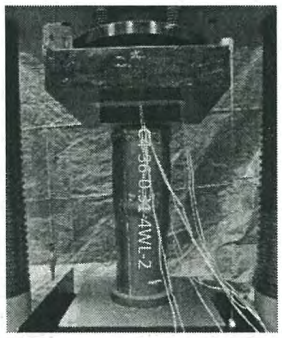

(12) C4-36-0.31-4WL-2

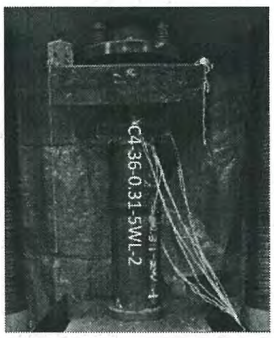

(13) C4-36-0.31-5WL-2

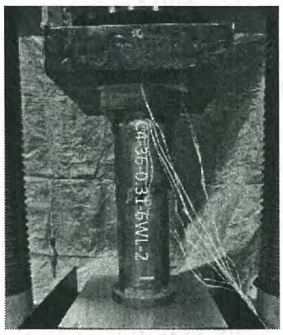

(14) C4-36-0.31-6WL-2

Fig.3.15 Failure modes of circular CFDST specimens

3.4.1.4. Experimental program

After testing, the final deformed shapes of all specimens (take one of the two identical specimens as example) are shown in Fig.3.15. In Fig.3.15, as the original chalk marks fell off, the yellow marks were added to the pictures again. From this figure, it can be observed that the outward local buckling

occurred at the mid-height and two ends of the external tubes. As the authors reported in Ref.[6], the inward local buckling generally occurred at the mid-height of the internal tubes, not tired in words here. In order to investigate the structural behaviour of the studied CFDST specimens, their axial load versus shortening curves will be discussed. Note that the axial loads of all specimens have been normalized with regard to the whole cross-sectional area since the cross-sectional areas of the specimens are not identical. The axial stress versus axial/circumferential strain curves of the external tubes for G1 and G2 specimens are shown in Fig.3.16(a), but those for G3 and G4 specimens are presented in Figs.3.16(b) and 3.16(c), respectively. For brevity's sake, Fig. 3.16 presents only one curve in two identical specimens.

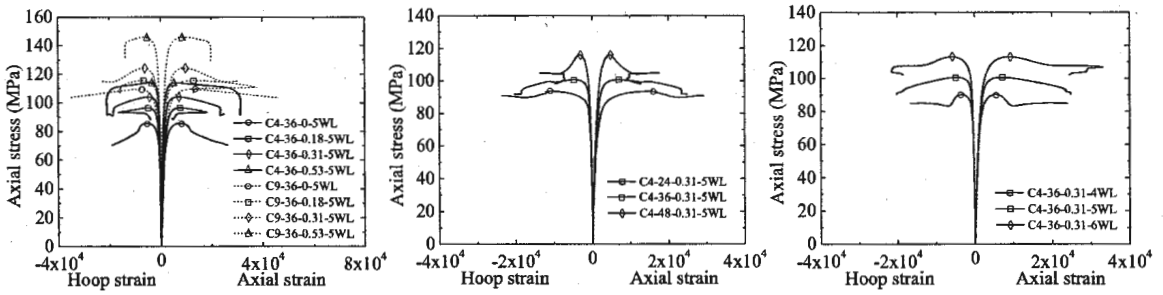

(a) G1 and G2 (b) G3 (c) G4

Fig.3.16 Axial stress vs. strain curves of outer steel tubes

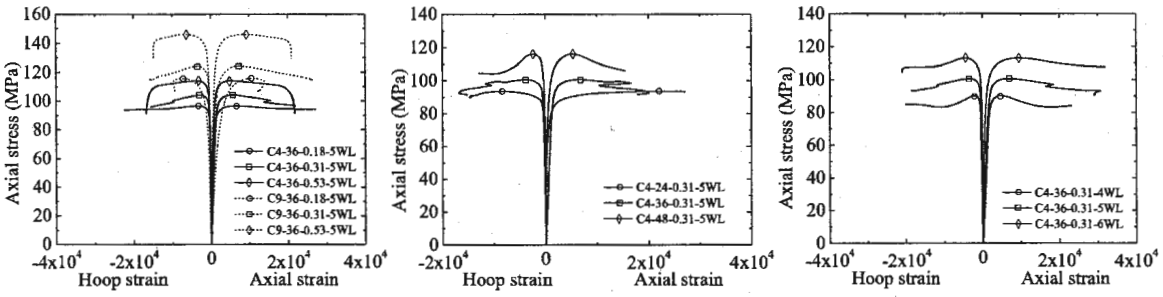

(a) G1 and G2 (b) G3 (c) G4

Fig.3.17 Axial stress vs. strain curves of inner steel tubes

Moreover, Fig.3.16 (a) shows that with increasing of the hollow ratio, the normalized ultimate axial stresses of the column are improved due to the reduction of the cross-sectional area. The absolute axial/circumferential strain of the columns at the normalized ultimate axial stresses become smaller as the hollow ratio increases but their ductility have been increased. The reason for this is that the increase of hollow ratio reduces the area of concrete and increases the steel ratio. Furthermore, for the identical hollow ratio, the normalized ultimate axial stress and the corresponding strain as well as the ductility of the columns with STK490 external tubes are larger than those of ones with STK400 external tubes. This indicates that the external tube yield stress yields a significant effect on the behaviour of the column. Fig.3.16(b) shows that as the concrete strength increases, the normalized ultimate axial stress increases, while the corresponding axial/circumferential strain decreases. This indicates that increasing the concrete strength increases the ultimate axial loads of the columns but reduces their ductility. Fig.3.16(c) shows that with the decrease of the D_o/t_o ratio (by varying the value of t_o), the normalized ultimate axial stress and the corresponding axial/circumferential strain increase

simultaneously. This is mainly attributed to the increase of steel ratio in case of the same cross-sectional area of the column. Additionally, the axial stress vs. axial/circumferential strain of the internal tubes for G1, G2, G3 and G4 specimens are illustrated in Fig.3.17. The same conclusions as the external tubes are made for the internal tubes.

To evaluate the composite effects of the steel tubes and concrete in the studied CFDST specimens, a capacity index (*CI*) is defined here and expressed by:

$$CI = \frac{N_{u,exp}}{N_{u,sum}} \tag{3.17}$$

in which $N_{u,exp}$ denotes the measured ultimate axial load of the CFDST column, as shown in Table 3.2; $N_{u,sum}$ stands for the summation of the individual strengths of the external and internal tubes as well as the sandwiched concrete, i.e., $N_{u,sum} = f_{syo}A_{os} + f_cA_{sc} + f_{syi}A_{is}$.

The capacity indices (*CIs*) of all the specimens calculated by Eq. (3.17) are listed in Table 3.2 and depicted in Fig.3.18. From this figure, it can be found that the *CI* decreases as χ, f_c and D_o/t_o ratio increase, while it increases as f_{syo} enhances. That is, the composite effects of the steel tubes and concrete infill are weakened as χ, f_c and D_o/t_o ratio increase, but they are improved as f_{syo} enhances.

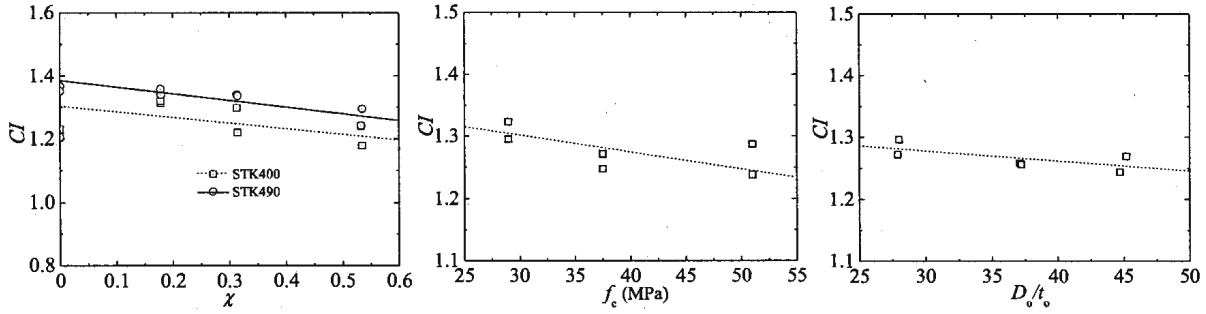

(a) Hollow ratio and steel strength (b) Concrete strength (c) D_o/t_o ratio

Fig.3.18 Composite effects of the tested specimens

3.4.2. Investigation of confining stress paths (CSPs)

3.4.2.1. General

As the authors reported in previous studies [29-30], the CSPs of confined concrete in FRP-confined concrete or CFST columns were influenced by column parameters. Similar to FRP-confined concrete or CFST columns, the CSPs of confined concrete in CFDST columns vary with varying the column variables. In this section, the CSPs of the CFDST columns with different column variables and their effects are investigated.

3.4.2.2. Parametric analysis on CSP

(1) Effects of χ on CSP

The external and internal CSPs of confined concrete in circular CFDST columns with different χ values are shown in Fig.3.19. From this figure, it can be found that the parts of the external CSPs in the pre-fracture (OAB) stages are almost similar, after which the obvious differences in the parts of the external CSPs are found in the post-fracture (BCD) stages. That is, the hollow ratio considerably affects the part of the CSP in the post-fracture (BCD) stage of the concrete infill. The CSPs in specimens with smaller χ tend to generate a higher BC stage with longer yielding plateau, and a

gentler CD stage. This indicates that higher hollow ratio provides a weaker lateral confinement effect and acts an insignificant role in delaying concrete fracture. Additionally, Fig.3.19 also shows that the internal CSPs with different χ values fluctuate around abscissa axis with inapparent trend. This suggests that the hollow ratio has little effect on the internal CSPs, and internal tube provides less confinement effect to the concrete infill. Accordingly, the effects of the yield stress and diameter-to-thickness ratio of internal tube on the CSPs will not be further discussed in the next sections.

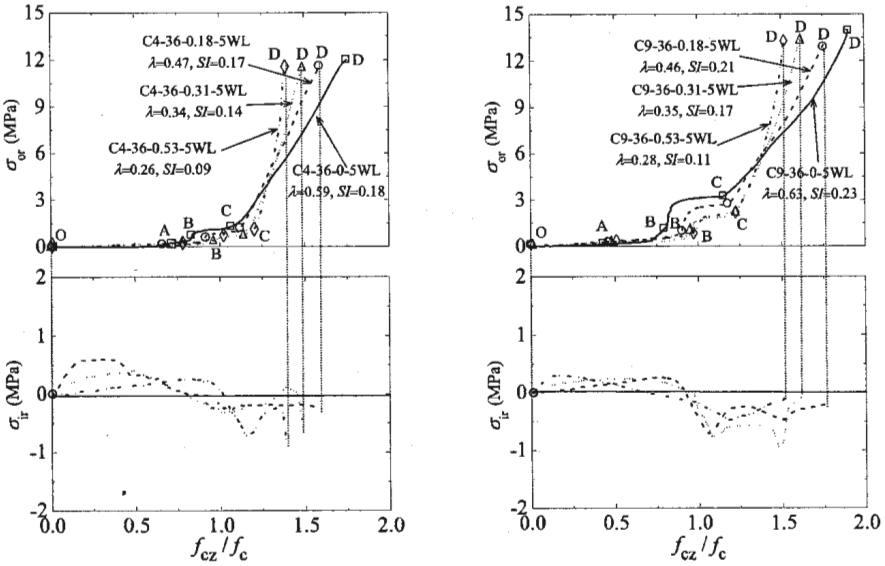

(a) G1 (C4) (b) G2 (C9)

Fig.3.19 CSPs for specimens with different χ values

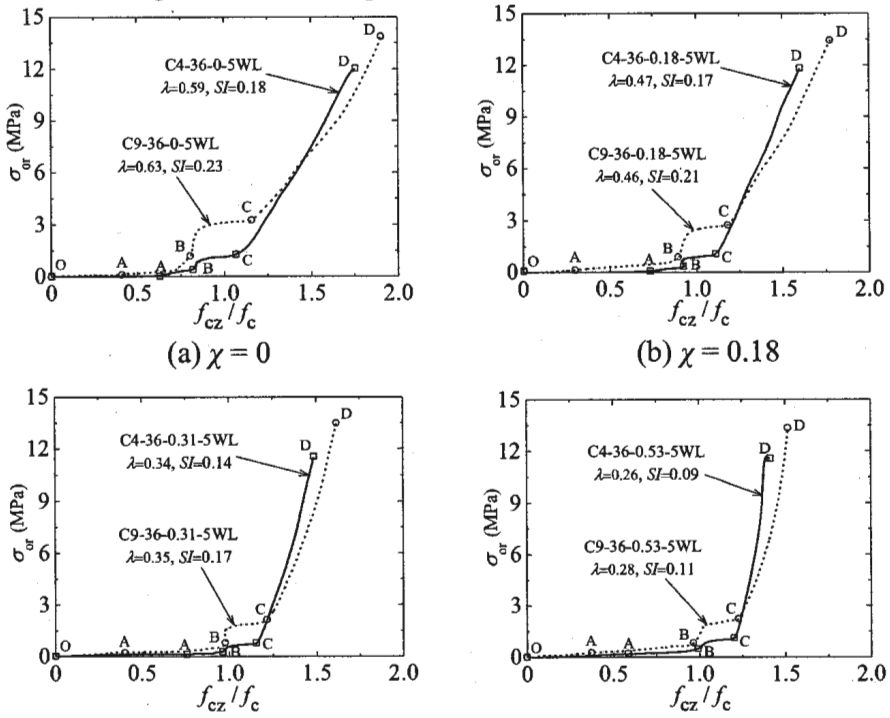

(a) $\chi = 0$ (b) $\chi = 0.18$

(c) $\chi = 0.31$ (d) $\chi = 0.53$

Fig.3.20 CSPs for specimens with different f_{syo} values

(2) Effects of f_{syo} on CSP

The effects of f_{syo} on the external CSPs of confined concrete in circular CFDST columns were examined against the test results of G1 and G2 specimens. The CSPs of the specimens with different f_{syo} values are shown Fig.3.20. From this figure, it can be seen that the external tube yield stress significantly affects the parts of the CSPs in the pre-fracture (OAB) and post-fracture (BCD) stages of the concrete infill. Compared with different f_{syo} values, the lateral stress in the specimen with a higher f_{syo} value appears to yield in an earlier stage, thus achieving a shorter OA part and a longer AB part. Additionally, the CSP in the specimen with a higher f_{syo} value tend to achieve a higher BC part with a longer plateau, and a longer and gentler CD part. This suggests that the specimens with a higher f_{syo} value exhibit better ductility performance due to higher confinement effect. This finding is consistent with that in axially loaded CFST column reported by the authors [30].

(3) Effects of f_c on CSP

The external and internal CSPs of confined concrete in the CFDST columns with different f_c values are shown in Fig.3.21. From this figure, it can be seen that the OABC parts of the external CSPs are similar, while differences are only found in the CD parts of the external CSPs. This indicates the concrete strength remarkably influences the CD part of the external CSPs during the strain hardening stage of the external tube. The CFDST column filled with a higher f_c value tends to achieve a shorter and steeper CD part. This suggests that the higher strength concrete undergoes a weaker lateral confinement effect under the identical confinement conditions, which is mainly attributed to the brittleness of high strength concrete. However, the concrete strength affords less contribution to the internal CSPs. Also, the inner tube provides an insignificant lateral confinement effect to the concrete infill, which is consistent with the observation in Section (1).

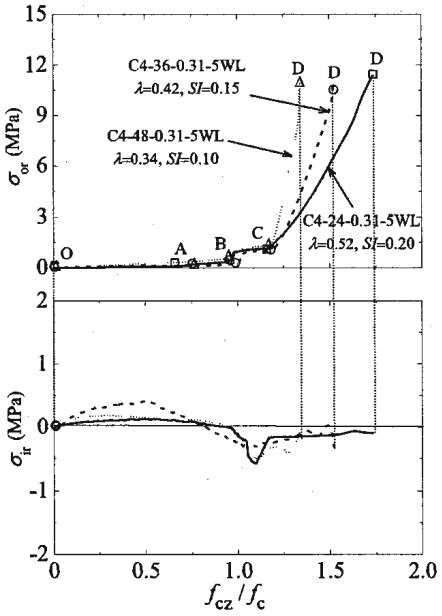

Fig.3.21 CSPs for specimens with different f_c values

(4) Effects of D_o/t_o ratio on CSP

The external and internal CSPs of confined concrete in the CFDST columns with different D_o/t_o ratios are shown in Fig.3.22. From this figure, it can be found that the D_o/t_o ratio yields an insignificant

effect on the OABC part of the external CSPs. Only differences are found in the length of the CD part of the external CSPs at when the external tube is in the strain hardening state. CFDST columns with a larger D_o/t_o ratio tend to generate a shorter CD part. This shows that the outer steel tubes with a larger D_o/t_o ratio provide a weaker lateral confinement effect, resulting in a lower ultimate axial load and ductility of the column. Additionally, the findings similar to Sections (1) and (3) were observed in this section for the internal CSPs.

As discussed above, the OB part (the pre-fracture stage of the concrete infill) of the external CSP is only influenced by f_{syo}, while the BC part of the external CSP is affected by both χ and f_{syo}. However, the CD part of the external CSP is almost influenced by all the examined variables. Different from the external CSP, the internal CSP is hardly affected by χ, f_{syo}, f_c and D_o/t_o ratio. Generally, the column parameters investigated yield significant effects on the external CSP, but less effects on the internal CSP.

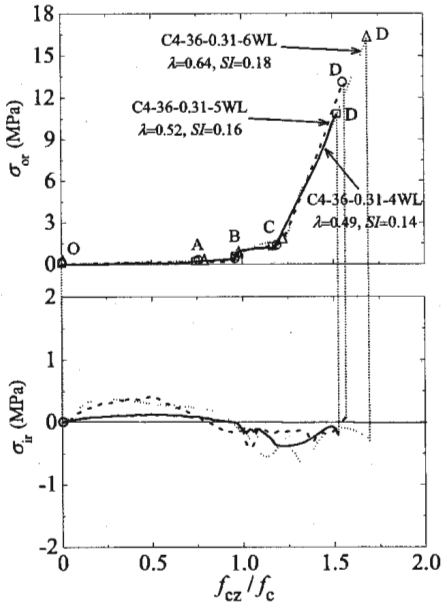

Fig.3.22 CSPs for specimens with different D_o/t_o ratios

(5) Relationship between *SI* and CSP

As defined above, the CSP of confined concrete in circular CFDST columns is represented by the domination index *SI*, calculated by Eq. (3.13). The values of *SI* for all the specimens are listed in Table 3.2. The mean value of *SI* for two identical specimens is also given in Figs.3.19 to 3.22 for their corresponding CSP. Since the external CSPs are influenced by χ, f_{syo}, f_c and D_o/t_o ratio, the domination index *SI* should be quantitatively expressed by these variables. The relationships between the domination index *SI* and column parameters, i.e., *SI* vs. χ, *SI* vs. f_{syo}/f_c, and *SI* vs. D_o/t_o ratio, are shown in Fig.3.23. The domination index *SI* decreases as the χ and D_o/t_o ratio increase, while it increases as the f_{syo}/f_c increases. This demonstrates that with increasing χ, f_c and D_o/t_o ratio, the CSP gets closer to the path P_0, which suggests that the lateral stress acts an insignificant role in the external CSP. On the contrary, with increasing f_{syo}, the CSP gets closer to the path P_a, which implies that the lateral stress acts a vital role in the external CSP.

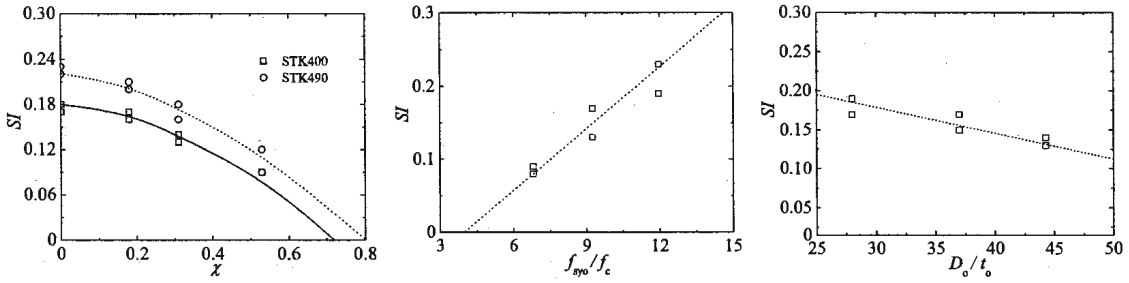

Fig.3.23 Relationships between laterally dominant index and variables investigated

3.4.2.3. CSP effect on the compressive strength

In this section, the influences of CSPs on the compressive strength of confined concrete are discussed. As defined above, such effect is characterized by an effect index λ; see Eq. (3.16). The values of λ for all the specimens are listed in Table 3.2, and the average value of λ of the two identical specimens for each CSP is also shown in Figs.3.19 to 3.22. It can be found that all the effect indices fall between 0 and 1. The reason for this is the equivalent CSPs of confined concrete in circular CFDST columns shift between those of the plain concrete and actively confined concrete. That is, the compressive strength (f_{cc}) of confined concrete in CFDST columns varies between f_c and f_{ac}, i.e., $f_{cc} \in (f_c, f_{ac})$.

The relationship between the effect index λ and domination index SI is depicted in Fig.3.24. In general, (a) the effect index λ for circular CFDST columns is smaller than the unity, i.e., $\lambda \neq 1.0$, which indicates that the compressive strength of confined concrete in circular CFDST columns is CSP-dependent; (b) the effect index λ is generally improved as the domination index SI enhances. This indicates that the CSP for CFDST column with a larger SI yields less significant impact on the compressive strength of confined concrete.

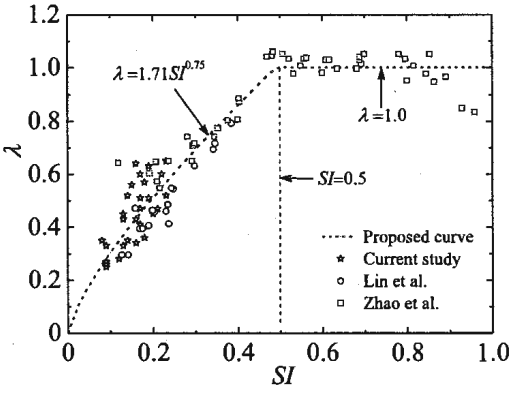

Fig.3.24 Relationship between effect index λ and domination index SI

It should be noted that the values of SI of the current study fall into the interval of (0.08, 0.23), for the purpose of generality, the values of the two indices λ and SI for circular CFST columns provided by Zhao et al. [29] and Lin et al. [34] are also depicted in Fig.3.24. The compressive strength of confined concrete is CSP-dependent for $SI \in (0,0.5)$, while it is CSP-independent for $SI \in [0.5,1]$. The relationship between the two indices λ and SI generally follows the observations given by Zhao et al. [29] and Lin et al. [34], a lightly modified model is proposed to interpret their relationship, as

given in Eq. (3.18). The proposed model is expressed in the form of a dash line in Fig.3.24. From this figure, it can be seen that, in general, the test results of the current and previous studies are evenly distributed on both sides of the dash line.

$$\lambda = \begin{cases} 1.71SI^{0.75}, & 0 \le SI < 0.5 \\ 1.0 & , 0.5 \le SI \le 1.0 \end{cases} \tag{3.18}$$

From Eq. (3.18), it can be noticed that once the domination index SI is determined, the value of the effect index λ will be obtained. As stated above, the domination index SI is influenced by the column parameters, i.e., χ, f_{syo}, f_c and D_o/t_o ratio. To reflect such effect, a confinement coefficient η considering these variables is defined as:

$$\eta = \left(1-\chi^2\right)\frac{2t_o}{D_o - 2t_o}\frac{f_{syo}}{f_c} \tag{3.19}$$

The relationship between the η and SI is illustrated in Fig.3.25. Based on the regression analysis of the test results, a model the reflects such relationship is developed as:

$$SI = 0.25\eta^{0.69} \tag{3.20}$$

Then, by substituting Eq. (3.20) into Eq. (3.18), Eq. (3.18) becomes the following equation:

$$\lambda_{CFDST} = \begin{cases} 0.60\eta^{0.51}, & 0 \le \eta < 2.731 \\ 1.0 & , 2.731 \le \eta \le 7.457 \end{cases} \tag{3.21}$$

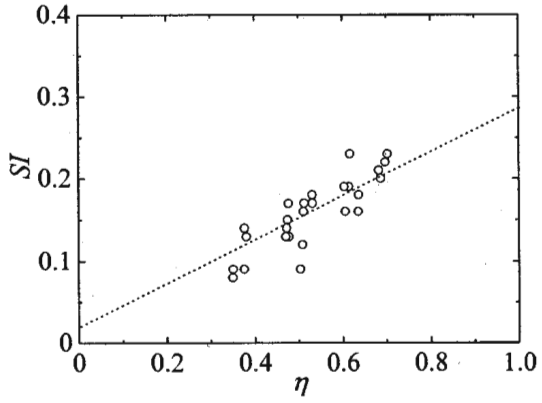

Fig.3.25 Relationship between SI and η

In order to well understand the confinement effects of circular CFDST and CFST columns, the relationships between the effect index λ and confinement coefficient η from such columns are depicted in Fig.3.26. In Fig.3.26, 'CL' denotes that only the concrete section of the column is subjected to axial load, while 'WL' indicates that the full section of the column is subjected to axial load. From Fig.3.26, it can be observed that:

(I) Similar to CFST columns, the effect indices of CFDST columns with a smaller η are smaller than the unity, which suggests that the compressive strength of confined concrete in CFDST columns with a smaller η is CSP-dependent.

(II) In general, the effect indices of CFDST column are less than those of CFST columns, which implies that the confinement effects of CFDST columns are weaker than those of CFST columns. Note that when the η is smaller than about 0.2, the effect indices of CFDST columns are nearly the same as those of CFST columns, which demonstrates that the confinement effects for both are almost identical. It is probably because columns with a smaller η (i.e., larger χ and D/t ratios (lead to premature buckling) or lower strength ratio f_y/f_c) have generally experienced a lower axial stress of steel tube, resulting in a higher circumferential stress of steel tube (according to the von Mises yield criterion).

(III) As the η increases, the effect indices of CFST and CFDST columns become the unity in turn, which suggests that the confinement effects for both are identical. Also, the compressive strength of confined concrete in columns with a larger η is CSP-independent.

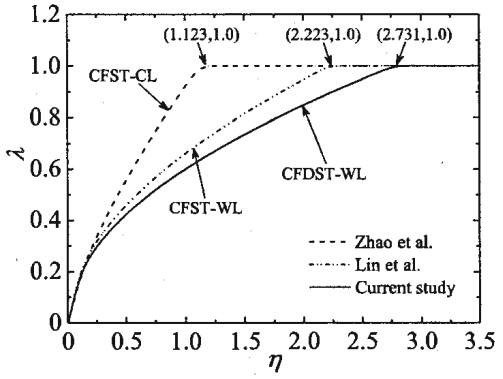

Fig.3.26 Effect index vs. confinement coefficient curves

Furthermore, based on Eq. (3.16), a compressive strength model of confined concrete in CFDST columns considering the CSP effect is given by:

$$f_{cc} = f_c + 2.2\lambda f_c^{0.3}\sigma_{ru}^{0.81} \tag{3.22}$$

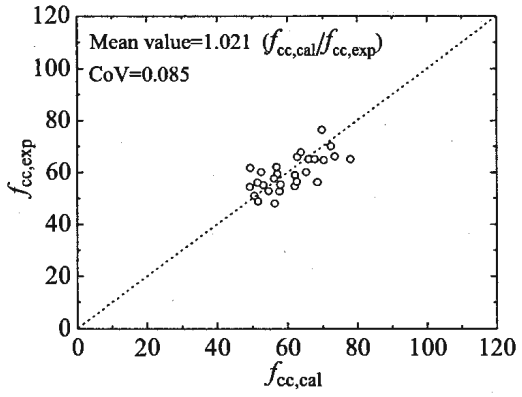

Fig.3.27 Verification of the developed model

In order to examine the performance of the developed model, comparison between the results calculated by the developed model and the measured results is shown in Fig.3.27. From this figure, the mean value and coefficient of variation (COV) of the predicted-to-test strengths are 1.021 and 0.085, respectively, which demonstrates that a higher prediction performance was achieved in the developed model. Simultaneously, it should be noted that the developed model can also be suitably

applied to predict the compressive strength of confined concrete in CFST columns by setting the hollow ratio (χ) to 0.

3.5. Conclusions

In total, 28 the entire-section axially loaded CFDST short columns fabricated using both outer and inner circular carbon steel tubes were tested, and the experimental results were compared with those of the concrete axially loaded CFDST short columns. Then, FE models verified based on the experimental results were developed to further investigate the differences in the mechanical behavior of the entire-section and concrete axially loaded CFDST columns. Additionally, based on the experimental tests, the confinement paths and the confinement path effects on the compressive strength of confined concrete in the entire-section axially loaded CFDST columns were studied in this paper. From the investigation, the following conclusions could be drawn:

1. The hollow ratio and yield strength of the external steel tube considerably affected the ultimate axial strengths of circular CFDST short columns. An increase of concrete strength and wall thickness of the external steel tube can effectively improve the compressive strengths of circular CFDST short columns.

2. For the specimens with the hollow ratio of 0 and 0.19, the ultimate strength of the entire-section axially loaded specimens is larger than that of the concrete axially loaded ones, while the opposite result is found for the specimens with the hollow ratio of 0.34 and 0.56. This indicates that the lateral confinement effect of outer and inner steel tubes to sandwiched concrete decreases as the hollow ratio increases.

3. The ultimate strength of the entire-section axially loaded specimens with the hollow ratio of 0.34 is larger than that of the concrete axially loaded ones. The ultimate strength of the entire-section axially loaded specimens is smaller than that of the concrete axially loaded ones at first, and then larger than that of the concrete axially loaded ones with the increase of the D_o/t_o ratio. This is mainly due to the stronger lateral confinement effect of the specimens with smaller D_o/t_o ratio (thicker wall thickness).

4. The external CSPs of CFDST columns are remarkably affected by the column variables investigated, i.e., χ, f_{syo}, f_c and D_o/t_o ratio, but less effects on the internal CSPs.

5. Similar to CFST columns under different types of loading, the effect indices of CFDST columns with a smaller η are smaller than the unity, which suggests that the compressive strength of confined concrete in the column with a smaller η is CSP-dependent.

6. The effect indices of CFDST column are generally less than those of CFST columns, which implies that the confinement effects of CFDST columns are weaker than those of CFST columns. Note that when the η is smaller than about 0.2, the effect indices of CFDST columns are nearly the same as those of CFST columns, which implies that the confinement effects for both are almost identical.

7. As the η enhances, the effect indices of CFST and CFDST columns become the unity in turn, which suggests that the confinement effects for both are identical. In other words, the compressive strength of confined concrete in the column with a larger η is CSP-independent.

8. A CSP-based compressive strength model of axially compressed circular CFDST short columns is proposed, and comparisons with existing models against the collected test data indicate a higher degree of accuracy and consistency of the predictions for the proposed model.

References

[1] Y.G. Zhao, X.F. Yan, S.Q. Lin, Compressive strength of axially loaded circular hollow centrifugal concrete-filled steel tubular short columns, Eng. Struct. 201 (2019) 109828.

[2] L.H. Han, W. Li, R. Bjorhovde, Developments and advanced applications of concrete-filled steel tubular (CFST) structures: members, J. Constr. Steel Res. 100 (2014) 211–228.

[3] F.X. Ding, Q. Fu, B. Wen, Q.S. Zhou, X.M. Liu, Behavior of circular concrete-filled steel tubular columns under pure torsion, Steel Compos. Struct. 26(4) (2018) 501–511.

[4] H.B. Ge, T. Usami, Strength of concrete-filled thin-walled steel box columns: experiment, J. Struct. Eng. 118(11) (1992) 3036–3054.

[5] J.F. Yang, X.F. Yan, P.P. Hu, G.P. Zhang, Z.H. Xi, Study on the bending performance of cantilever concrete-filled circular steel tubular long columns, J. Xi'an Univ. of Arch. & Tech. (Natural Science Edition) 48(5) (2016) 654–660.

[6] X.F. Yan, Y.G. Zhao, Compressive strength of axially loaded circular concrete-filled double-skin steel tubular short columns, J. Constr. Steel Res. 170 (2020) 106114.

[7] X.F. Yan, Y.G. Zhao, Experimental and numerical studies of circular sandwiched concrete axially loaded CFDST short columns, Eng. Struct. 230 (2021) 111617.

[8] H. Huang, L.H. Han, Z. Tao, X.L. Zhao, Analytical behavior of concrete-filled double skin steel tubular (CFDST)stub columns, J. Constr. Steel Res. 66(3) (2010) 542–555.

[9] Y.F. Yang, L.H. Han, B.H. Sun, Experimental behavior of partially loaded concrete filled double-skin steel tube (CFDST) sections, J. Constr. Steel Res. 71 (2012) 63–73.

[10] F.C. Wang, L.H. Han, W. Li, Analytical behavior of CFDST stub columns with external stainless steel tubes under axial compression, Thin-Walled Struct. 127 (2018) 756–768.

[11] M. Elchalakani, X.L. Zhao, R. Grzebieta, Tests on concrete filled double-skin (CHS outer and SHS inner) composite short columns under axial compression, Thin-Walled Struct. 40(5) (2002) 415–441.

[12] X.L. Zhao, R. Grzebieta, Strength and ductility of concrete filled double skin (SHS inner and SHS outer) tubes, Thin-Walled Struct. 40 (2002) 199–213.

[13] L.H. Han, Z. Tao, H. Huang, X.L. Zhao, Concrete-filled double skin (SHS outer and CHS inner) steel tubular beam-columns, Thin-Walled Struct. 42(9) (2004) 1329-1355.

[14] Z. Tao, L.H. Han, X.L. Zhao, Behavior of concrete-filled double skin (CHS inner and CHS outer) steel tubular stub columns and beam columns, J. Constr. Steel Res. 60(8) (2004) 1129–1158.

[15] Z. Tao, L.H. Han, Behavior of concrete-filled double skin rectangular steel tubular beam columns, J. Constr. Steel Res. 62(7) (2006) 631–646.

[16] K. Uenaka, H. Kitoh, K Sonoda, Concrete filled double skin circular stub columns under compression, Thin-Walled Struct. 48 (2010) 19-24.

[17] Y. Essopjee, M. Dundu, Performance of concrete-filled double skin circular tubes in compression, Compos. Struct. 133 (2015) 1276–1283.

[18] T. Ekmekyapar, H.G. Hasan, The influence of the inner steel tube on the compression behavior of the concrete filled double skin steel tube (CFDST) columns, Mar. Struct. 66 (2019) 197–212.

[19] W. Li, Y.X. Cai, Performance of CFDST stub columns using high-strength steel subjected to axial compression, Thin-Walled Struct. 141 (2019) 411–422.

[20] H.T. Hu, F.C. Su, Nonlinear analysis of short concrete-filled double skin tube columns subjected to axial compressive forces, Mar. Struct. 24 (2011) 319–337.

[21] M.F. Hassanein, O.F. Kharoob, Compressive strength of circular concrete-filled double skin tubular short columns, Thin-Walled Struct. 77 (2014) 165–173.

[22] Q.Q. Liang, Nonlinear analysis of circular double-skin concrete-filled steel tubular columns under axial compression, Eng. Struct. 131(15) (2017) 639–650.

[23] L.H. Han, Q.X. Ren, W. Li, Tests on stub stainless steel-concrete-carbon steel double-skin tubular (DST) columns, J. Constr. Steel Res. 67(3) (2011) 437–452.

[24] F.Y. Wang, B. Yong, L. Gardner, Compressive testing and numerical modelling of concrete-filled double skin CHS with austenitic stainless steel outer tubes, Thin-Walled Struct. 141 (2019) 345–359.

[25] M.F. Hassanein, O.F. Kharoob, Q.Q. Liang, Circular concrete-filled double skin tubular short columns with external stainless steel tubes under axial compression, Thin-Walled Struct. 73 (2013) 252–263.

[26] ABAQUS Standard User's Manual. The Abaqus Software is a product of Dassault Systemes Simulia Corp. Providence, RI, USA Dassault Systemes, Version 6.8, USA, 2008.

[27] F.E. Richart, A. Brandtzaeg, A. Brown, A study of the failure of concrete under combined compressive stresses. Bulletin No. 185, Champaign (IL, USA): University of Illinois, Engineering Experimental Station; 1928.

[28] J.B. Mander, M.J.N. Priestley, R. Park, Theoretical stress-strain model for confined concrete, J. Struct. Eng. 114 (1988) 1804–1826.

[29] Y.G. Zhao, S.Q. Lin, Z.H. Lu, T. Saito, L.S He, Loading paths of confined concrete in circular concrete loaded CFT stub columns subjected to axial compression, Eng. Struct. 156 (2018) 21–31.

[30] S.Q. Lin, Y.G. Zhao, J.M. Li, Z.H. Lu, Confining stress path based compressive strength model of axially loaded FRP-confined columns, J. Compos. Constr. 25(1) (2021) 04020077.

[31] E. Farajpourbonab, Effective parameters on the behavior of CFDST columns, J. Applied Eng. Sci. 15(1) (2017) 99–108.

[32] X.F. Yan, C. Yang, Experimental research and analysis on residual stress distribution of circular steel tubes with different processing techniques, Thin-Walled Struct. 144 (2019) 106268.

[33] Z. Tao, Z.B. Wang, Q. Yu, Finite element modelling of concrete-filled steel stub columns under axial compression, J. Constr. Steel Res. 89 (2013) 121-131.

[34] S.Q. Lin, Y.G. Zhao, L.S. He, Stress paths of confined concrete in axially loaded circular concrete-filled steel tube stub columns, Eng. Struct. 173 (2018) 1019–1028.

CHAPTER 4. COMPRESSIVE STRENGTH OF CIRCULAR ENTIRE-SECTION AXIALLY LOADED CFDST SHORT COLUMNS

4.1. Introduction

Concrete-filled steel tubes (CFSTs) are widely used in industrial construction, civil architectures, and public buildings owing to their excellent load-carrying capacities, high stiffness and ductility, and superior seismic performance [1-4]. As a member of CFSTs family, concrete-filled double-skin steel tubular (CFDST) columns with concrete infilled between the two steel tubes possess lighter weight, higher bending stiffness, and better cyclic performance than their CFST counterparts [5,6]. They can be applied in the sea-bed vessels, legs of offshore platforms in deep water, bridge piers, and transmission tower [7-10]. It has been shown that the mechanical and economic benefits from such columns can be further improved by using high strength materials, such as high strength concrete or steel [11-13].

With the rapid development of concrete technology, the production of high-strength concrete (HSC) has become more accessible by adding a small amount of admixtures, such as silica fume, super plasticizer, or steel fiber [14,15]. In accordance with European Code EN 1992-1-1 (EC2) [16], the concrete is temporarily categorized as normal-strength concrete (NSC), HSC and ultrahigh-strength concrete (UHSC) with the compressive strengths of 50 MPa and 90 MPa as the boundaries. High performance HSC (or UHSC) is well liked in construction of deep foundations, high-rise buildings, and longspan bridges owing to the following reasons [17,18]: (1) reduce the cross-sectional size of column and save economy; (2) maximize useable floor space; (3) accelerate construction by filling concrete with minimum compactness; (4) improve urban environment by reducing carbon from the use of steel.

Despite such advantages of HSC, up to now, however, experimental studies on the compressive behaviour of CFDST columns with HSC infilled between two circular carbon steel tubes have been very scarce [19-23,26]. Wei et al. [19] investigated the compressive behaviour of circular CFDST stub columns filled using polymer concrete with the compressive strength of 58.6 MPa, and the influences of column parameters on the cross-sectional strengths were evaluated. Zhao et al. [20] experimentally investigated the compressive behaviour of CFDST stub columns fabricated using cold-formed circular hollow sections with the standard concrete cylinder strength of 60.9 MPa. Previous theoretical models for the cross-sectional strengths were examined on the basis of the conducted test results, and a simple prediction model was proposed. Furthermore, Zhao et al. [21] conducted a series of experimental tests on circular CFDST columns with the standard concrete cylinder strength of 60.9 MPa subjected to large deformation axial loading. Results show that the load drop during cyclic loading is insignificant. Ekmekyapar and Hasan [22] experimentally investigated the effects of the internal tubes upon the compressive behaviour of CFDST columns with the maximum standard concrete cylinder strength of 64.6 MPa, and the applicability of the existing strength prediction models were investigated. Besides, Ekmekyapar et al. [23] also performed a comparison of classical, double skin and double section CFST stub columns with the maximum standard concrete cylinder strength of 68.2 MPa based on the experimental procedures. For design purposes, the modified versions of EC4 [24] and AISC 360-16 [25] to the design of composite members were evaluated against the test results. Yan and Zhao [26] experimentally examined the performance of axially compressed CFDST columns with the maximum standard concrete cylinder strength of 51.0 MPa. The applicability of existing strength prediction models for CFDST columns

was assessed based on the conducted and collected test data, and a novel strength prediction formula was proposed.

From the above literature review, it can be found that the concrete strength of the existing tested CFDST columns with HSC are only limited between 50 MPa and 68.2 MPa, which is very close to the boundary between NSC and HSC. As a result, the applicability of the existing empirical models, which were developed based on the limited experimental data, is doubtful for HSC or UHSC, and needs to be further assessed for a wider range of column parameters. To fill the current research gap, therefore, it is necessary to carry out further experimental study on the axial compression behavior of circular CFDST short columns with HSC or UHSC, and then proposed a more accurate strength prediction model than the existing models.

The purpose of this paper is to experimentally and numerically investigate the behaviour of axially compressed circular HSC and UHSC filled CFDST short columns with outer and inner carbon steel tubes. The remainder of this paper is outlined as below: In Section 2, a comprehensive experimental program that includes 24 CFDST column specimens is carried out. The influences of various parameters on the failure modes, ultimate strengths, post-peak ductility, and axial load-shortening response of such columns are discussed; In Section 3, a finite element (FE) model is established and verified against the test results; In Section 4, using the verified FE model, the interaction of the steel tubes and concrete and the load distribution on components are analysed, and the parametric study is conducted to further ascertain the influences of column variables on the compressive behaviour of the CFDST columns. In Section 5, the applicability of the existing design codes and empirical models to design the CFDST columns is evaluated based on the test results in the present and previous studies, and a more accurate strength prediction model is proposed. Finally, Section 6 draws the conclusions.

4.2. Experimental investigation

4.2.1. Test specimens

A total of 24 test experiments were performed to investigate the compressive behavior of axially loaded circular CFDST stub columns with HSC and UHSC, as shown in Table 4.1. In this table, $N_{u,e}$ represents the ultimate axial strengths of columns, f_c denotes the standard concrete cylinder strength (150 mm in diameter and 300 mm in height), f_{syo} and f_{syi} symbolize the yield strengths of external and internal tubes, respectively. The cross-sectional diagram of a typical CFDST column is depicted in Fig.4.1. In this figure, D_o symbolizes the outside diameter of the external tube, and the corresponding wall thickness is t_o; D_i and t_i denote the outside diameter and wall thickness of the internal tube, respectively. In accordance with Japanese Standard JIS G 3444-2015 [27], in this study, four different sectional sizes of circular hollow steel (CHS) tubes are selected as the external and inner tubes. The STK400 CHS tubes with the nominal size of 165.2 × 3.7 mm (diameter × thickness) and 165.2 × 6.0 mm as well as the STK490 tubes with the nominal size of 165.2 × 6.0 mm are employed as the external tubes. The internal tubes use STK400 CHS tubes with the nominal size of 42.7 × 3.2 mm and 76.3 × 2.8 mm, respectively. Geometrical measurements were conducted, and the diameter and wall thickness of the cross-sectional size were measured by a vernier caliper made in Japan. The measured results are listed in Table 4.1.

The CHS tubes were cut to the size required for the experiments. Before fixation, the bidirectional strain gauges were pasted on the outside wall of the internal CHS tubes and protected by a waterproof

Table 4.1. Details of 24 tested circular CFDST short column specimens

Series	Specimens	$D_o \times t_o$ (mm)	D_o/t_o	f_{syo} (MPa)	$D_i \times t_i$ (mm)	D_i/t_i	f_{syi} (MPa)	χ (D_i/D_o)	f_c (MPa)	$N_{u,e}$ (kN)	SI	DI	$N_{u,FE}$ (kN)	$N_{u,FE}/N_{u,e}$
Series 1	C4-46-0.26-3.7-1	165.2 × 3.68	44.9	357.7	42.5 × 3.19	13.3	409.8	0.26	53.7	2060	1.14	4.98	1898	0.921
	C4-46-0.26-3.7-2	164.9 × 3.69	44.7	357.7	42.7 × 3.20	13.3	409.8	0.26	53.7	2003	1.11	4.79	1898	0.948
	C4-83-0.26-3.7-1	165.0 × 3.68	44.8	357.7	42.6 × 3.21	13.3	409.8	0.26	90.7	2423	0.98	2.33	2512	1.037
	C4-83-0.26-3.7-2	165.1 × 3.70	44.6	357.7	42.7 × 3.19	13.4	409.8	0.26	90.7	2446	0.99	2.29	2512	1.027
	C4-130-0.26-3.7-1	164.8 × 3.69	44.7	357.7	42.6 × 3.20	13.3	409.8	0.26	141.0	3068	0.91	1.85	3412	1.112
	C4-130-0.26-3.7-2	164.9 × 3.69	44.7	357.7	42.5 × 3.20	13.3	409.8	0.26	141.0	3110	0.92	1.97	3412	1.097
Series 2	C4-46-0.46-3.7-1	165.0 × 3.70	44.6	357.7	76.0 × 2.80	27.1	385.6	0.46	53.7	1831	1.06	2.90	1839	1.004
	C4-46-0.46-3.7-2	165.0 × 3.70	44.6	357.7	76.2 × 2.79	27.3	385.6	0.46	53.7	1876	1.09	2.84	1839	0.980
	C4-83-0.46-3.7-1	165.1 × 3.67	45.0	357.7	76.1 × 2.81	27.1	385.6	0.46	90.7	2174	0.96	1.51	2400	1.104
	C4-83-0.46-3.7-2	165.2 × 3.69	44.8	357.7	76.4 × 2.80	27.3	385.6	0.46	90.7	2202	0.97	1.43	2400	1.090
	C4-130-0.46-3.7-1	164.8 × 3.68	44.8	357.7	76.3 × 2.80	27.3	385.6	0.46	141.0	2732	0.91	1.35	2885	1.056
	C4-130-0.46-3.7-2	164.7 × 3.71	44.4	357.7	76.1 × 2.78	27.4	385.6	0.46	141.0	2736	0.91	1.27	2885	1.054
Series 3	C4-46-0.46-6.0-1	165.3 × 5.96	27.7	347.0	76.1 × 2.79	27.3	385.6	0.46	53.7	2183	1.07	3.22	2045	0.937
	C4-46-0.46-6.0-2	165.0 × 5.99	27.5	347.0	76.2 × 2.81	27.1	385.6	0.46	53.7	2203	1.08	3.35	2045	0.928
	C4-83-0.46-6.0-1	164.9 × 6.01	27.4	347.0	75.9 × 2.80	27.1	385.6	0.46	90.7	2666	1.05	2.34	2920	1.095
	C4-83-0.46-6.0-2	164.8 × 6.00	27.5	347.0	75.8 × 2.80	27.1	385.6	0.46	90.7	2631	1.04	2.26	2920	1.110
	C4-130-0.46-6.0-1	164.9 × 6.01	27.4	347.0	76.0 × 2.81	27.0	385.6	0.46	141.0	3110	0.96	1.77	3389	1.090
	C4-130-0.46-6.0-2	164.8 × 6.00	27.5	347.0	76.1 × 2.78	27.4	385.6	0.46	141.0	3032	0.94	1.84	3389	1.118
Series 4	C9-46-0.46-6.0-1	165.2 × 5.95	27.8	428.6	76.1 × 2.79	27.3	385.6	0.46	53.7	2645	1.17	5.31	2634	0.996
	C9-46-0.46-6.0-2	165.0 × 5.96	27.7	428.6	76.0 × 2.79	27.2	385.6	0.46	53.7	2601	1.15	5.19	2634	1.013
	C9-83-0.46-6.0-1	165.0 × 5.99	27.5	428.6	75.8 × 2.80	27.1	385.6	0.46	90.7	2971	1.07	3.82	3212	1.081
	C9-83-0.46-6.0-2	165.0 × 6.01	27.5	428.6	75.9 × 2.78	27.3	385.6	0.46	90.7	2911	1.04	3.77	3212	1.103
	C9-130-0.46-6.0-1	165.1 × 5.94	27.8	428.6	75.9 × 2.80	27.1	385.6	0.46	141.0	3322	0.95	2.31	3566	1.073
	C9-130-0.46-6.0-2	164.9 × 6.02	27.4	428.6	76.1 × 2.80	27.2	385.6	0.46	141.0	3304	0.95	2.24	3566	1.079
	Mean													1.044
	CoV													0.061

tape. The data output lines connected to the strain gauges were extended along the outside wall of the internal CHS tube and placed into its inner hole. Through spot welding, the external and internal CHS tubes were simultaneously welded on the same bottom endplate so that they located in the same center. The column specimens were poured with concrete with the nominal cylinder compressive strength of 46 MPa, 83 MPa and 130 MPa. Due to the shrinkage of concrete at the top end during the curing period, the specimens were trimmed with concrete mortar to keep the steel tubes and concrete in the same plane. The bottom endplate was removed after the curing stage of concrete was finished. The prepared specimens are shown in Fig.4.2. The ratio (L/D_o) of the nominal short column length-to-outside diameter of external tube is maintained at a constant value of 3 to avoid overall buckling.

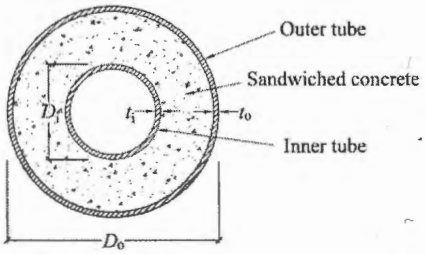

Fig.4.1 Definition of cross-section of circular CFDST columns

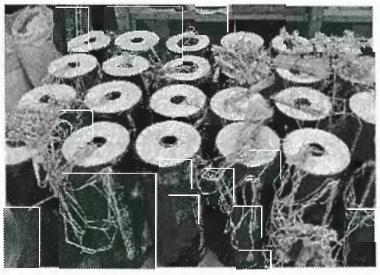

Fig.4.2 The preparation of specimens

4.2.2. Specimen labelling

For simplicity, the tested CFDST columns are generally marked as: the section shape of columns, material grade of external tube, strength grade of concrete, hollow ratio, nominal wall thickness of external tube, and number of identical specimens, as shown in Table 4.1. For instance, the label "C4-46-0.26-3.7-1" defines the following specimen: The first letter "C" means the CHS; number "4" refers to the STK400; number "46" after the first en dash indicates the nominal cylinder compressive strength of concrete, 46 MPa; number "0.26" after the second en dash denotes the hollow ratio ($\chi = D_i/D_o$) of column; number "3.7" after the third en dash denotes the nominal wall thickness of external tube, 3.7 mm; number "1" after the fourth en dash symbolizes the first test body of identical specimens in each set.

4.2.3. Material properties

4.2.3.1. External and internal steel tubes

The tensile coupon tests on external and internal tubes were launched to determine their material properties, and the test setup for tensile coupon tests is shown in Fig.4.3. The tensile coupons were longitudinally cut from the curved face of the CHS tubes with the same parent material as the test specimens. Each coupon was manufactured with a parallel width of 12.5 mm and 36 mm gauge. The

two ends of coupons were fixed using the grips located in the MTS tensile machine with a displacement control, as shown in Fig.4.3(b). Two strain gauges were pasted to the front and back of the coupon centroid to monitor the compatibility of strain changes in the plane, and a Shimazu video noncontact extensometer TRViewX was used to measure the change of the gauge length, as shown in Fig.4.3(a). A constant displacement rate of 0.2 mm/min was utilized throughout the loading process. The measured engineering stress-strain curves for the external and internal tubes are depicted in Fig.4.4, and the corresponding material properties are listed in Table 4.2.

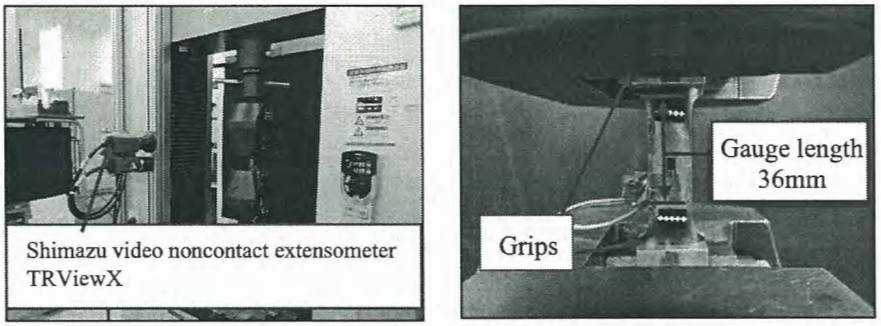

(a) (b)

Fig.4.3 Test setup for tensile coupon tests

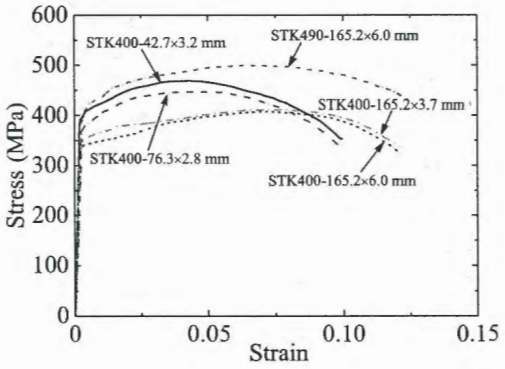

Fig.4.4 Measured stress-strain curves for steel CHS tubes

Table 4.2. Material properties of external and internal tubes

Type of steel	Location	Nominal sectional size (mm)	f_{sy} (MPa)	f_{su} (MPa)	E_o (GPa)	ε_f (%)
STK400	Internal tube	42.7 × 3.2	409.8	466.7	200.1	17.0
		76.3 × 2.8	385.6	445.9	198.5	17.4
	External tube	165.2 × 3.7	357.7	410.6	202.6	18.9
		165.2 × 6.0	347.0	409.8	203.1	19.1
STK490	External tube	165.2 × 6.0	428.6	500.1	199.7	20.3

4.2.3.2. Concrete

The material properties of the concrete used were obtained from the standard concrete cylinder tests. According to the American Standard ACI 318 [28], the dimensions of standard concrete cylinder are specified as 150 mm in diameter and 300 mm in height. Three concrete strength grades including C46, C83 and C130 were made from commercially available materials. The mix design of the concrete used is listed in Table 4.3. At 28 days, six standard concrete cylinder specimens for C46,

C83 and C130 were tested, and their strengths are 49.6, 87.7 and 137.4 MPa with the coefficients of variation of 0.034, 0.012 and 0.019, respectively. The rest of the specimens were tested together with the corresponding CFDST column specimens on the test day, and their strengths are 53.7 MPa, 90.7 MPa and 141.0 MPa for C46, C83 and C130, respectively, as shown in Table 4.4.

Table 4.3. Mix design of concrete

Concrete grades	Water/cement ratio	Mix proportions (to the weight of cement)					
		Cement	Water	Fine aggregate	10 mm aggregate	SP	CSF
C46	0.52	1.00	0.52	1.52	2.41	0.005	0
C83	0.26	1.00	0.26	1.24	1.89	0.026	0.04
C130	0.16	1.00	0.16	1.01	1.45	0.060	0.12

Note: SP represents the super plasticizer; CSF represents the condensed silica fume

Table 4.4. Measured strength of concrete cylinders

Nominal concrete strength (MPa)	Average concrete strength at 28 days (MPa)	Coefficient of variation (CoV)	Number of cylinder tests	Average concrete strength at test day (MPa)	Coefficient of variation (CoV)	Number of cylinder tests
C46	49.6	0.034	2	53.7	0.012	4
C83	87.7	0.012	2	90.7	0.009	4
C130	137.4	0.019	2	141.0	0.021	4

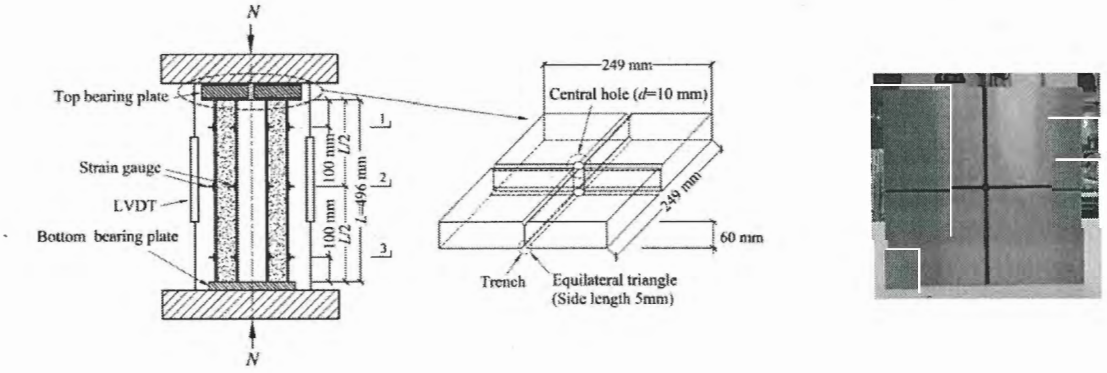

(a) (b) (c)

Fig.4.5 Schematics of loading device

4.2.4. Column test procedures

The schematic diagram of the loading device is illustrated in Fig.4.5. A universal testing machine equipped with the ultimate compression capacity of 5000 kN was utilized for loading all the specimens. Fig.4.5(a) shows that axial compressive loads acting on both ends of all the specimens are applied through the top and bottom bearing plates. As shown in Fig.4.5(b), the top bearing plate was made with two 5 mm equilateral triangular trenches that are perpendicular to each other at the top and bottom, and a hole with a diameter of 10 mm was dug at the intersection of the trenches. The physical

picture of the top bearing plate is shown in Fig.4.5(c). Twelve pairs of two-way strain gauges were pasted at the outside surface of external and internal tubes to obtain the longitudinal and transverse strains of the corresponding measured positions, as shown in Fig.4.5(a). Through the trench and central hole in the top bearing plate, the data lines of the strain gauges pasted to the outside surface of the internal tubes were pulled out for test data collection. A circuit diagram of gauge lines (red lines) of the inner tube is shown in Fig.4.6. After the strain lines passed through the trenches in the upper surface of the top bearing plate (see Fig.4.7(b)), the top bearing plate was adjusted to align with the test body, and then the upper loading ram of the testing machine was lowered to prepare for the test. In addition, to monitor if the tested specimens occurred twist in the load plane and measure the corresponding axial-shortening deformation, two Linear Variable Differential Transformers (LVDTs) were employed. A data acquisition system was utilized to write down changes in axial loads during the test process as well as the readings of LVDTs and strain gauges. The actual test setup is also shown in Fig.4.7.

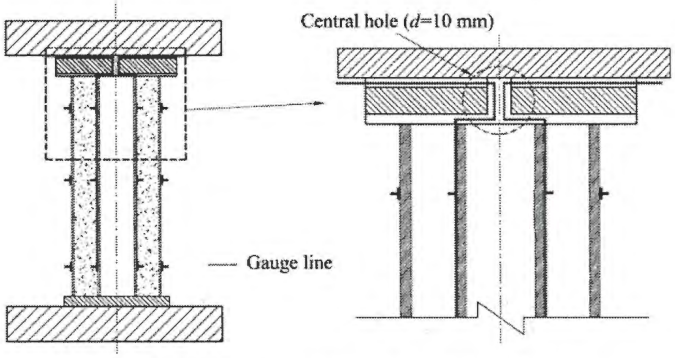

Fig.4.6 Circuit diagram of gauge lines

(a) Axial loading (b) Top surface of top bearing plate

Fig.4.7 Test setup

4.2.5. Test results and discussions

4.2.5.1. Failure modes

During the loading process, after reaching the ultimate strength, due to the weak mutual restraint between the steel tubes and concrete at both ends of the specimens, the elephant foot appeared at both ends of the specimens. As the axial deformation continues, the outward buckling occurred at the mid-height of the specimens, and the loading was terminated when the axial displacement reached about 30 mm. After the experimental tests, the two failure modes of the tested CFDST columns were observed, typical examples of which are presented in Fig.4.8. From Figs.4.8 (a) and (b), it can be

found that the outward local buckling deformation occurs at the mid-height of the outer tube, whereas the inner tube exhibits the inward local buckling deformation at the same location. That's mostly because of the mutual extrusion between the steel tubes and concrete infilled. This failure phenomenon is consistent with those of the experimental tests reported previously in Ref. [26].

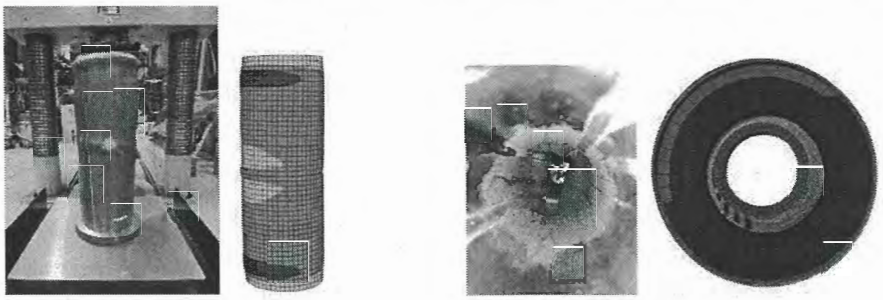

(a) External skin (b) Internal skin

Fig.4.8 The typical failure modes of the specimen C4-83-0.46-6.0-1

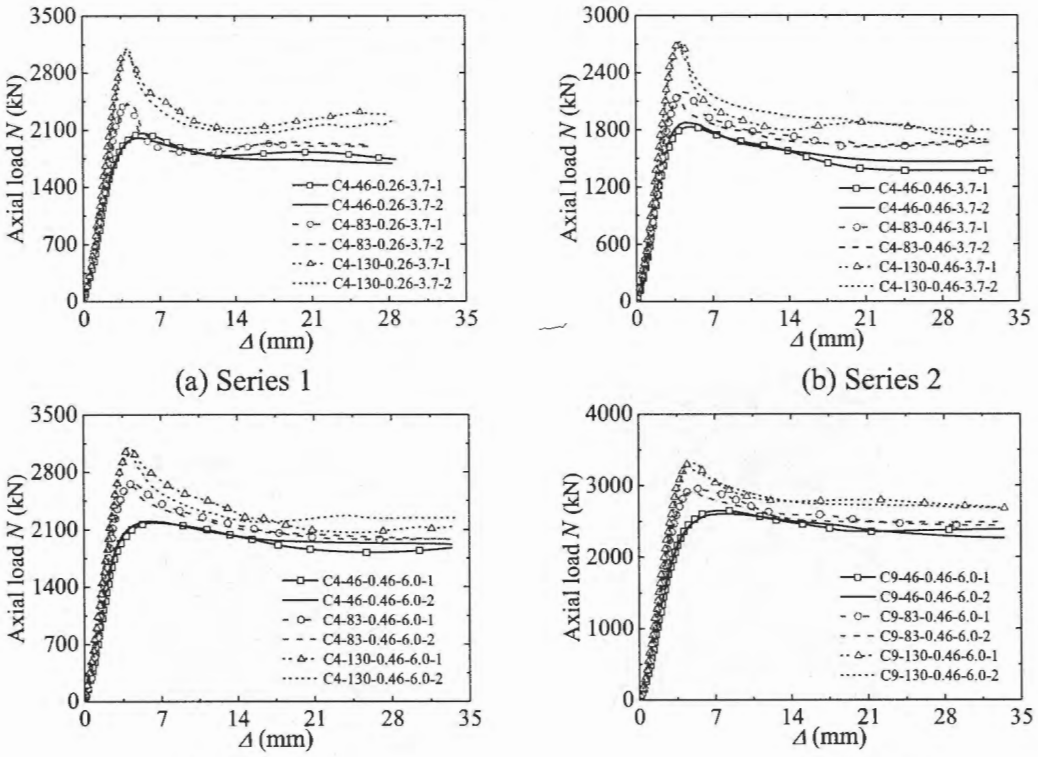

(a) Series 1 (b) Series 2

(c) Series 3 (d) Series 4

Fig.4.9 Axial load versus displacement curves of the tested CFDST columns

4.2.5.2. Axial load versus displacement curves

The axial load (N) vs. displacement (Δ) curves of all specimens are illustrated in Fig.4.9, in which N is extracted from the pressure sensor installed in the universal testing machine and Δ is read by using the LVDTs. From Fig.4.9, it can be noticed that before reaching the ultimate loads, the N-Δ curves of all measured columns undergo an elastic and elastoplastic stage. In this range, the initial stiffness of CFDST columns is improved with the increase in the concrete strength. After the ultimate load is reached, the N-Δ curves enter the descending stage. Columns with different concrete grades

exhibit distinct descending trends in the *N-Δ* curves. As the concrete strength increases, the descending trend changes from gentle to steep, which shows that the tested CFDST columns undergo from ductile failure to brittle failure. That's mostly because the higher the concrete strength, the greater the brittleness. This causes the interaction between the steel tubes and concrete infilled to be underplayed. It is worth noting that the *N-Δ* curves tend to gentle after descending stage and experience relatively longer level behaviour. In addition, one can see clearly that the specimens have high post-yield residual strength, which may be attributed to the good confinement effect between the steel tubes and concrete infill.

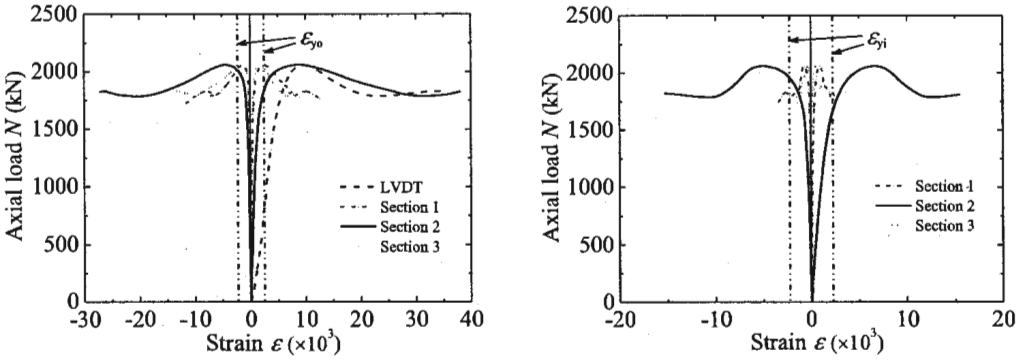

(a) Outer tube (b) Inner tube

Fig.4.10 Axial load vs. longitudinal and hoop strain curves of the specimen C4-46-0.26-3.7-1

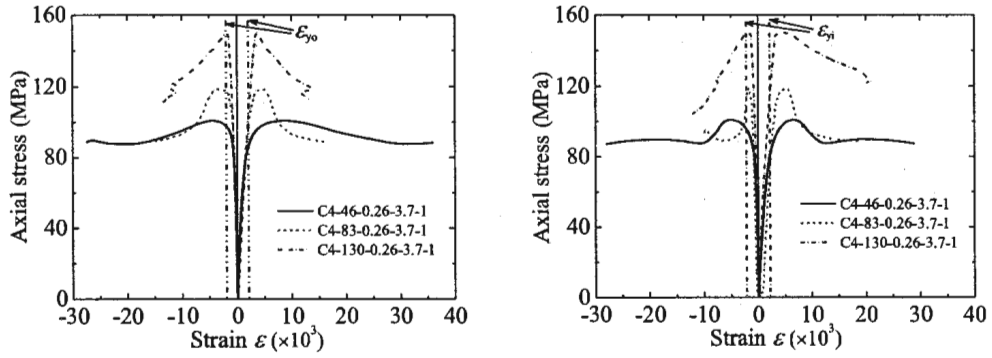

(a) Outer tube (b) Inner tube

Fig.4.11 Axial stress vs. strain curves of the specimens with different concrete strengths

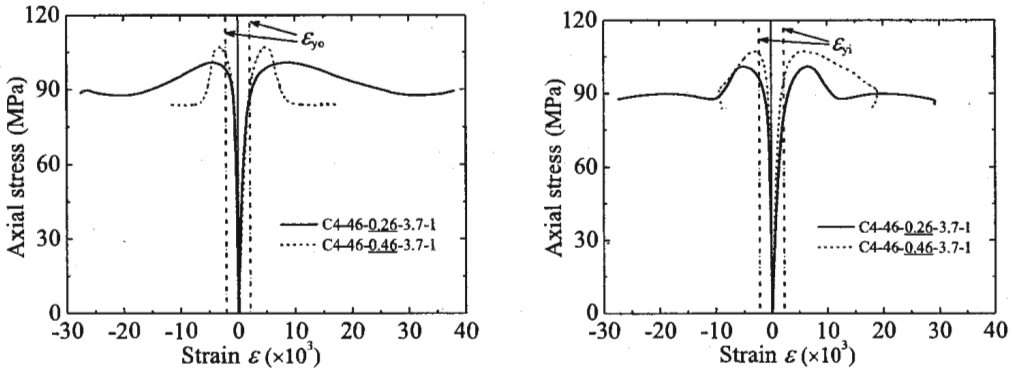

(a) Outer tube (b) Inner tube

Fig.4.12 Axial stress vs. strain curves of the specimens with different hollow ratios

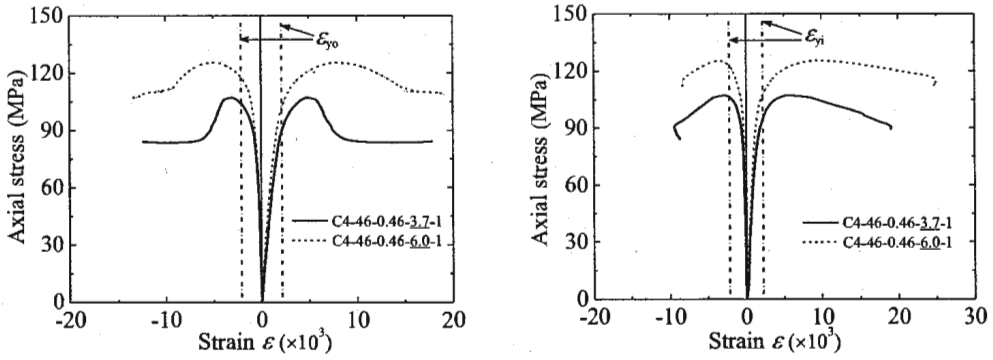

(a) Outer tube (b) Inner tube

Fig.4.13 Axial stress vs. strain curves of the specimens with different outer tube wall thicknesses

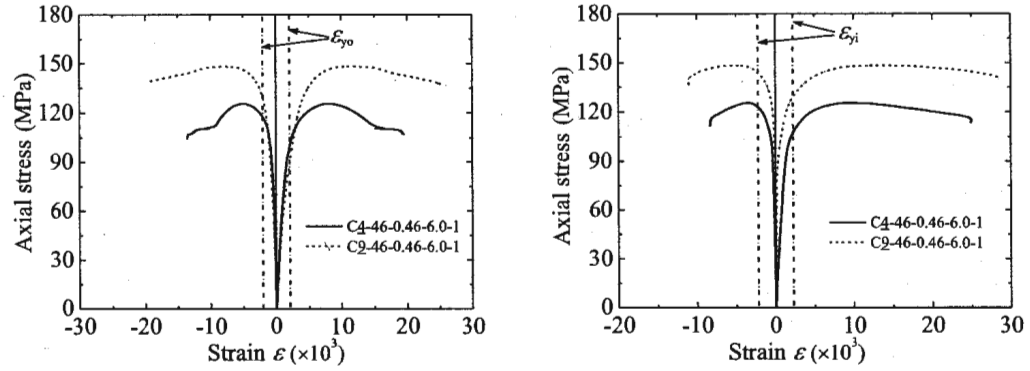

(a) Outer tube (b) Inner tube

Fig.4.14 Axial stress vs. strain curves of the specimens with different outer tube yield stresses

4.2.5.3. Strain response

To assess the differences between the readings of the strain gauges located at different heights and the LVDTs, the specimen C4-46-0.26-3.7-1 was employed and its typical axial load vs. longitudinal and hoop strain curves are shown in Fig.4.10. In Fig.4.10, ε_{yo} and ε_{yi} stand for the yield strains of the outer and inner tubes, and their values are 2003 $\mu\varepsilon$ and 2215 $\mu\varepsilon$, respectively. In this paper, the longitudinal compressive strain is taken as positive, while the hoop tensile strain is taken as negative. From Fig.4.10, it can be seen that with the increase of the axial deformation, the longitudinal and hoop strains of the outer and inner tubes at the section 2, i.e. the middle height of column (see Fig.4.5) develop faster than those at the sections 1 and 3. The strains at the ultimate load at the section 2 are larger than the yield strains of the outer and inner tubes, while the strains at the ultimate load at the sections 1 and 3 are smaller than the yield strains of the outer and inner tubes. This indicates the steel tubes at the sections 1 and 3 do not enter the yield stage at ultimate load, and their strains can't really reflect the overall deformation of the column due to the complex boundary conditions at the ends. Therefore, the strains of the steel tubes at the section 2 are usually used to reflect the overall deformation of columns. Besides, it can be found from Fig.4.10(a) that the axial load vs. strain curves obtained from the LVDTs and the strain gauges at the section 2 are basically consistent except for a small deviation before the ultimate load. This deviation is mainly due to the compatibility of the strain gauge readings adhered to the symmetrical position at the section 2 and the accuracy of LVDT readings, as well as many unavoidable factors in the loading process.

Additionally, based on the above observation, the axial stress vs. strain curves at the section 2 of the typical specimens are shown in Fig.4.11 to Fig.4.14 to further investigate the effects of key variables on the overall deformation of the columns. It should be noted that axial stress, i.e., the axial load of the column divided by the whole section area, is employed to account for the different section areas of the specimens. From Fig.4.11, it can be seen that with the increase of concrete strength, the ultimate axial stresses of the specimens are improved but their ductility is reduced. Besides, as the concrete strength increases, the absolute strain value at ultimate axial stress of the specimens becomes smaller. This is mainly due to the brittleness of HSC or UHSC. Fig.4.12 shows the axial stress vs. strain curves of the specimens with different hollow ratios. From this figure, it can be seen that the hollow ratio significantly affects the ultimate axial stress of the columns and the absolute strain value at ultimate axial stress. Fig.4.13 and Fig.4.14 present the axial stress vs. strain curves of the specimens with different wall thickness and yield stress of the outer tube. It can be seen from Fig.4.13 and Fig.4.14 that with the increase of the wall thickness and yield stress of the outer tube, the ultimate axial stress of the specimens and the absolute strain value at ultimate axial stress as well as the ductility are improved. This is mainly attributed to the increase of the steel ratio and the enhancement of the confinement effect.

4.2.5.4. Load-carrying capacities

The cross-sectional resistances of the tested CFDST columns are shown in Table 4.1 and illustrated against the experimental parameters in Fig.4.15. In Table 1 and Fig.4.15, $N_{u,e}$ denotes the cross-sectional resistances of the tested CFDST columns. From Fig.4.15, it can be seen that as the concrete strength increases, the cross-sectional resistances of the columns increase linearly. Along with the increase of the wall thickness and yield stress of the outer tube, the cross-sectional resistances of the columns increase, whereas they decrease with the increase of the hollow ratio. Overall, the geometrical dimensions and material strengths investigated exhibit a significant effect on the load-carrying capacities of the studied CFDST columns.

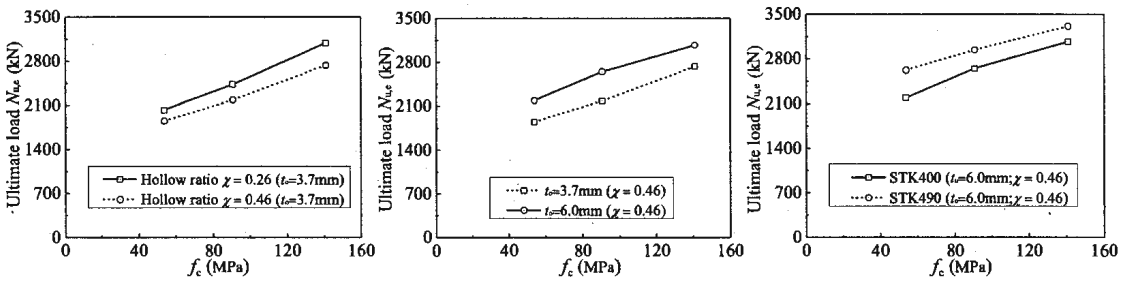

(a) (b) (c)

Fig.4.15 Effects of the tested parameters on load-carrying capacities

4.2.5.5. Strength index (*SI*)

A strength index (*SI*) is presented to quantitatively evaluate the composite effects between the steel tubes and concrete infill on the cross-sectional resistances of the CFDST columns, and it can be determined by:

$$SI = \frac{N_{u,e}}{N_{u,c}} \tag{4.1}$$

in which $N_{u,e}$ is the measured ultimate axial strength from the experimental tests, as shown in Table 4.1; $N_{u,c}$ is the calculated ultimate axial strength and can be determined by Eq. (2), where the plastic resistance of internal steel tube is taken as an individual term and incorporated in the equation.

$$N_{u,c} = A_{so} f_{syo} + A_c f_c + A_{si} f_{syi} \tag{4.2}$$

where A_{so} and A_{si} are the cross-sectional areas of the outer and inner tubes, respectively; f_{syo} and f_{syi} are the yield strengths of the outer and inner tubes, respectively; A_c and f_c stand for the cross-sectional area and cylinder strength of concrete infill, respectively.

The strength indexes (*SI*) for all specimens are listed in Table 4.1, and their average values are illustrated against the experimental parameters in Fig.4.16. From Fig.4.16, it can be seen that the value of *SI* decreases with the increase in the concrete strength. This is mainly due to the fact that the utilization rate of concrete infilled is reduced with the increase of the concrete strength owing to the weak confinement effect induced from the brittleness of HSC. Additionally, it can be noted that the value of *SI* decreases as the hollow ratio increases (see Fig.4.16(a)), whereas it increases as the wall thickness and yield stress of the outer tube increase (see Figs.4.16(b) and (c)).

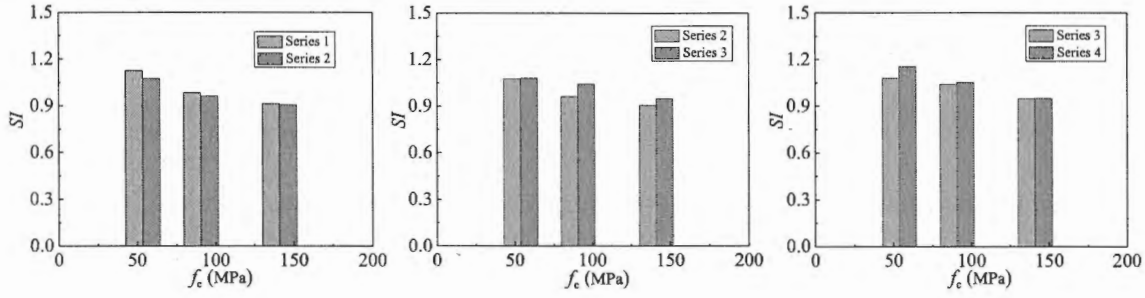

(a) (b) (c)

Fig.4.16 Effects of the investigated parameters on strength index (*SI*)

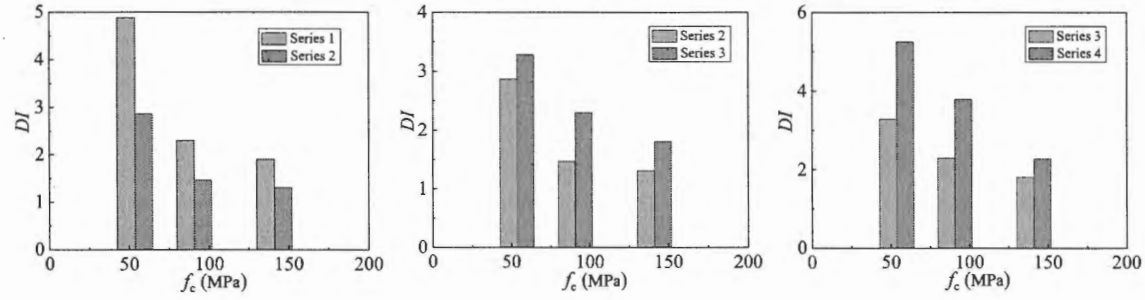

(a) (b) (c)

Fig.4.17 Effects of the investigated parameters on ductility (*DI*)

4.2.5.6. Ductility index (*DI*)

A ductility index (*DI*) can be presented to quantitatively evaluate the effects of the investigated parameters on the post-peak behaviour of the CFDST columns. *DI* is defined as below [10]:

$$DI = \frac{\bar{\varepsilon}_{85\%}}{\bar{\varepsilon}_u} \tag{4.3}$$

in which $\bar{\varepsilon}_{85\%}$ represents the axial strain when the axial load is reduced to 85% of the ultimate load, $\bar{\varepsilon}_u$ denotes the axial strain at the ultimate load.

The ductility indexes (*DI*) for all specimens are listed in Table 4.1, and their average values are illustrated against the experimental parameters in Fig.4.17. From this figure, one can be found that the value of *DI* decreases with the increase in the concrete strength. This demonstrates that the tested CFDST columns tend to the brittleness failure with the increase in the concrete strength. In addition, it can be observed that the value of *DI* decreases as the hollow ratio increases (see Fig.4.17(a)), whereas it increases as the wall thickness and yield stress of the outer tube increase (see Figs.4.17(b) and 4.17(c)).

4.3. Numerical modelling

The FE models based on the computer-aided engineering software ABAQUS [29] are developed and validated by comparing with the axial load vs. displacement curves, ultimate strengths and failure modes from the experimental results. Using the verified FE models, the interaction of the steel tubes and concrete as well as the load distribution on components are analysed, and the parametric study is performed to further ascertain the effects of column variables on the compressive behaviour of the studied CFDST columns.

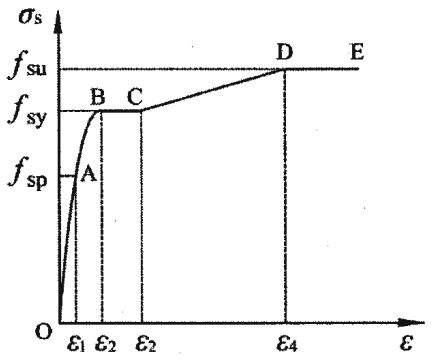

Fig.4.18 Stress (σ) -strain (ε) relationship for steel

4.3.1. Material modelling

4.3.1.1. Carbon steel

An idealized multi-linear elastic-plastic stress-strain relationship suggested by Han et al. [30] as depicted in Fig.4.18 is adopted herein to simulate steel. This model is widely utilized by many researchers, such as Li et al. [11], Huang et al. [31] and Wang et al. [32]. The stress-strain relationship of carbon steel suggested by Han et al. [30] is expressed by:

$$\sigma_s = \begin{cases} E_s\varepsilon & \varepsilon \le \varepsilon_1 \\ -A\varepsilon^2 + B\varepsilon + C & \varepsilon_1 \le \varepsilon \le \varepsilon_2 \\ f_{sy} & \varepsilon_2 \le \varepsilon \le \varepsilon_3 \\ f_{sy}\left[1 + 0.6\dfrac{\varepsilon - \varepsilon_3}{\varepsilon_4 - \varepsilon_3}\right] & \varepsilon_3 \le \varepsilon \le \varepsilon_4 \\ 1.6f_{sy} & \varepsilon \ge \varepsilon_4 \end{cases} \tag{4.4}$$

where E_s and f_{sy} denote the elastic modulus and yield stress of the steel, and E_s is taken as 2.0×10^5 MPa; $A = 0.2f_{sy}/(\varepsilon_2 - \varepsilon_1)^2$, $B = 0.2A\varepsilon_2$, $C = 0.8f_{sy} + A\varepsilon_1^2 - B\varepsilon_1$, $\varepsilon_1 = 0.8f_{sy}/E_s$, $\varepsilon_2 = 1.5\varepsilon_1$, $\varepsilon_3 = 10\varepsilon_2$, $\varepsilon_4 = 100\varepsilon_2$.

4.3.1.2. Concrete

The concrete material model developed by Han et al. [30] performed well in modeling the behavior of CFST members under various conditions, e.g., axial compression, torsion, bending and shearing. Li et al. [11], Huang et al. [31] and Wang et al. [32] suggested that the passive confinement of concrete in CFST and CFDST columns shows insignificant difference, and Han's model [30] can be used to model the behaviour of concrete in CFDST columns. In this paper, the concrete material model provided by Han et al. [30] is tentatively adopted and expressed by:

$$\sigma_c = \begin{cases} 2x - x^2 & x \le 1 \\ \dfrac{x}{\beta_0 (x-1)^\eta + x} & x > 1 \end{cases} \tag{4.5}$$

where $x = \varepsilon / \varepsilon_0$, $y = f / f_c$, ε stands for the axial strain of concrete at axial stress f; f_c symbolizes the standard concrete cylinder strength; ε_0 is the axial strain at the concrete strength f_c; η and β_0 represent the parameters related to the section type. For circular section, η is taken as 2, and β_0 is expressed as below:

$$\beta_0 = 0.5\left(2.36 \times 10^{-5}\right)^{\left[0.25 + (\xi - 0.5)^7\right]} \left(f_c\right)^{0.5} \ge 0.12 \tag{4.6}$$

where ξ represents the nominal confinement factor.

In addition, the concrete damage plasticity model (CDPM) is employed in this paper, and the details of the CDPM can be found in Refs. [30].

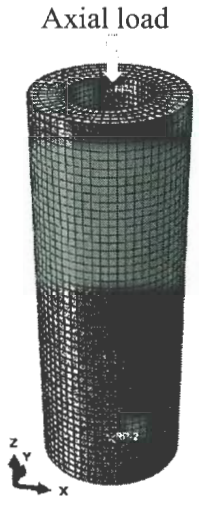

Fig.4.19 Mesh of FE model for CFDST column

4.3.2. Element, boundary condition and method of loading

The mesh of typical FE model for circular CFDST short columns is shown in Fig.4.19. In Fig.4.19, the 8-node linear brick elements with reduced integration (C3D8R) and shell elements (S4R) are adopted to model the sandwiched concrete and steel tube [31-33]. The element size for a circular section is taken as $D/20$ based on mesh convergence studies [32]. Two reference points (RPs) are

designated at two ends of the column, and the concrete and steel tube surfaces at both ends of the column are coupled to the RPs. The boundary conditions are applied to both RPs, where all degrees of freedom of RP-1 and RP-2 are restrained except for z-axis displacement at RP-1. A uniform displacement instead of directly loading is statically applied in z-axis of RP-1

4.3.3. Contact modelling

In order to model the contact behaviors between the steel tubes and concrete, a surface-to-surface contact is employed. The inside surface of outer steel tube and the outside surface of inner steel tube are specified as the master surfaces, and the concrete surfaces in contact with the steel tubes are naturally defined as slave surfaces. The Coulomb friction model incorporating a friction coefficient of 0.6 and hard-contact relation are employed in the tangent and normal directions, respectively [11-12].

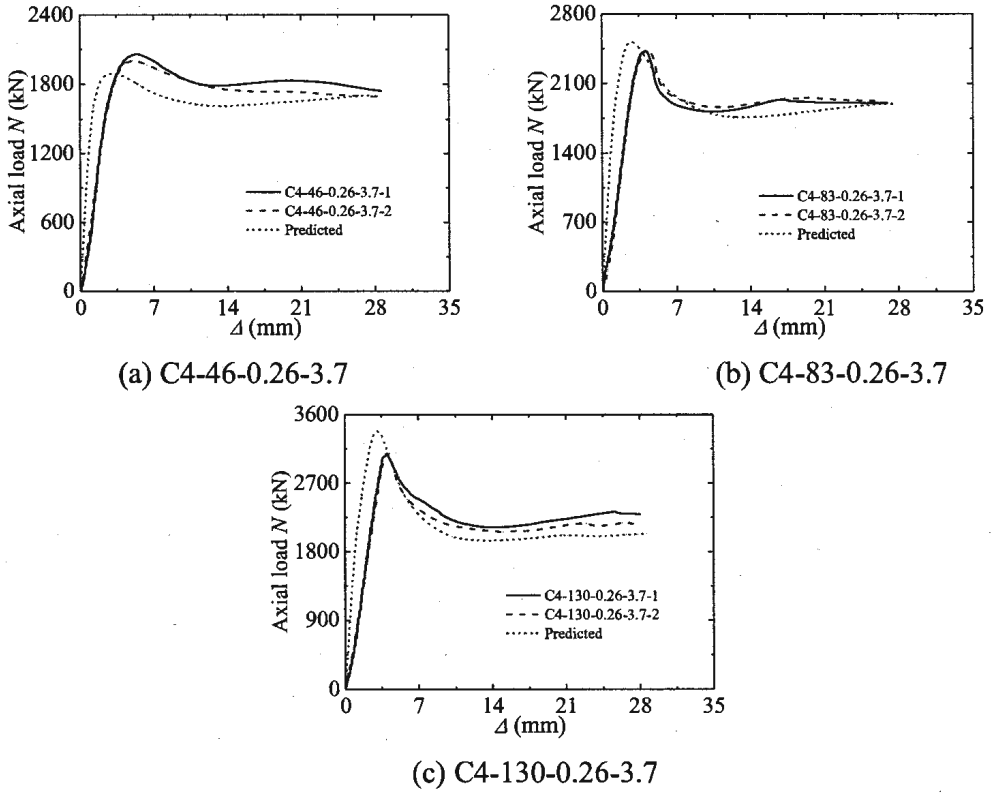

(a) C4-46-0.26-3.7

(b) C4-83-0.26-3.7

(c) C4-130-0.26-3.7

Fig.4.20 Comparisons of the predicted and measured axial load N-shortening (ε) curves

4.3.4. Verification of FE modelling

The established FE models are verified against comparing with the test results in terms of axial load vs. shortening curves, ultimate strengths and failure modes. The comparisons of axial load vs. shortening curves between the FE modelling and experiments are depicted in Fig.4.20. From Fig.4.20, it can be found that the FE models can almost replicate axial load-deformation histories of the tested specimens. A slight discrepancy is found in the prediction of the initial stiffness and ultimate strengths. This discrepancy may have been resulted from the interaction between steel and concrete simulated in ABAQUS which is not completely consistent with the actual test conditions. Moreover, the real f_c values of the concrete infill may also differ from those obtained from the cylindrical material tests due to differences in the curing methods used in both specimens. Two possible reasons can be used

to explain that the predicted stiffness of the numerical model is higher than the experimental one. Firstly, it is difficult for the end constraint conditions simulated in FE models to be consistent with the test conditions. Due to the influence of gravity and other natural conditions, the density and strength of concrete at both ends of the specimens may be lower than that in the middle, which leads to a relatively weak composite effect between the steel tube and concrete at two ends of the specimens. However, the uniform density and strength of concrete were used in the FE models. This may cause the predicted stiffness to be higher than the test stiffness. Secondly, with the improvement of concrete strength, due to the brittleness of HSC, the utilization efficiency of concrete strength may be reduced, which makes the effective concrete strength filled in the column specimens lower than that obtained from the concrete cylindrical material tests. However, the FE models employ the concrete strength obtained from the concrete cylindrical material tests, which will make the predicted stiffness higher than the test stiffness.

Moreover, a comparison of ultimate strengths between the FE modelling and experimental tests is listed in Table 4.1. The mean value of $N_{FE}/N_{u,exp.}$ is 1.044, with a coefficient of variation (CoV) of 0.061. This indicates that the FE models perform well in predicting the ultimate strengths of the tested CFDST columns. In addition, comparisons of the failure modes between the FE modelling and experiments are shown in Fig.4.8. From Fig.4.8, it can be observed that good agreements are achieved between numerical and test failure modes. In general, the developed FE models can effectively predict the axial compression response of the studied CFDST columns with a reasonable accuracy, which provides a basis for further numerical study.

4.4. Mechanism analysis and parametric study

4.4.1. Mechanism analysis

In this section, comparisons between the mechanical behavior of the CFDST columns with NSC and HSC are made by utilizing the verified FE model. The column parameters of the specimens for mechanism analysis are: D_o = 300 mm, t_o = 6 mm, D_i = 145 mm, t_i = 6 mm, $f_{syo} = f_{syi}$ =275 MPa, f_c = 40 MPa (NSC), f_c = 80 MPa (HSC), χ = 0.5.

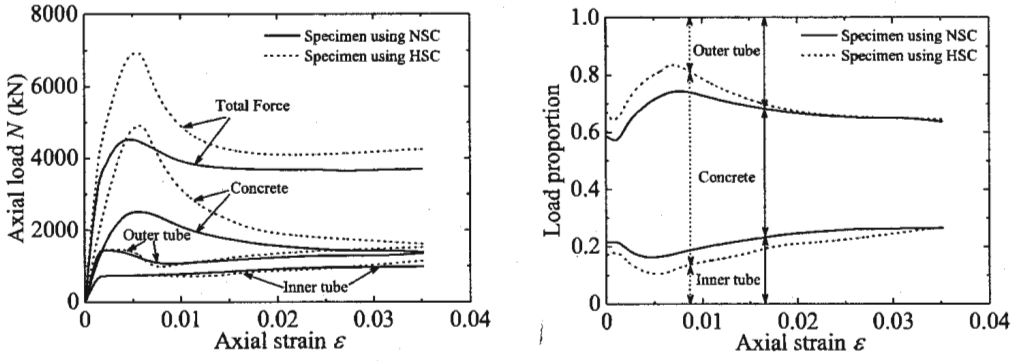

Fig.4.21 Load distribution in different components of the specimens with NSC and HSC

The calculated axial load (N) vs. axial strain (ε) curves of the specimens with NSC and HSC and the different components are depicted in Fig.4.21(a). From this figure, it can be seen that with the increase of concrete strength, the initial stiffness, axial strengths and post-peak residual strengths of the specimens and the sandwiched concrete are increased. However, the axial loads carried by the outer and inner steel tubes are almost the same. This shows that concrete grade plays an important

role in improving the load-carrying capacity of the columns. Besides, the load-carrying proportion vs. axial strain relations of different components are shown in Fig.4.21(b). From Fig.4.21(b), it can be found that at the beginning of loading, the load proportions for the concrete, outer and inner steel tubes are approximately 36%, 42% and 22% for the specimen with NSC, and 50%, 33% and 17% for the specimen with HSC, respectively. As the axial deformation increases, the load proportion of the sandwiched concrete gradually decreases. This is mainly because the elastic modulus of concrete decreases with the increase of axial deformation in the elastic stage, and the load-carrying capacity of concrete is proportional to the elastic modulus of concrete. As the axial compression continues, the outer and inner steel tubes yield and could not provide more strength. Due to the confinement effect, the concrete strength continues to increase, resulting in an increase in the load proportion. Finally, as the load-carrying proportion of different components of the specimen with HSC is almost the same as that of the specimen with NSC.

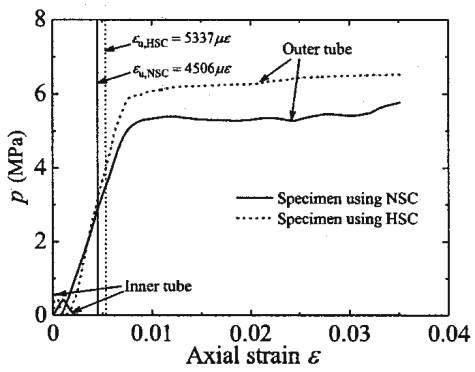

Fig.4.22 Contact stress between the steel tubes and concrete

Fig.4.22 shows that the contact stress (p) vs. axial strain (ε) relations between the steel tubes and sandwiched concrete of the specimens with NSC and HSC. In Fig.4.22, $\varepsilon_{u,NSC}$ and $\varepsilon_{u,NSC}$ stand for the ultimate strains when the specimens reach the ultimate loads, respectively. It can be seen from this figure that in the initial stage of loading, because the Poisson's ratio of concrete is less than that of steel tube, the lateral confinement stress of the outer steel tube is almost zero, and the inner steel tube yields a smaller lateral confinement stress. As the axial deformation increases, the equivalent Poisson's ratio of concrete becomes larger than that of the steel tube. As a result, the outer steel tube begins to provide the lateral confinement stress to the sandwiched concrete, while the lateral confinement stress of the inner steel tube becomes zero. It can be observed that the lateral confinement stress is delayed with the increase of the concrete strength, which is mainly because the HSC has less lateral expansion at this stage. As the axial compression continues, the lateral confinement stress provided by the outer steel tube of the specimen with HSC is stronger than that of the specimen with NSC after 3000 $\mu\varepsilon$. Besides, it can be found that the lateral confinement stress provided by the outer steel tube of the specimen with HSC is slightly higher than that of the specimen with NSC at ultimate load. This is mainly because the lateral expansion of the HSC is larger than that of the NSC at ultimate load.

4.4.2. Parametric study

Utilizing the verified FE model, the effects of the key geometric parameters and material properties on the compressive behaviour of the studied CFDST columns are investigated. In this study,

Table 4.5. The details of parametric design

Parameters	Specimens	$D_o \times t_o$ (mm × mm)	D_o/t_o	$D_i \times t_i$ (mm × mm)	D_i/t_i	f_{syo} (MPa)	f_{syi} (MPa)	f_c (MPa)	χ	$N_{u,FE}$ (kN)	DI
Compressive strength of concrete	S1	300 × 6	50	145 × 6	24	275	275	50	0.5	4907	2.21
	S2	300 × 6	50	145 × 6	24	275	275	70	0.5	5867	1.62
	S3	300 × 6	50	145 × 6	24	275	275	90	0.5	6936	1.42
	S4	300 × 6	50	145 × 6	24	275	275	110	0.5	7884	1.25
	S5	300 × 6	50	145 × 6	24	275	275	130	0.5	8715	1.11
Yield stress of outer steel tube	S6	300 × 6	50	145 × 6	24	275	275	80	0.5	6449	1.43
	S7	300 × 6	50	145 × 6	24	355	275	80	0.5	6985	1.56
	S8	300 × 6	50	145 × 6	24	460	275	80	0.5	7690	1.66
	S9	500 × 10	50	240 × 8	30	275	275	80	0.5	17412	1.40
	S10	500 × 10	50	240 × 8	30	355	275	80	0.5	18999	1.52
	S11	500 × 10	50	240 × 8	30	460	275	80	0.5	20917	1.63
Yield stress of inner steel tube	S12	300 × 6	50	145 × 6	24	275	355	70	0.5	5999	1.60
	S13	300 × 6	50	145 × 6	24	275	460	70	0.5	6171	1.63
Hollow ratio	S14	300 × 6	50	28 × 4	7	275	275	70	0.1	6449	1.73
	S15	300 × 6	50	86 × 4	22	275	275	70	0.3	6346	1.81
	S16	300 × 6	50	145 × 4	36	275	275	70	0.5	5867	1.90
	S17	300 × 6	50	201 × 4	50	275	275	70	0.7	4673	2.11
Diameter-to-thickness ratio of outer steel tube	S18	300 × 10	30	145 × 6	24	275	275	60	0.5	6233	2.19
	S19	300 × 6	50	145 × 6	24	275	275	60	0.5	5383	2.01
	S20	300 × 4.3	70	145 × 6	24	275	275	60	0.5	4981	1.82
Diameter-to-thickness ratio of inner steel tube	S21	300 × 6	50	145 × 9.7	15	275	275	70	0.5	6257	1.61
	S22	300 × 6	50	145 × 5.8	25	275	275	70	0.5	6006	1.60
	S23	300 × 6	50	145 × 4.1	35	275	275	70	0.5	5819	1.61

the variables investigated include the yield stresses and diameter-to-thickness ratios of the outer and inner steel tubes, concrete strength, and hollow ratio. The details of the parametric design are listed in Table 4.5.

4.4.2.1. Effect of concrete strength

S1-S5 listed in Table 4.5 were employed here to investigate the effect of concrete strength on the axial load N vs. strain ε curves, ultimate strengths, and ductility performance of the CFDST columns. The considered concrete strengths are 50, 70, 90, 110, and 130 MPa. Fig.4.23(a) shows the N - ε curves of the CFDST columns, while their ultimate strengths are given in Table 4.5. The ductility indices are given in both Fig.4.23(b) and Table 4.5. From Fig.4.23, it can be seen that the initial stiffness and ultimate strengths of the columns are increased with the increase of concrete strength, while their ductility is reduced. When the concrete strength increases from 50 MPa to 130 MPa, the initial stiffness of the columns increases by 18.5%, 36.6%, 45.7% and 64.1%, respectively. From Table 4.5, it can be seen that with the increase of the concrete strength from 50 MPa to 130 MPa, the ultimate strengths of the columns increase by 19.6%, 41.3%, 60.7%, and 77.6%, respectively. However, the ductility of the columns reduces by 26.7%, 35.7%, 43.4%, and 49.8%, respectively, as the concrete strength increases from 50 MPa to 130 MPa. This indicates that increasing the concrete strength can improve the initial stiffness and ultimate strength of the CFDST columns, but it reduces columns' ductility

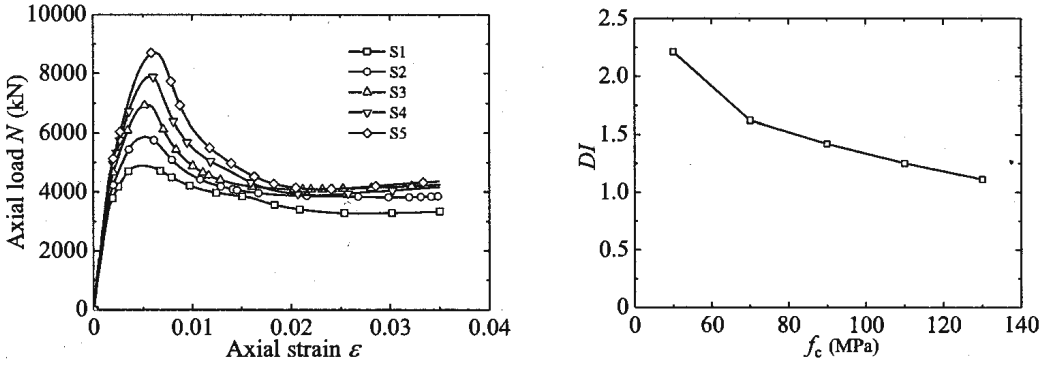

(a) (b)

Fig.4.23 Effect of compressive strength of concrete

4.4.2.2. Effect of yield stress of outer steel tube

S6-S8 and S9-11 with two different sectional dimensions listed Table 4.5 were used to investigate the effect of the yield stress of outer steel tube on the axial load N vs. strain ε curves, ultimate strengths, and ductility performance of the CFDST columns. The considered yield stresses are 275, 355, and 460 MPa. Figs.4.24(a) and 4.24(b) show the N - ε curves of CFDST columns, while their ultimate strengths are shown in Table 4.5. The ductility indices are given in both Fig.4.24(c) and Table 4.5. From Fig.4.24, it can be seen that the initial stiffness, ultimate strengths, and ductility of the columns are increased with the increase of the yield stress of the outer steel tube. When the yield stress of the outer steel tube increases from 275 to 460 MPa, the initial stiffness of the columns increases by 17.9% and 32.3% for S6-S8 as well as 18.3% and 31.2% for S9-S11, respectively. From Table 4.5, it can be seen that with the increase of the yield stress of the outer steel tube from 275 to 460 MPa, the ultimate strengths of the columns increase by 8.3% and 19.2% for S6-S8 as well as 9.1% and 20.1% for S9-S11, respectively. Besides, the ductility of the columns increases by 9.0% and 16.1% for S6-S8 as

well as 8.6% and 16.4% for S9-S11, respectively, as the yield stress of the outer steel tube increases from 275 to 460 MPa. This indicates that increasing the yield stress of the outer steel tube can considerably improve the ultimate loads and ductility of the CFDST columns.

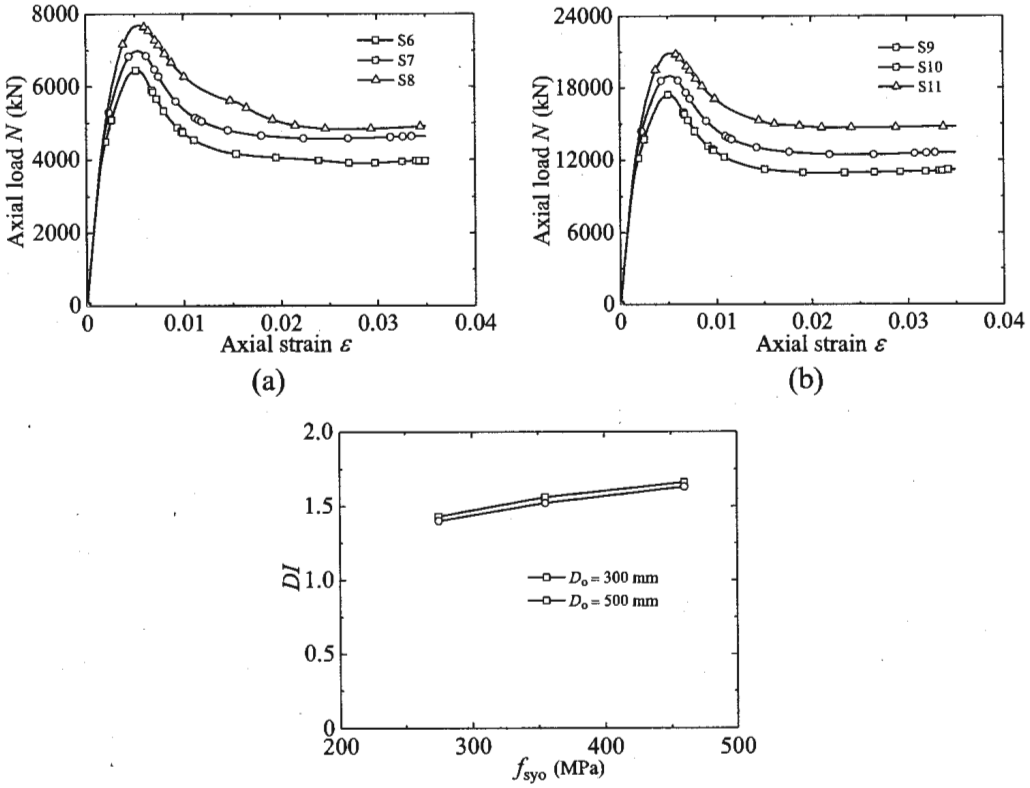

(a) (b) (c)

Fig.4.24 Effect of yield stress of outer steel tube

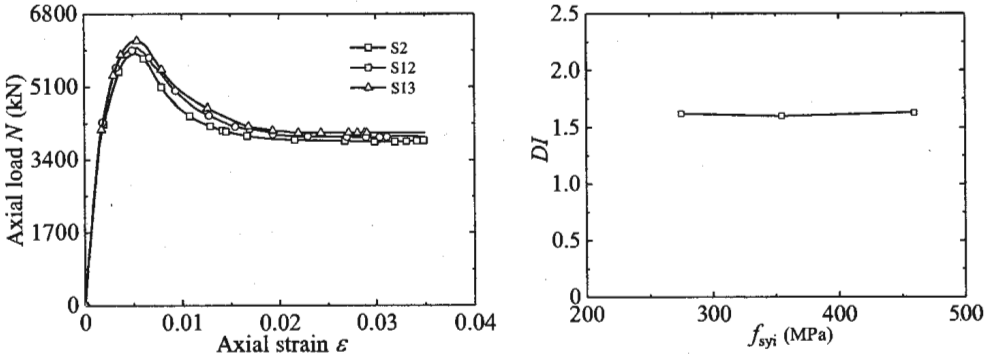

(a) (b)

Fig.4.25 Effect of yield stress of inner steel tube

4.4.2.3. Effect of yield stress of inner steel tube

S2, S12-S13 listed Table 4.5 were used to investigate the effect of the yield stress of the inner steel tube on the axial load N vs. strain ε curves, ultimate strengths, and ductility performance of the CFDST columns. The considered yield stresses are 275, 355, and 460 MPa. Fig.4.25(a) shows the N - ε curves of the CFDST columns, while their ultimate strengths are shown in Table 4.5. The ductility indices are given in both Fig.4.25(b) and Table 4.5. From Fig.4.25 and Table 4.5, it can be seen that

the initial stiffness, ultimate strengths, and ductility of the CFDST columns are almost the same. This indicates that the yield stress of the inner steel tube yields insignificant effect on the initial stiffness, ultimate strengths, and ductility of the CFDST columns. This is mainly because the inner steel tube makes less strength contribution than other components and provides less lateral confinement to the sandwiched concrete.

4.4.2.4. Effect of hollow ratio

S14-S17 listed Table 4.5 were employed to ascertain the effect of the hollow ratio on the axial load N vs. strain ε curves, ultimate strengths, and ductility performance of the CFDST columns. The considered hollow ratios are 0.1, 0.3, 0.5, and 0.7. Fig.4.26(a) depicts the N - ε relations of the CFDST columns, while their ultimate strengths are listed in Table 4.5. The ductility indices are shown in both Fig.4.26(b) and Table 4.5. From Fig.4.26, it can be seen that with the increase of the hollow ratio, the initial stiffness and ultimate strengths of the columns are decreased while their ductility is increased. This is mainly because the increase of the hollow ratio reduces the cross-sectional area of concrete, which plays an important role in bearing the axial load, and increases the steel ratio. When the hollow ratio increases from 0.1 to 0.7, the ultimate strengths of the columns decrease by 1.6%, 9.0%, and 27.5%, respectively. However, the ductility of the columns increases by 4.6%, 9.8%, and 22.0%, respectively, as the hollow ratio increases from 0.1 to 0.7.

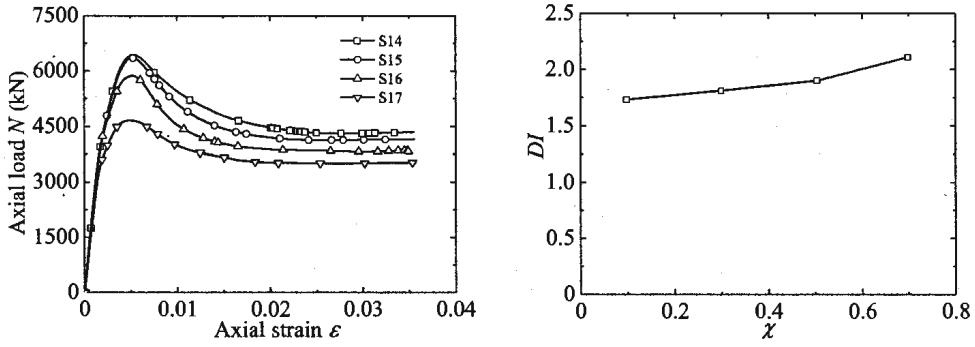

Fig.4.26 Effect of hollow ratio

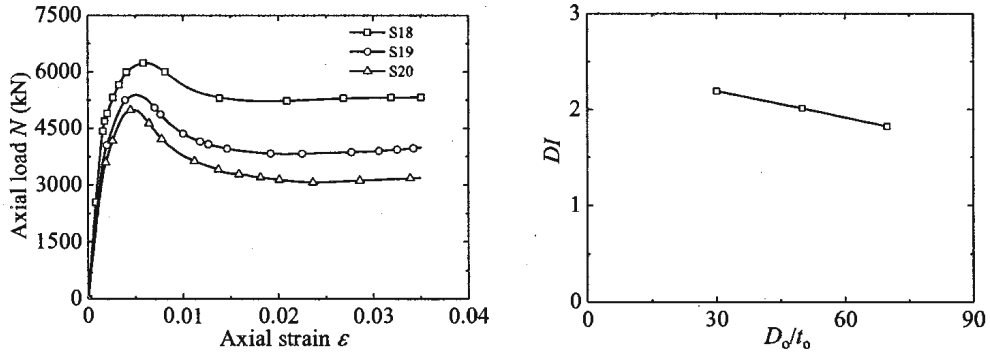

Fig.4.27 Effect of D_o/t_o ratio

4.4.2.5. Effect of outer tube diameter-to-wall thickness ratio (D_o/t_o)

S18-S20 listed Table 4.5 were employed to discuss the effect of the D_o/t_o ratio on the axial load N vs. strain ε curves, ultimate strengths, and ductility performance of the CFDST columns. Herein,

the D_o/t_o ratio is increased by reducing the wall thickness of the outer steel tube while keeping its diameter constant. The considered D_o/t_o ratios are 30, 50, and 70. Fig.4.27(a) gives the N - ε relations of the CFDST columns, while their ultimate strengths are listed in Table 4.5. The ductility indices are shown in both Fig.4.27(b) and Table 4.5. From Fig.4.27, it can be found that with the increase of the D_o/t_o ratio, the initial stiffness, ultimate strengths, and ductility of the columns are decreased. When the D_o/t_o ratio increases from 30 to 70, the initial stiffness of the columns decreases by 18.9% and 27.6%, respectively, and their ultimate strengths reduce by 13.6% and 20.1%, respectively. Besides, the ductility of the columns decreases by 8.2% and 16.9%, respectively, as the D_o/t_o ratio increases from 30 to 70. This is mainly attributed to the fact that the reduction of the wall thickness of the outer steel tube diminishes its lateral confinement effect to the sandwiched concrete, and reduces the steel ratio.

4.4.2.6. Effect of inner tube diameter-to-wall thickness ratio (D_i/t_i)

S21-S23 listed Table 4.5 were used to analyse the effect of the D_i/t_i ratio on the axial load N vs. strain ε curves, ultimate strengths, and ductility performance of the CFDST columns. Herein, the D_i/t_i ratio is increased by reducing the wall thickness of the inner steel tube while keeping its diameter constant. The considered D_i/t_i ratios are 15, 25, and 35. Fig.4.28(a) gives the N - ε relations of CFDST columns, while their ultimate strengths are listed in Table 4.5. The ductility indices are shown in both Fig.4.28(b) and Table 4.5. From Fig.4.28, it can be seen that the initial stiffness, ultimate strengths, and ductility of the CFDST columns are almost the same. This shows that the D_i/t_i ratio yields insignificant effect on the initial stiffness, ultimate strengths, and ductility of the CFDST columns. This finding is basically consistent with the effect of the yield stress of the inner steel tube, which is attributed to the fact that the inner steel tube makes less strength contribution than other components and provides less lateral confinement to the sandwiched concrete.

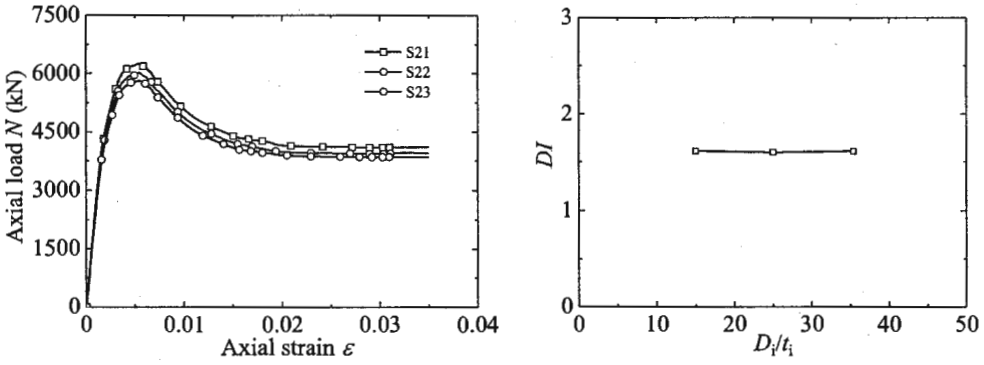

Fig. 28 Effect of D_i/t_i ratio

4.5. Proposal of strength prediction model

4.5.1. Investigation of the existing design codes and empirical models

In this section, the prediction models specified in the existing design codes and the empirical models given by the previous researchers are investigated based on the conducted and collected experimental test data. The design equations in the existing design codes and empirical models are given in Table 6. The existing design codes, i.e., the European Code EN 1994-1-1 (EC4) [24] and the American Specification AISC 360-16 [25], are employed here to determine the cross-sectional resistances of the CFDST columns. As Wang et al. [12] and Ekmekyapar and Hasan [22] suggested,

the term relating to the reinforcing bars is replaced by the inner steel tube, which is treated as an independent term incorporated in the resistance equation. It should be noted that limitations on the sectional slenderness and material strengths are specified in codes EC4 [24] and AISC 360 [25]; see

Table 4.6. Design equations in the existing empirical models and design codes

Design codes	Design equations
AISC 360-16 [25]	$N_{u,AISC}=\begin{cases} N_p & \text{(Compact)} \\ N_p-\dfrac{N_p-N_y}{(\lambda_r-\lambda_p)^2}(\lambda-\lambda_p)^2+A_{si}f_{syi} & \text{(Noncompact)} \\ A_{so}f_{cr}+0.7f_cA_c+A_{si}f_{syi} & \text{(Slender)} \end{cases}$ $N_p=A_{so}f_{syo}+0.95A_cf_c+A_{si}f_{syi} \qquad N_y=A_{so}f_{syo}+0.7A_cf_c+A_{si}f_{syi}$ $f_{cr}=\dfrac{0.72f_{syo}}{\left[\left(\dfrac{D_o}{t_o}\right)\dfrac{f_{syo}}{E_o}\right]^{0.2}}$
EC 4 [24]	$N_{u,EC4}=A_cf_c\left(1+\eta_c\dfrac{t_o}{D_o}\dfrac{f_{syo}}{f_c}\right)+\eta_aA_{so}f_{syo}+A_{si}f_{syi}$ $\eta_c=4.9-18.5\bar{\lambda}+17\bar{\lambda}^2\geq 0 \qquad \eta_a=0.25(3+2\bar{\lambda})\leq 1.0$ $\bar{\lambda}=\dfrac{N_{plR}}{N_{cr}} \qquad A_{eff}=A\left(\dfrac{90}{D/t}\dfrac{235}{f_{sy}}\right)^{0.5}$
Empirical models	Design equations
Han et al. [34]	$N_{u,Han}=N_{osc,u}+N_{i,u}$ $N_{osc,u}=f_{scy}A_{sco} \qquad N_{i,u}=f_{syi}A_{si}$ $A_{sco}=A_{so}+A_c \qquad f_{scy}=C_1\chi^2f_{syo}+C_2(1.14+1.02\xi)f_{ck}$
Uenaka et al. [35]	$N_{u,Uenaka}=\left(2.86-2.59\dfrac{D_i}{D_o}\right)f_{syo}A_{so}+f_cA_c+f_{syi}A_{si}$ with $0.2<\dfrac{D_i}{D_o}\leq 0.7$
Hassanein et al. [33]	$N_u=\gamma_{so}f_{syo}A_{so}+f'_{cc}A_c+\gamma_{si}f_{syi}A_{si}$ $f'_{cc}=\gamma_cf_c+4.1f'_{rp}$ $f'_{rp}=\begin{cases} 0.7(\upsilon_e-\upsilon_s)\dfrac{2t_o}{D_o-2t_o}f_{syo} & \text{for } \dfrac{D_o}{t_o}\leq 47 \\ \left(0.006241-0.0000357\dfrac{D_o}{t_o}\right)f_{syo} & \text{for } 47<\dfrac{D_o}{t_o}\leq 150 \end{cases}$
Liang [36]	$f'_{rp}=8.525-0.166\left(\dfrac{D_o}{t_o}\right)-0.00897\left(\dfrac{D_i}{t_i}\right)+0.00125\left(\dfrac{D_o}{t_o}\right)^2$ $+0.00246\left(\dfrac{D_o}{t_o}\right)\left(\dfrac{D_i}{t_i}\right)-0.0055\left(\dfrac{D_i}{t_i}\right)^2\geq 0$

Table 4.7. Comparisons between the conducted test results and design models

Specimens	$N_{u,e}$ (kN)	Ref. [25]		Ref. [24]		Ref. [34]		Ref. [35]		Ref. [33]		Ref. [36]		Proposed model	
		$N_{u,c}$	$N_{u,c}/N_{u,e}$	$N_{u,c}$	$N_{u,c}/N_{u,e}$	$N_{u,c}$	$N_{u,c}/N_{u,e}$	$N_{u,c}$	$N_{u,c}/N_{u,e}$	$N_{u,c}$	$N_{u,c}/N_{u,e}$	$N_{u,c}$	$N_{u,c}/N_{u,e}$	$N_{u,c}$	$N_{u,c}/N_{u,e}$
C4-46-0.26-3.7-1	2060	1738	0.84	2164	1.05	1809	0.88	2339	1.14	2110	1.02	2113	1.03	2126	1.03
C4-46-0.26-3.7-2	2003	1735	0.87	2160	1.08	1806	0.90	2336	1.17	2108	1.05	2109	1.05	2122	1.06
C4-83-0.26-3.7-1	2423	2077	0.86	2508	1.04	2507	1.03	2971	1.23	2751	1.14	2780	1.15	2482	1.02
C4-83-0.26-3.7-2	2446	2081	0.85	2514	1.03	2512	1.03	2978	1.22	2757	1.13	2784	1.14	2487	1.02
C4-130-0.26-3.7-1	3068	2763	0.90	3210	1.05	3452	1.13	3543	1.15	3347	1.09	3682	1.20	3204	1.04
C4-130-0.26-3.7-2	3110	2767	0.89	3214	1.03	3457	1.11	3547	1.14	3351	1.08	3687	1.19	3208	1.03
C4-46-0.46-3.7-1	1831	1669	0.91	2001	1.09	1727	0.94	2163	1.18	1976	1.08	1874	1.02	1941	1.06
C4-46-0.46-3.7-2	1876	1667	0.89	1999	1.07	1726	0.92	2161	1.15	1974	1.05	1870	1.00	1939	1.03
C4-83-0.46-3.7-1	2174	1949	0.90	2287	1.05	2305	1.06	2686	1.24	2505	1.15	2427	1.12	2235	1.03
C4-83-0.46-3.7-2	2202	1952	0.89	2290	1.04	2308	1.05	2690	1.22	2508	1.14	2427	1.10	2238	1.02
C4-130-0.46-3.7-1	2732	2512	0.92	2864	1.05	3080	1.13	3154	1.15	2992	1.10	3164	1.16	2826	1.03
C4-130-0.46-3.7-2	2736	2513	0.92	2867	1.05	3082	1.13	3156	1.15	2992	1.09	3163	1.16	2829	1.03
C4-46-0.46-6.0-1	2183	1980	0.91	2437	1.12	2106	0.96	2639	1.21	2403	1.10	2228	1.02	2360	1.08
C4-46-0.46-6.0-2	2203	1981	0.90	2436	1.11	2107	0.96	2638	1.20	2403	1.09	2230	1.01	2359	1.07
C4-83-0.46-6.0-1	2666	2242	0.84	2705	1.01	2678	1.00	3078	1.15	2853	1.07	2744	1.03	2637	0.99
C4-83-0.46-6.0-2	2631	2239	0.85	2701	1.03	2674	1.02	3074	1.17	2849	1.08	2741	1.04	2633	1.00
C4-130-0.46-6.0-1	3110	2771	0.89	3245	1.04	3450	1.11	3371	1.08	3179	1.02	3440	1.11	3193	1.03
C4-130-0.46-6.0-2	3032	2763	0.91	3235	1.07	3440	1.13	3361	1.11	3170	1.05	3425	1.13	3183	1.05
C9-46-0.46-6.0-1	2645	2220	0.84	2763	1.04	2344	0.89	2990	1.13	2699	1.02	2478	0.94	2679	1.01
C9-46-0.46-6.0-2	2601	2218	0.85	2761	1.06	2343	0.90	2988	1.15	2697	1.04	2476	0.95	2677	1.03
C9-83-0.46-6.0-1	2971	2487	0.84	3036	1.02	2921	0.98	3531	1.19	3239	1.09	3000	1.01	2962	1.00
C9-83-0.46-6.0-2	2911	2488	0.85	3038	1.04	2923	1.00	3532	1.21	3240	1.11	2998	1.03	2964	1.02
C9-130-0.46-6.0-1	3322	3012	0.91	3567	1.07	3688	1.11	3929	1.18	3668	1.10	3692	1.11	3513	1.06
C9-130-0.46-6.0-2	3304	3016	0.91	3573	1.08	3693	1.12	3927	1.19	3666	1.11	3693	1.12	3518	1.06
Mean			0.88		1.05		1.02		1.17		1.08		1.08		1.03
SD			0.03		0.03		0.09		0.04		0.04		0.07		0.02
CoV			0.03		0.02		0.09		0.03		0.03		0.07		0.02

Table 4.8. Details of 126 published experimental data

Refs.	No.	Specimens	$D_o \times t_o$ (mm)	D_o/t_o	f_{syo} (MPa)	$D_i \times t_i$ (mm)	D_i/t_i	f_{syi} (MPa)	χ (D_i/D_o)	$f_{c,t}$ (MPa)		L/D	$N_{u,e}$ (kN)
[26]	1	C4-36-0.18-5-1	190.6 × 5.15	37.0	346.9	34.0 × 3.08	11.0	348.2	0.18	37.5	$f_{c,cyl150}$	3.0	2718
	2	C4-36-0.18-5-2	190.5 × 5.13	37.1	346.9	33.9 × 3.10	10.9	348.2	0.18	37.5			2724
	3	C4-36-0.31-5-1	190.5 × 5.15	37.0	346.9	59.6 × 3.32	18.0	342.1	0.31	37.5			2718
	4	C4-36-0.31-5-2	188.2 × 5.04	37.3	346.9	59.1 × 3.28	18.0	342.1	0.31	37.5			2482
	5	C4-36-0.53-5-1	190.7 × 5.11	37.3	346.9	101.6 × 4.03	25.2	345.8	0.53	37.5			2626
	6	C4-36-0.53-5-2	189.2 × 5.08	37.2	346.9	101.2 × 4.05	25.0	345.8	0.53	37.5			2462
	7	C9-36-0.18-5-1	188.9 × 5.09	37.1	464.0	33.7 × 3.09	10.9	348.2	0.18	37.5			3182
	8	C9-36-0.18-5-2	188.9 × 5.12	36.9	464.0	33.5 × 3.06	10.9	348.2	0.18	37.5			3232
	9	C9-36-0.31-5-1	191.0 × 5.15	37.1	464.0	59.4 × 3.31	17.9	342.1	0.31	37.5			3286
	10	C9-36-0.31-5-2	190.1 × 5.11	37.2	464.0	59.1 × 3.29	18.0	342.1	0.31	37.5			3242
	11	C9-36-0.53-5-1	190.7 × 5.15	37.0	464.0	101.1 × 4.10	24.7	345.8	0.53	37.5			3082
	12	C9-36-0.53-5-2	190.7 × 5.09	37.5	464.0	100.9 × 4.07	24.8	345.8	0.53	37.5			3192
	13	C4-24-0.31-5-1	190.4 × 5.15	37.0	346.9	59.9 × 3.33	18.0	342.1	0.31	29.0			2460
	14	C4-24-0.31-5-2	190.0 × 5.11	37.2	346.9	59.1 × 3.31	17.9	342.1	0.31	29.0			2494
	15	C4-36-0.31-5-1	189.1 × 5.10	37.1	346.9	59.4 × 3.35	17.7	342.1	0.31	37.5			2623
	16	C4-36-0.31-5-2	190.1 × 5.07	37.5	346.9	59.7 × 3.35	17.8	342.1	0.31	37.5			2588
	17	C4-48-0.31-5-1	189.9 × 5.12	37.1	346.9	58.9 × 3.31	17.8	342.1	0.31	51.0			2950
	18	C4-48-0.31-5-2	188.6 × 5.08	37.1	346.9	58.9 × 3.33	17.7	342.1	0.31	51.0			3026
	19	C4-36-0.31-4-1	190.3 × 4.26	44.7	336.8	59.4 × 3.36	17.7	342.1	0.31	37.5			2376
	20	C4-36-0.31-4-2	190.1 × 4.21	45.2	336.8	59.3 × 3.30	18.0	342.1	0.31	37.5			2406
	21	C4-36-0.31-5-1	189.7 × 5.12	37.1	346.9	59.5 × 3.32	17.9	342.1	0.31	37.5			2611
	22	C4-36-0.31-5-2	188.8 × 5.08	37.2	346.9	59.5 × 3.31	18.0	342.1	0.32	37.5			2579
	23	C4-36-0.31-6-1	189.1 × 6.77	27.9	327.3	59.7 × 3.34	17.9	342.1	0.32	37.5			2894
	24	C4-36-0.31-6-2	188.6 × 6.73	28.0	327.3	59.8 × 3.33	18.0	342.1	0.32	37.5			2928
[40]	25	cc2a	180.0 × 3.00	60.0	275.9	48.0 × 3.00	16.0	396.1	0.27	47.4	$f_{c,cu150}$	3.0	1790
	26	cc2b	180.0 × 3.00	60.0	275.9	48.0 × 3.00	16.0	396.1	0.27	47.4			1791
	27	cc3a	180.0 × 3.00	60.0	275.9	88.0 × 3.00	29.3	370.2	0.49	47.4			1648

Table 4.8. (*continued*)

Refs.	No.	Specimens	$D_o \times t_o$ (mm)	D_o/t_o	f_{syo} (MPa)	$D_i \times t_i$ (mm)	D_i/t_i	f_{syi} (MPa)	χ (D_i/D_o)	$f_{c,t}$ (MPa)		L/D	$N_{u,e}$ (kN)
[40]	28	cc3b	180.0 × 3.00	60.0	275.9	88.0 × 3.00	29.3	370.2	0.49	47.4	$f_{c,cu150}$	3.0	1650
	29	cc4a	180.0 × 3.00	60.0	275.9	140.0 × 3.00	46.7	342.0	0.78	47.4			1435
	30	cc4b	180.0 × 3.00	60.0	275.9	140.0 × 3.00	46.7	342.0	0.78	47.4			1358
	31	cc5a	114.0 × 3.00	38.0	294.5	58.0 × 3.00	19.3	374.5	0.51	47.4			904
	32	cc5b	114.0 × 3.00	38.0	294.5	58.0 × 3.00	19.3	374.5	0.51	47.4			898
	33	cc6a	240.0 × 3.00	80.0	275.9	114.0 × 3.00	38.0	294.5	0.48	47.4			2421
	34	cc6b	240.0 × 3.00	80.0	275.9	114.0 × 3.00	38.0	294.5	0.48	47.4			2460
	35	cc7a	300.0 × 3.00	100.0	275.9	165.0 × 3.00	55.0	320.5	0.55	47.4			3331
	36	cc7b	300.0 × 3.00	100.0	275.9	165.0 × 3.00	55.0	320.5	0.55	47.4			3266
[10]	37	C1-1	350.0 × 3.82	91.6	439.3	231.0 × 2.92	79.1	396.5	0.66	52.5	$f_{c,cu150}$	3.0	5499
	38	C1-2	350.0 × 3.82	91.6	439.3	231.0 × 2.92	79.1	396.5	0.66	52.5			5396
[41]	39	DS-2	300.0 × 2.00	150.0	290.0	180.0 × 2.00	90.0	290.0	0.60	23.3	$f_{c,cyl100}$	3.0	2141
	40	DS-6	300.0 × 4.00	75.0	290.0	180.0 × 2.00	90.0	290.0	0.60	23.3			2693
[35]	41	c10-375	158.0 × 0.90	175.6	221.0	38.0 × 0.90	42.2	221.0	0.24	18.7	No	3.0	635
	42	c10-750	159.0 × 0.90	176.7	221.0	76.0 × 0.90	84.4	221.0	0.48	18.7			540
	43	c10-1125	159.0 × 0.90	176.7	221.0	114.0 × 0.90	126.7	221.0	0.72	18.7			378
	44	c16-375	158.0 × 1.50	105.3	308.0	39.0 × 1.50	26.0	308.0	0.25	18.7			852
	45	c16-750	158.0 × 1.50	105.3	308.0	77.0 × 1.50	51.3	308.0	0.49	18.7			728
	46	c16-1125	158.0 × 1.50	105.3	308.0	114.0 × 1.50	76.0	308.0	0.72	18.7			589
	47	c23-375	158.0 × 2.14	73.8	286.0	40.0 × 2.14	18.7	286.0	0.25	18.7			968
	48	c23-750	158.0 × 2.14	73.8	286.0	77.0 × 2.14	36.0	286.0	0.49	18.7			879
	49	c23-1125	157.0 × 2.14	73.4	286.0	115.0 × 2.14	53.7	286.0	0.73	18.7			704
[11]	50	C1-1	356.0 × 5.50	64.7	618.0	219.0 × 3.30	66.4	356.0	0.62	46.5	$f_{c,cu150}$	3.0	7242
	51	C1-2	356.0 × 5.50	64.7	618.0	219.0 × 3.30	66.4	356.0	0.62	46.5			7159
	52	C2-1	356.0 × 5.50	64.7	618.0	168.0 × 3.30	50.9	356.0	0.47	46.5			6917
	53	C2-2	356.0 × 5.50	64.7	618.0	168.0 × 3.30	50.9	356.0	0.47	46.5			8516
[22]	54	Set1-1-1-2	114.3 × 5.85	19.5	455.0	60.3 × 2.52	23.9	396.0	0.53	40.2	$f_{c,cyl100}$	3.0	1422
	55	Set1-2-1-2	114.3 × 5.85	19.5	455.0	60.3 × 5.77	10.5	310.0	0.53	40.2			1574
	56	Set2-1-1-1	114.3 × 2.73	41.9	285.0	60.3 × 2.52	23.9	396.0	0.53	40.2			735

Table 4.8. (*continued*)

Refs.	No.	Specimens	$D_o \times t_o$ (mm)	D_o/t_o	f_{syo} (MPa)	$D_i \times t_i$ (mm)	D_i/t_i	f_{syi} (MPa)	χ (D_i/D_o)	$f_{c,t}$ (MPa)		L/D	$N_{u,e}$ (kN)
[22]	57	Set2-2-1-1	114.3 × 2.73	41.9	285.0	60.3 × 5.77	10.5	310.0	0.53	40.2	$f_{c,cyl100}$	3.0	913
	58	Set3-1-2-2	114.3 × 5.85	19.5	455.0	60.3 × 2.52	23.9	396.0	0.53	67.3			1506
	59	Set3-2-2-2	114.3 × 5.85	19.5	455.0	60.3 × 5.77	10.5	310.0	0.53	67.3			1666
	60	Set4-1-2-1	114.3 × 2.73	41.9	285.0	60.3 × 2.52	23.9	396.0	0.53	67.3			899
	61	Set4-2-2-1	114.3 × 2.73	41.9	285.0	60.3 × 5.77	10.5	310.0	0.53	67.3			1088
[20]	62	C1C7	114.5 × 5.90	19.4	454.0	48.4 × 2.80	17.3	425.0	0.42	63.4	$f_{c,cyl100}$	3.0	1418
	63	C2C7	114.6 × 4.70	24.4	416.0	48.4 × 2.80	17.3	425.0	0.42	63.4			1390
	64	C3C7	114.4 × 3.50	32.7	453.0	48.4 × 2.80	17.3	425.0	0.42	63.4			1191
	65	C4C7	114.2 × 3.00	38.1	430.0	48.4 × 2.80	17.3	425.0	0.42	63.4			1100
	66	C5C8	165.1 × 3.50	47.2	433.0	101.8 × 3.10	32.8	410.0	0.62	63.4			1700
	67	C6C8	165.3 × 2.90	57.0	395.0	101.8 × 3.10	32.8	410.0	0.62	63.4			1591
[19]	68	A1-1	74.8 × 1.03	72.6	486.0	62.0 × 1.00	62.0	470.0	0.83	58.6	No	3.0	283
	69	A1-2	74.7 × 0.97	77.0	486.0	62.0 × 0.94	66.0	470.0	0.83	58.6			285
	70	A2-1	75.4 × 1.29	58.4	486.0	62.7 × 1.23	51.0	470.0	0.83	58.6			348
	71	A2-2	75.2 × 1.19	63.2	486.0	62.4 × 1.20	52.0	470.0	0.83	58.6			348
	72	A3-1	76.3 × 1.78	42.9	486.0	62.0 × 1.00	62.0	470.0	0.81	58.6			395
	73	A3-2	76.3 × 1.74	43.9	512.0	62.0 × 0.94	66.0	470.0	0.81	58.6			395
	74	B1-1	81.0 × 0.90	90.0	524.0	62.0 × 1.00	62.0	470.0	0.77	58.6		2.8	330
	75	B1-2	81.0 × 0.87	93.1	524.0	62.0 × 0.94	66.0	470.0	0.77	58.6			335
	76	B2-1	81.5 × 1.11	73.4	524.0	62.7 × 1.14	55.0	470.0	0.77	58.6			386
	77	B2-2	81.5 × 1.14	71.5	524.0	62.2 × 1.13	55.0	470.0	0.76	58.6			395
	78	C1-1	87.4 × 0.99	88.3	428.0	61.8 × 0.87	71.0	452.0	0.71	58.6		2.6	378
	79	C1-2	87.3 × 0.94	92.9	428.0	61.6 × 0.88	70.0	452.0	0.71	58.6			385
	80	C2-1	87.9 × 1.26	69.8	428.0	61.4 × 0.89	69.0	452.0	0.70	58.6			432
	81	C2-2	87.9 × 1.17	75.1	444.0	61.2 × 0.85	72.0	452.0	0.70	58.6			408
	82	D1-1	99.7 × 0.59	169.0	409.0	80.3 × 0.55	146.0	474.0	0.81	58.6		2.3	283
	83	D2-1	99.9 × 0.69	144.8	409.0	86.8 × 0.61	142.3	444.0	0.87	58.6			299

Table 4.8. (*continued*)

Refs.	No.	Specimens	$D_o \times t_o$ (mm)	D_o/t_o	f_{syo} (MPa)	$D_i \times t_i$ (mm)	D_i/t_i	f_{syi} (MPa)	χ (D_i/D_o)	$f_{c,t}$ (MPa)		L/D	$N_{u,e}$ (kN)
[19]	84	D3-1	99.9 × 0.71	140.7	409.0	80.5 × 0.67	120.1	474.0	0.81	58.6	No	2.3	357
	85	D4-1	99.9 × 0.70	142.7	409.0	74.0 × 0.62	119.4	512.0	0.74	58.6			380
	86	D5-1	99.8 × 0.66	151.2	409.0	61.4 × 0.55	111.6	432.0	0.62	58.6			443
	87	D6-1	101.7 × 1.61	63.2	409.0	61.5 × 0.56	109.8	432.0	0.60	58.6			644
	88	E1-1	88.8 × 1.55	57.3	286.0	63.5 × 1.16	54.7	216.0	0.72	58.6			357
	89	E2-1	101.4 × 1.56	65.0	255.0	63.4 × 1.15	55.1	216.0	0.63	58.6			477
	90	E3-1	101.5 × 1.65	61.5	255.0	76.1 × 1.19	63.9	235.0	0.75	58.6			417
	91	E4-1	114.3 × 1.64	69.7	262.0	63.5 × 1.12	56.7	216.0	0.56	58.6			598
	92	E5-1	114.3 × 1.64	69.7	262.0	76.1 × 1.14	66.8	235.0	0.67	58.6		2.0	551
	93	E6-1	114.3 × 1.64	69.7	262.0	88.9 × 1.56	57.0	286.0	0.78	58.6			524
[42]	94	CC3 240-120	240.0 × 3.00	80.0	280.0	120.0 × 3.00	40.0	280.0	0.50	29.0	$f_{c,cyl150}$	3.0	1990
	95	CC3 240-120(R)	240.0 × 3.00	80.0	280.0	120.0 × 3.00	40.0	280.0	0.50	29.0			1990
	96	CC3 240-80	240.0 × 3.00	80.0	280.0	80.0 × 3.00	26.7	280.0	0.33	29.0			2207
	97	CC3 240-80(R)	240.0 × 3.00	80.0	280.0	80.0 × 3.00	26.7	280.0	0.33	29.0			2207
	98	CC4 240-120	240.0 × 4.00	60.0	280.0	120.0 × 4.00	30.0	280.0	0.50	29.0			2517
	99	CC4 240-120(R)	240.0 × 4.00	60.0	280.0	120.0 × 4.00	30.0	280.0	0.50	29.0			2517
	100	CC4 240-80	240.0 × 4.00	60.0	280.0	80.0 × 4.00	20.0	280.0	0.33	29.0			2735
	101	CC4 240-80(R)	240.0 × 4.00	60.0	280.0	80.0 × 4.00	20.0	280.0	0.33	29.0			2735
[23]	102	0-1-1-1	114.3 × 2.74	41.7	355.0	60.3 × 2.52	23.9	396.0	0.53	42.9	$f_{c,cyl100}$	3.0	789
	103	0-1-1-2	114.3 × 6.11	18.7	535.0	60.3 × 2.52	23.9	396.0	0.53	42.9			1682
	104	0-2-1-1	114.3 × 2.74	41.7	355.0	60.3 × 5.77	10.5	310.0	0.53	42.9			969
	105	0-2-1-2	114.3 × 6.11	18.7	535.0	60.3 × 5.77	10.5	310.0	0.53	42.9			1823
	106	0-1-2-1	114.3 × 2.74	41.7	355.0	60.3 × 2.52	23.9	396.0	0.53	71.0			914
	107	0-1-2-2	114.3 × 6.11	18.7	535.0	60.3 × 2.52	23.9	396.0	0.53	71.0			1753
	108	0-2-2-1	114.3 × 2.74	41.7	355.0	60.3 × 5.77	10.5	310.0	0.53	71.0			1068
	109	0-2-2-2	114.3 × 6.11	18.7	535.0	60.3 × 5.77	10.5	310.0	0.53	71.0			1890
[43]	110	CFDST-CC1	166.3 × 5.24	31.7	520.0	76.7 × 3.58	21.4	520.0	0.46	41.9	$f_{c,cu150}$	2.7	2692
	111	CFDST-CC2	166.0 × 5.22	31.8	520.0	76.7 × 3.58	21.4	520.0	0.46	42.8			2745

Table 4.8. (*continued*)

Refs.	No.	Specimens	$D_o \times t_o$ (mm)	D_o/t_o	f_{syo} (MPa)	$D_i \times t_i$ (mm)	D_i/t_i	f_{syi} (MPa)	χ (D_i/D_o)	$f_{c,t}$ (MPa)		L/D	$N_{u,e}$ (kN)
[44]	112	GC1-1	140.0 × 2.50	56.0	307.0	114.0 × 2.00	57.0	321.0	0.81	51.1	$f_{c,cu100}$	3.0	755
	113	GC1-2	140.0 × 2.50	56.0	307.0	114.0 × 2.00	57.0	321.0	0.81	51.1			701
	114	GC2-1	140.0 × 2.50	56.0	307.0	76.0 × 1.60	47.5	429.0	0.54	51.1			942
	115	GC2-2	140.0 × 2.50	56.0	307.0	76.0 × 1.60	47.5	429.0	0.54	51.1			928
	116	GCL-1	450.0 × 8.00	56.3	365.0	400.0 × 8.00	50.0	363.0	0.89	54.8			8906
	117	GCL-2	450.0 × 8.00	56.3	365.0	400.0 × 8.00	50.0	363.0	0.89	54.8			8774
[21]	118	O1I1-S	114.3 × 6.00	19.1	454.0	48.3 × 2.90	16.7	425.0	0.42	63.4	$f_{c,cyl100}$	3.0	1665
	119	O2I1-S	114.3 × 4.80	23.8	416.0	48.3 × 2.90	16.7	425.0	0.42	63.4			1441
	120	O3I1-S	114.3 × 3.60	31.8	453.0	48.3 × 2.90	16.7	425.0	0.42	63.4			1243
	121	O4I1-S	114.3 × 3.20	35.7	430.0	48.3 × 2.90	16.7	425.0	0.42	63.4			1145
	122	O5I2-S	165.1 × 3.50	47.2	433.0	101.6 × 3.30	30.8	394.0	0.62	63.4			1629
	123	O6I2-S	165.1 × 3.00	55.0	395.0	101.6 × 3.30	30.8	394.0	0.62	63.4			1613
	124	O7I2-S	163.8 × 2.35	69.7	395.0	101.6 × 3.30	30.8	394.0	0.62	63.4			1487
	125	O8I2-S	163.0 × 1.95	83.6	395.0	101.6 × 3.30	30.8	394.0	0.62	63.4			1328
	126	O9I2-S	162.5 × 1.70	95.6	395.0	101.6 × 3.30	30.8	394.0	0.63	63.4			1236

Table 4.9. Comparisons of all test strengths-to-predicted strengths

Refs.	No.	$N_{u,c}$ (kN)	Ref. [25]		Ref. [24]		Ref. [34]		Ref. [35]		Ref. [33]		Ref. [36]		Proposed model	
			$N_{u,c}$	$N_{u,c}/N_{u,e}$	$N_{u,c}$	$N_{u,c}/N_{u,e}$	$N_{u,c}$	$N_{u,c}/N_{u,e}$	$N_{u,c}$	$N_{u,c}/N_{u,e}$	$N_{u,c}$	$N_{u,c}/N_{u,e}$	$N_{u,c}$	$N_{u,c}/N_{u,e}$	$N_{u,c}$	$N_{u,c}/N_{u,e}$
[26]	1	2718	2022	0.74	2701	0.99	2085	0.77	2839	1.04	2476	0.91	2533	0.93	2638	0.97
	2	2724	2018	0.74	2694	0.99	2079	0.76	2831	1.04	2470	0.91	2527	0.93	2631	0.97
	3	2718	2050	0.75	2659	0.98	2108	0.78	2800	1.03	2481	0.91	2483	0.91	2578	0.95
	4	2482	1993	0.80	2582	1.04	2048	0.83	2720	1.10	2411	0.97	2413	0.97	2503	1.01
	5	2626	2083	0.79	2498	0.95	2127	0.81	2646	1.01	2424	0.92	2346	0.89	2400	0.91
	6	2462	2057	0.84	2464	1.00	2100	0.85	2611	1.06	2394	0.97	2319	0.94	2367	0.96
	7	3182	2329	0.73	3181	1.00	2375	0.75	3297	1.04	2829	0.89	2836	0.89	3121	0.98
	8	3232	2335	0.72	3191	0.99	2382	0.74	3308	1.02	2837	0.88	2843	0.88	3132	0.97
	9	3286	2410	0.73	3192	0.97	2453	0.75	3319	1.01	2893	0.88	2850	0.87	3105	0.95
	10	3242	2383	0.74	3156	0.97	2425	0.75	3282	1.01	2861	0.88	2819	0.87	3070	0.95
	11	3082	2450	0.79	2985	0.97	2483	0.81	3136	1.02	2836	0.92	2729	0.89	2868	0.93
	12	3192	2432	0.76	2964	0.93	2464	0.77	3114	0.98	2814	0.88	2708	0.85	2848	0.89
	13	2460	1866	0.76	2472	1.00	1901	0.77	2550	1.04	2237	0.91	2287	0.93	2383	0.97
	14	2494	1852	0.74	2454	0.98	1886	0.76	2532	1.02	2220	0.89	2272	0.91	2367	0.95
	15	2623	2021	0.77	2619	1.00	2078	0.79	2759	1.05	2445	0.93	2448	0.93	2539	0.97
	16	2588	2032	0.79	2631	1.02	2087	0.81	2770	1.07	2455	0.95	2460	0.95	2551	0.99
	17	2950	2320	0.79	2929	0.99	2418	0.82	3137	1.06	2815	0.95	2771	0.94	2860	0.97
	18	3026	2289	0.76	2888	0.95	2386	0.79	3095	1.02	2778	0.92	2735	0.90	2820	0.93
	19	2376	1867	0.79	2377	1.00	1903	0.80	2495	1.05	2224	0.94	2276	0.96	2306	0.97
	20	2406	1852	0.77	2357	0.98	1887	0.78	2473	1.03	2204	0.92	2256	0.94	2286	0.95
	21	2611	2032	0.78	2635	1.01	2089	0.80	2775	1.06	2458	0.94	2460	0.94	2555	0.98
	22	2579	2011	0.78	2605	1.01	2067	0.80	2744	1.06	2431	0.94	2433	0.94	2526	0.98
	23	2894	2234	0.77	2940	1.02	2351	0.81	3090	1.07	2739	0.95	2717	0.94	2853	0.99
	24	2928	2219	0.76	2918	1.00	2334	0.80	3067	1.05	2719	0.93	2697	0.92	2831	0.97
[40]	25	1790	1457	0.81	1774	0.99	1483	0.83	1681	0.94	1536	0.86	1852	1.03	1734	0.97
	26	1791	1457	0.81	1774	0.99	1483	0.83	1681	0.94	1536	0.86	1852	1.03	1734	0.97
	27	1648	1424	0.86	1663	1.01	1445	0.88	1603	0.97	1484	0.90	1631	0.99	1611	0.98

Table 4.9. (*continued*)

Refs.	No.	$N_{u,e}$ (kN)	Ref. [25]		Ref. [24]		Ref. [34]		Ref. [35]		Ref. [33]		Ref. [36]		Proposed model	
			$N_{u,c}$	$N_{u,c}/N_{u,e}$	$N_{u,c}$	$N_{u,c}/N_{u,e}$	$N_{u,c}$	$N_{u,c}/N_{u,e}$	$N_{u,c}$	$N_{u,c}/N_{u,e}$	$N_{u,c}$	$N_{u,c}/N_{u,e}$	$N_{u,c}$	$N_{u,c}/N_{u,e}$	$N_{u,c}$	$N_{u,c}/N_{u,e}$
[40]	28	1650	1424	0.86	1663	1.01	1445	0.88	1603	0.97	1484	0.90	1631	0.99	1611	0.98
	29	1435	1218	0.85	1282	0.89	1228	0.86	1301	0.91	1230	0.86	1217	0.85	1269	0.88
	30	1358	1218	0.90	1282	0.94	1228	0.90	1301	0.96	1230	0.91	1217	0.90	1269	0.93
	31	904	748	0.83	883	0.98	767	0.85	955	1.06	891	0.99	878	0.97	853	0.94
	32	898	748	0.83	883	0.98	767	0.85	955	1.06	891	0.99	878	0.98	853	0.95
	33	2421	2161	0.89	2505	1.03	2184	0.90	2360	0.97	2171	0.90	2522	1.04	2441	1.01
	34	2460	2161	0.88	2505	1.02	2184	0.89	2360	0.96	2171	0.88	2522	1.03	2441	0.99
	35	3331	3016	0.91	3345	1.00	3039	0.91	3159	0.95	2915	0.87	3192	0.96	3325	1.00
	36	3266	3016	0.92	3345	1.02	3039	0.93	3159	0.97	2915	0.89	3192	0.98	3325	1.02
[10]	37	5499	5047	0.92	4829	0.88	4770	0.87	5138	0.93	4636	0.84	4701	0.85	5205	0.95
	38	5396	5047	0.94	4829	0.89	4770	0.88	5138	0.95	4636	0.86	4701	0.87	5205	0.96
[41]	39	2141	1535	0.72	1883	0.88	1778	0.83	1854	0.87	1669	0.78	1762	0.82	1968	0.92
	40	2693	2287	0.85	2676	0.99	2275	0.84	2600	0.97	2298	0.85	2253	0.84	2581	0.96
[35]	41	635	357	0.56	505	0.80	439	0.69	408	0.64	/	/	2367	3.73	511	0.80
	42	540	340	0.63	455	0.84	408	0.76	382	0.71	/	/	1322	2.45	459	0.85
	43	378	290	0.77	336	0.89	332	0.88	316	0.83	/	/	325	0.86	355	0.94
	44	852	642	0.75	727	0.85	586	0.69	721	0.85	630	0.74	1153	1.35	732	0.86
	45	728	693	0.95	679	0.93	581	0.80	690	0.95	609	0.84	771	1.06	680	0.93
	46	589	704	1.19	559	0.95	539	0.92	604	1.03	541	0.92	524	0.89	581	0.99
	47	968	680	0.70	889	0.92	672	0.69	848	0.88	740	0.76	998	1.03	851	0.88
	48	879	691	0.79	846	0.96	684	0.78	824	0.94	733	0.83	815	0.93	804	0.91
	49	704	656	0.93	718	1.02	652	0.93	731	1.04	668	0.95	643	0.91	696	0.99
[11]	50	7242	6030	0.83	6977	0.96	6538	0.90	7676	1.06	6756	0.93	6525	0.90	7499	1.04
	51	7159	6030	0.84	6977	0.97	6538	0.91	7676	1.07	6756	0.94	6525	0.91	7499	1.05
	52	6917	6263	0.91	7992	1.16	6905	1.00	8375	1.21	7257	1.05	6961	1.01	8415	1.22
	53	8516	6263	0.74	7943	0.93	6905	0.81	8375	0.98	7257	0.85	6961	0.82	8415	0.99
[22]	54	1422	1286	0.90	1562	1.10	1371	0.96	1650	1.16	1529	1.08	1462	1.03	1519	1.07
	55	1574	1412	0.90	1685	1.07	1497	0.95	1776	1.13	1674	1.06	1652	1.05	1645	1.04
	56	735	690	0.94	808	1.10	705	0.96	873	1.19	812	1.11	791	1.08	780	1.06

Table 4.9. (*continued*)

Refs.	No.	$N_{u,e}$ (kN)	Ref. [25]		Ref. [24]		Ref. [34]		Ref. [35]		Ref. [33]		Ref. [36]		Proposed model	
			$N_{u,c}$	$N_{u,c}/N_{u,e}$	$N_{u,c}$	$N_{u,c}/N_{u,e}$	$N_{u,c}$	$N_{u,c}/N_{u,e}$	$N_{u,c}$	$N_{u,c}/N_{u,e}$	$N_{u,c}$	$N_{u,c}/N_{u,e}$	$N_{u,c}$	$N_{u,c}/N_{u,e}$	$N_{u,c}$	$N_{u,c}/N_{u,e}$
[22]	57	913	816	0.89	931	1.02	830	0.91	999	1.09	957	1.05	969	1.06	905	0.99
	58	1506	1396	0.93	1673	1.11	1538	1.02	1849	1.23	1720	1.14	1603	1.06	1635	1.09
	59	1666	1521	0.91	1796	1.08	1663	1.00	1974	1.18	1865	1.12	1792	1.08	1760	1.06
	60	899	821	0.91	942	1.05	882	0.98	1051	1.17	990	1.10	958	1.07	917	1.02
	61	1088	946	0.87	1066	0.98	1007	0.93	1176	1.08	1135	1.04	1137	1.04	1043	0.96
[20]	62	1418	1437	1.01	1802	1.27	1594	1.12	1968	1.39	1798	1.27	1697	1.20	1772	1.25
	63	1390	1220	0.88	1517	1.09	1326	0.95	1679	1.21	1532	1.10	1445	1.04	1483	1.07
	64	1191	1118	0.94	1377	1.16	1186	1.00	1539	1.29	1400	1.18	1314	1.10	1344	1.13
	65	1100	1023	0.93	1244	1.13	1080	0.98	1395	1.27	1276	1.16	1207	1.10	1214	1.10
	66	1700	1792	1.05	2042	1.20	1861	1.09	2061	1.21	1915	1.13	1918	1.13	1981	1.17
	67	1591	1626	1.02	1818	1.14	1689	1.06	1849	1.16	1727	1.09	1768	1.11	1782	1.12
[19]	68	283	350	1.24	239	0.84	270	0.95	292	1.03	272	0.96	264	0.93	275	0.97
	69	285	326	1.14	225	0.79	258	0.91	279	0.98	259	0.91	251	0.88	263	0.92
	70	348	315	0.91	297	0.85	319	0.92	342	0.98	324	0.93	315	0.90	324	0.93
	71	348	410	1.18	282	0.81	306	0.88	328	0.94	310	0.89	301	0.86	311	0.89
	72	395	353	0.89	360	0.91	359	0.91	407	1.03	385	0.97	356	0.90	365	0.92
	73	395	354	0.90	342	0.87	360	0.91	409	1.04	386	0.98	357	0.90	367	0.93
	74	330	279	0.85	286	0.87	315	0.96	349	1.06	321	0.97	309	0.94	326	0.99
	75	335	269	0.80	276	0.82	307	0.92	339	1.01	312	0.93	300	0.89	317	0.95
	76	386	323	0.84	331	0.86	354	0.92	392	1.02	363	0.94	349	0.90	366	0.95
	77	395	432	1.09	337	0.85	359	0.91	398	1.01	369	0.93	354	0.90	372	0.94
	78	378	375	0.99	330	0.87	344	0.91	384	1.02	354	0.94	339	0.90	359	0.95
	79	385	292	0.76	325	0.84	340	0.88	379	0.98	349	0.91	335	0.87	354	0.92
	80	432	371	0.86	377	0.87	380	0.88	428	0.99	393	0.91	375	0.87	399	0.92
	81	408	430	1.05	365	0.89	373	0.92	421	1.03	386	0.95	368	0.90	392	0.96
	82	283	233	0.82	235	0.83	284	1.00	268	0.95	/	/	275	0.97	289	1.02
	83	299	221	0.74	197	0.66	257	0.86	270	0.90	247	0.83	244	0.82	260	0.87

Table 4.9. (*continued*)

Refs.	No.	$N_{u,e}$ (kN)	Ref. [25]		Ref. [24]		Ref. [34]		Ref. [35]		Ref. [33]		Ref. [36]		Proposed model	
			$N_{u,c}$	$N_{u,c}/N_{u,e}$	$N_{u,c}$	$N_{u,c}/N_{u,e}$	$N_{u,c}$	$N_{u,c}/N_{u,e}$	$N_{u,c}$	$N_{u,c}/N_{u,e}$	$N_{u,c}$	$N_{u,c}/N_{u,e}$	$N_{u,c}$	$N_{u,c}/N_{u,e}$	$N_{u,c}$	$N_{u,c}/N_{u,e}$
[19]	84	357	262	0.74	260	0.73	312	0.87	333	0.93	306	0.86	301	0.84	318	0.89
	85	380	286	0.75	306	0.81	349	0.92	376	0.99	346	0.91	341	0.90	359	0.94
	86	443	305	0.69	375	0.85	391	0.88	361	0.82	/	/	390	0.88	409	0.92
	87	644	501	0.78	548	0.85	519	0.81	600	0.93	544	0.84	514	0.80	560	0.87
	88	357	309	0.87	339	0.95	322	0.90	355	0.99	331	0.93	319	0.89	331	0.93
	89	477	409	0.86	460	0.96	431	0.90	476	1.00	444	0.93	427	0.89	447	0.94
	90	417	359	0.86	387	0.93	374	0.90	405	0.97	380	0.91	368	0.88	380	0.91
	91	598	546	0.91	623	1.04	576	0.96	636	1.06	591	0.99	573	0.96	606	1.01
	92	551	489	0.89	543	0.98	512	0.93	558	1.01	521	0.95	506	0.92	528	0.96
	93	524	460	0.88	486	0.93	475	0.91	506	0.97	478	0.91	468	0.89	481	0.92
[42]	94	1990	1807	0.91	2125	1.07	1811	0.91	2026	1.02	1837	0.92	2073	1.04	2056	1.03
	95	1990	1807	0.91	2125	1.07	1811	0.91	2026	1.02	1837	0.92	2073	1.04	2056	1.03
	96	2207	1875	0.85	2282	1.03	1879	0.85	2139	0.97	1925	0.87	2579	1.17	2221	1.01
	97	2207	1875	0.85	2282	1.03	1879	0.85	2139	0.97	1925	0.87	2579	1.17	2221	1.01
	98	2517	2092	0.83	2506	1.00	2104	0.84	2385	0.95	2169	0.86	2414	0.96	2401	0.95
	99	2517	2092	0.83	2506	1.00	2104	0.84	2385	0.95	2169	0.86	2414	0.96	2401	0.95
	100	2735	2124	0.78	2655	0.97	2139	0.78	2479	0.91	2226	0.81	2729	1.00	2561	0.94
	101	2735	2124	0.78	2655	0.97	2139	0.78	2479	0.91	2226	0.81	2729	1.00	2561	0.94
[23]	102	789	774	0.98	916	1.16	788	1.00	991	1.25	913	1.16	876	1.11	884	1.12
	103	1682	1501	0.89	1821	1.08	1606	0.96	1920	1.14	1779	1.06	1699	1.01	1781	1.06
	104	969	900	0.93	1039	1.07	913	0.94	1116	1.15	1057	1.09	1055	1.09	1009	1.04
	105	1823	1626	0.89	1943	1.07	1732	0.95	2045	1.12	1923	1.05	1889	1.04	1906	1.05
	106	914	902	0.99	1047	1.14	971	1.06	1189	1.30	1110	1.21	1050	1.15	1018	1.11
	107	1753	1606	0.92	1927	1.10	1779	1.01	2135	1.22	1984	1.13	1843	1.05	1891	1.08
	108	1068	1027	0.96	1171	1.10	1097	1.03	1314	1.23	1255	1.17	1229	1.15	1143	1.07
	109	1890	1731	0.92	2050	1.09	1904	1.01	2261	1.20	2129	1.13	2032	1.08	2017	1.07
[43]	110	2692	2282	0.85	2883	1.07	2323	0.86	2967	1.10	2665	0.99	2588	0.96	2770	1.03
	111	2745	2283	0.83	2878	1.05	2324	0.85	2970	1.08	2669	0.97	2587	0.94	2767	1.01

Table 4.9. (*continued*)

Refs.	No.	$N_{u,e}$ (kN)	Ref. [25]		Ref. [24]		Ref. [34]		Ref. [35]		Ref. [33]		Ref. [36]		Proposed model	
			$N_{u,c}$	$N_{u,c}/N_{u,e}$	$N_{u,c}$	$N_{u,c}/N_{u,e}$	$N_{u,c}$	$N_{u,c}/N_{u,e}$	$N_{u,c}$	$N_{u,c}/N_{u,e}$	$N_{u,c}$	$N_{u,c}/N_{u,e}$	$N_{u,c}$	$N_{u,c}/N_{u,e}$	$N_{u,c}$	$N_{u,c}/N_{u,e}$
[44]	112	755	718	0.95	740	0.98	723	0.96	772	1.02	726	0.96	712	0.94	743	0.98
	113	701	718	1.02	740	1.06	723	1.03	772	1.10	726	1.04	712	1.02	743	1.06
	114	942	875	0.93	1023	1.09	887	0.94	1007	1.07	919	0.98	885	0.94	987	1.05
	115	928	875	0.94	1023	1.10	887	0.96	1007	1.08	919	0.99	885	0.95	987	1.06
	116	8906	8572	0.96	8286	0.93	8598	0.97	8767	0.98	8426	0.95	8468	0.95	8677	0.97
	117	8774	8572	0.98	8286	0.94	8598	0.98	8767	1.00	8426	0.96	8468	0.97	8677	0.99
[21]	118	1665	1452	0.87	1819	1.09	1614	0.97	1985	1.19	1816	1.09	1718	1.03	1790	1.08
	119	1441	1233	0.86	1533	1.06	1342	0.93	1694	1.18	1548	1.07	1463	1.02	1499	1.04
	120	1243	1136	0.91	1399	1.13	1206	0.97	1563	1.26	1423	1.14	1337	1.08	1367	1.10
	121	1145	1056	0.92	1288	1.12	1117	0.98	1443	1.26	1320	1.15	1248	1.09	1258	1.10
	122	1629	1801	1.11	2052	1.26	1871	1.15	2071	1.27	1927	1.18	1954	1.20	1991	1.22
	123	1613	1649	1.02	1853	1.15	1714	1.06	1876	1.16	1755	1.09	1811	1.12	1809	1.12
	124	1487	1516	1.02	1644	1.11	1572	1.06	1708	1.15	1605	1.08	1718	1.16	1649	1.11
	125	1328	1813	1.36	1524	1.15	1486	1.12	1601	1.21	1512	1.14	1701	1.28	1551	1.17
	126	1236	1627	1.32	1453	1.18	1433	1.16	1532	1.24	1452	1.17	1727	1.40	1490	1.21

'/' indicates that the experimental parameters exceed the limitations specified by design models.

Table 4.10. Means and CoVs of all test strengths-to-predicted strengths

Design models	Ref. [25]	Ref. [24]	Ref. [34]	Ref. [35]	Ref. [33]	Ref. [36]	Proposed model
150 test data	$N_{u,c}/N_{u,e}$	$N_{u,c}/N_{u,e}$	$N_{u,c}/N_{u,e}$	$N_{u,c}/N_{u,e}$	$N_{u,c}/N_{u,e}$	$N_{u,c}/N_{u,e}$	$N_{u,c}/N_{u,e}$
Mean	0.88	1.00	0.91	1.06	0.98	1.02	1.00
SD	0.12	0.10	0.11	0.12	0.11	0.27	0.08
CoV	0.13	0.10	0.12	0.11	0.11	0.27	0.08

Refs. [12]. The parameters of the columns investigated may often exceed these limitations, but comparisons are still made to explore the possible extension of the EC4 and AISC 360 beyond their current scope of applicability. In current paper, the effective concrete strength is employed for EC4 [24] and AISC 360 [25] to account for the strength reduction of higher concrete grade. The effective concrete strength is defined by multiplying the concrete strength by a reduction factor η_r recommended by Wang et al. [12] based on the work of Liew et al. [14] and EN 1992-1-1 [16], as Eq. (7).

$$\eta_r = \begin{cases} 1.0 & f_c \le 50\text{MPa} \\ 1.0 - \frac{f_c - 50}{200} & 50\text{MPa} < f_c \le 90\text{MPa} \\ 0.8 & f_c > 90\text{MPa} \end{cases} \tag{4.7}$$

Besides, AISC 360 [25] divides the filled composite cross-sections into three types according to the slenderness ratios (D/t ratios) of the outer tubes, i.e., compact, noncompact, and slender. Based on different cross-section types, different formulas are used to calculate the cross-section resistances of the CFDST columns; see Table 4.6. However, EC4 [24] allows using circular steel tubes with a local slenderness ratio $D/t \le 90(235/f_{sy})$. When the D/t ratio of circular steel tube exceeds $90(235/f_{sy})$, an effective area needs to be introduced to account for the local buckling. Recently, Chan and Gardner [37] developed an effective area formula to calculate the effective area (A_{eff}) of CHS based on the formula specified in BS5950-1 [38]; see Table 4.6. It was confirmed by Wang et al. [12] to be feasible in calculating the effective area of the stainless outer steel tube in circular CFDST columns with outer stainless and inner carbon steel tubes. In this paper, the effective area formula developed by Chan and Gardner [37] is employed to calculate the effective areas of the outer and inner steel tubes in circular CFDST columns when the D_o/t_o and D_i/t_i ratios are greater than $90(235/f_{sy})$.

Similar to the design codes, the empirical models given by the previous researchers, such as Hassanein et al. [33], Han et al. [34], Uenaka et al. [35], and Liang [36], were developed based on a limited range of column parameters in their respective studies. To examine their effectiveness in designing CFDST columns with an extensive parameters, such as high-strength steel (HSS) or HSC, these empirical models are also evaluated based the conducted and collected experimental results.

4.5.1.1. Investigation based on the conducted test results

Based on the conducted test results shown in Table 4.1, the ultimate strengths ($N_{u,c}$) of the CFDST columns predicted by the existing design codes and the empirical models are listed Table 4.7. Also, comparisons between the predicted-to-experimental strengths ($N_{u,c}/N_{u,e}$) are shown Table 4.7. From this table, it can be found that AISC 360 provides on average conservative predictions for the cross-sectional resistances of the CFDST columns, while EC4, Hassanein et al., Han et al., Uenaka et al., and Liang, overestimate the cross-sectional resistances of the CFDST columns. As can be noticed, although the mean of the predictions given by Han's model is closer to the unity than those of other models, its standard deviation (SD) and CoV are the largest. The mean of the predictions provided by EC4 is 1.05 with a SD of 0.03 and a CoV of 0.02. Generally, EC4 suitably predicts the cross-sectional resistances of the CFDST columns.

4.5.1.2. Investigation based on the conducted and collected test results

In the above section, based on the conducted test data, the applicability of the prediction models specified in the existing design codes and the empirical models given by the previous researchers was investigated. Nevertheless, this test data pool is very limited. Therefore, a general database constructed using the collected and conducted test results on the circular CFDST short columns with outer and inner carbon steel tubes, is employed herein to further check the applicability of these models.

A summary of the conducted and collected experimental data is performed, the details of which are listed in Table 4.1 and Table 4.8. As shown in Table 4.1 and Table 4.8, the ratio (L/D_o) of column length to tube diameter of all selected columns ranges from 2 to 3, which is less than 4, and thus the influences of global imperfections are ignored [39]. In Table 4.8, $f_{c,t}$ stands for the compressive strength of concrete obtained from the material tests of concrete based on different dimensions. $f_{c,cu150}$ and $f_{c,cu100}$ are the concrete cube strengths (150 mm cube and 100 mm cube), respectively, $f_{c,cyl100}$ is the concrete cylinder strengths (100 × 200 mm cylinder), $f_{c,cyl150}$ (i.e., f_c) denotes the standard concrete cylinder strengths (150 × 300 mm cylinder) [28]. In order to facilitate the comparison, the following expressions are used to convert $f_{c,cu150}$, $f_{c,cu100}$, and $f_{c,cyl100}$ into the standard concrete cylinder strength f_c [39,45-46].

$$f_{c,cu150} = 0.96 f_{c,cu100} \tag{4.8}$$

$$f_c = \left[0.76 + 0.2\log_{10}\left(\frac{f_{c,cu150}}{19.6}\right)\right] f_{c,cu150} \tag{4.9}$$

$$f_c = 0.96 f_{c,cyl100} \tag{4.10}$$

It should be noted that Uenaka et al. [35] does not give the specific size of the specimens used in the material tests of the concrete. In the current paper, the concrete strength provided by Uenaka et al. is assumed as the standard concrete cylinder strength f_c. In addition, the concrete strength given by Wei et al. [19] is obtained from the average test strengths of the concrete cylinder specimens with a diameter of 60 mm and a height ranging from 160 to 190 mm. Similar to Ref. [35], such concrete strength would be assumed as the standard concrete cylinder strength f_c in this paper. Generally, the limitations of all the experimental data about the studied CFDST columns are described as follows:

(1) The hollow ratio χ (D_i/D_o) varies from 0.18 to 0.89;

(2) The unconfined concrete strength (f_c) ranges from 18.7 MPa to 141.0 MPa;

(3) The diameter-to-thickness ratios of the outer and inner steel tubes range from 18.7 to 176.7 and 10.5 to 146.0, respectively;

(4) The yield strengths of the outer and inner steel tubes range from 221.0 MPa to 618.0 MPa and 216.0 MPa to 520.0 MPa, respectively.

From the above summary, it can be found that the current test database not only consists of a wide range of concrete strengths, but also a wide-scope of yield stresses and diameter-to-thickness ratios of outer and inner steel tubes as well as hollow ratios. Utilizing this database, the ultimate strengths ($N_{u,c}$) of the CFDST columns predicted by the existing design codes and the empirical models and their comparisons with the experimental strengths are shown Table 4.7 and Table 4.9. Also, the mean, SD, and CoV of the predicted-to-experimental strengths ($N_{u,c}/N_{u,e}$) are shown Table 4.10. From Table

4.10, it can be seen that AISC 360, Han et al., and Hassanein et al. provide on average conservative predictions for the cross-sectional resistances of the CFDST columns, while Uenaka et al. and Liang overestimate the cross-sectional resistances of the CFDST columns. The mean of the comparisons between the predictions given by EC4 and the experimental strengths is 1.00 with a SD of 0.10 and a CoV of 0.10. Generally, the EC4 can suitably predict the cross-sectional resistances of circular CFDST short columns with an acceptable deviation.

4.5.2. Proposed formula

From the above survey, the existing strength prediction models have relatively large deviations. Accordingly, based on the model proposed by Yan and Zhao [26], a modified model was suggested to evaluate the cross-sectional resistances of CFDST columns with an extensive parameters, where a reduction factor reflecting the effective use of concrete strength was introduced. The proposed model can be expressed by:

$$N_{u,pro.} = A_c \eta_r f_c (1+\eta_c) + A_{so} f_{syo} + A_{si} f_{syi} \tag{4.11}$$

$$\eta_c = 1.21 \frac{\eta}{\eta_r} \tag{4.12}$$

$$\eta = (1-\chi^2) \frac{2t_o}{D_o - 2t_o} \frac{f_{syo}}{f_c} \tag{4.13}$$

where η_c stands for the enhancing factor of concrete; η_r represents the reduction factor of concrete strength; η denotes the confinement coefficient.

Based on the conducted and collected test data, comparison between the test strengths and the predicted strengths by the proposed model is shown Table 4.7 and Table 4.10. From Table 4.7 and Table 10, it can be seen that a high prediction performance is achieved for the proposed model. This result indicates that the proposed model achieves better strength predictions than the existing design models.

4.6. Conclusions

A comprehensive experimental and numerical investigation on axially loaded circular CFDST columns with HSC and UHSC has been carried out. Based on the scope of the current study, the following conclusions are drawn:

1. The outer and inner tubes of the CFDST columns buckle outward and inward at near the mid-height, respectively. The CFDST columns tend to the brittleness failure with the increase in the concrete strength.

2. As the concrete strength increases, the cross-sectional resistances of the CFDST columns increase linearly. With the increase of the wall thickness and yield stress of the outer tube, the cross-sectional resistances of the CFDST columns increase, whereas they decrease with the increase in the hollow ratio.

3. The FE models are developed and verified against the conducted experimental results. It can be found that established FE models can effectively predict the axial compression response and failure modes of the studied CFDST columns with a reasonable accuracy.

4. Based on the numerical analysis, it can be found that the concrete strength, hollow ratio, and yield stress and diameter-to-thickness ratio of the outer steel tube significantly affect the initial stiffness, ductility, and ultimate strengths of the CFDST columns, while the yield stress and diameter-to-thickness ratio of the inner steel tube exhibit insignificant effect.

5. A novel strength prediction model is suggested to evaluate the cross-sectional resistances of CFDST columns, and a higher prediction performance is achieved for the proposed model than the existing design models.

References

[1] Y.G. Zhao, X.F. Yan, S.Q. Lin, Compressive strength of axially loaded circular hollow centrifugal concrete-filled steel tubular short columns, Eng. Struct. 201 (2019) 109828.

[2] L.H. Han, W. Li, R. Bjorhovde, Developments and advanced applications of concrete-filled steel tubular (CFST) structures: members, J. Constr. Steel Res. 100 (2014) 211–228.

[3] S.Q. Lin, Y.G. Zhao, L.S. He, Stress paths of confined concrete in axially loaded circular concrete-filled steel tube stub columns, Eng. Struct. 173 (2018) 1019–1028.

[4] J. F. Yang, X.F. Yan, P.P. Hu, G.P. Zhang, Z.H. Xi, Study on the bending performance of cantilever concrete-filled circular steel tubular long columns, J. Xi'an Univ. Arch. Tech. (Natural Science Edition) 48(5) (2016) 654–660.

[5] X.F. Yan, Y.G. Zhao, Experimental and numerical studies of circular sandwiched concrete axially loaded CFDST short columns, Eng. Struct. 230 (2021) 111617.

[6] F.Y. Wang, B. Young, G. Leroy, CFDST sections with square stainless steel outer tubes under axial compression: Experimental investigation, numerical modelling and design, Eng. Struct. 207 (2020) 110189.

[7] M.F. Hassanein, O.F. Kharoob, Compressive strength of circular concrete-filled double skin tubular short columns, Thin-Walled Struct. 77 (2014) 165–173.

[8] P. Montague, A simple composite construction for cylindrical shells subjected to external pressure, J. Mech. Eng. Sci 17(2) (1975) 105–113.

[9] M. Elchalakani, X.L. Zhao, R.H. Grzebieta, Tests on concrete filled double-skin (CHS outer and SHS inner) composite short columns under axial compression, Thin-Walled Struct. 40(5) (2002) 415–441.

[10] W. Li, Q.X. Ren, L.H. Han, X.L. Zhao, Behaviour of tapered concrete-filled double skin steel tubular (CFDST) stub columns, Thin-Walled Struct. 57 (2012) 37–48.

[11] W. Li, Y.X. Cai, Performance of CFDST stub columns using high-strength steel subjected to axial compression, Thin-Walled Struct. 141 (2019) 411–422.

[12] F.Y. Wang, B. Young, G. Leroy, Compressive testing and numerical modelling of concrete-filled double skin CHS with austenitic stainless steel outer tubes, Thin-Walled Struct. 141 (2019) 345–359.

[13] W.Q. Wang, C.Q. Wu, J. Li, Z.X. Liu, X.D. Zhi, Lateral impact behavior of double-skin steel

tubular (DST) members with ultra-high performance fiber-reinforced concrete (UHPFRC), Thin-Walled Struct. 144 (2019) 106351.

[14] J.Y.R. Liew, M.X. Xiong, D.X. Xiong, Design of concrete filled tubular beam-columns with high strength steel and concrete, Struct. 8 (2016) 213-226.

[15] S. Cao, C.Q. Wu, W.Q. Wang, Behavior of FRP confined UHPFRC-filled steel tube columns under axial compressive loading, J. Build. Eng. 32 (2020) 101511.

[16] EN 1992-1-1. Eurocode 2: Design of concrete structures. Part 1.1: general rules and rules for buildings. Brussels: European Committee for Standardization (CEN); 2004.

[17] W.Q. Wang, C.Q. Wu, Z.X. Liu, Compressive behavior of hybrid double-skin tubular columns with ultra-high performance fiber-reinforced concrete (UHPFRC), Eng. Struct. 180 (2019) 419-441.

[18] W.Q. Wang, C.Q. Wu, Z.X. Liu, K.X. An, J.J. Zeng, Experimental investigation of the hybrid FRP-UHPC-steel double-skin tubular columns under lateral impact loading, J. Compos. Constr. 24(5) (2020) 04020041.

[19] S. Wei, S.T. Mau, C. Vipulanandan, S.K. Mantrala, Performance of new sandwich tube under axial loading: Experiment, J. Struct. Eng. 121(12) (1995) 1806–1814.

[20] X.L. Zhao, R.H. Grzebieta, M. Elchalakani, Tests of concrete-filled double-skin CHS composite stub columns, Steel Compos. Struct. 2(2) (2002) 129–146.

[21] X.L. Zhao, L.W. Tong, X.Y. Wang, CFDST stub columns subjected to large deformation axial loading, Eng. Struct. 32 (2010) 692-703.

[22] T. Ekmekyapar, H.G. Hasan, The influence of the inner steel tube on the compression behavior of the concrete filled double skin steel tube (CFDST) columns, Mar. Struct. 66 (2019) 197–212.

[23] T. Ekmekyapar, O.H. Alwan, H.G. Hasan, B.A. Shehab, B.J.M. Al-Eliwi, Comparison of classical, double skin and double section CFST stub columns: Experiments and design formulations, J. Constr. Steel Res. 155 (2019) 192-204.

[24] EN 1994-1-1. Eurocode 4: Design of composite steel and concrete structures. Part 1.1: general rules and rules for buildings. Brussels: European Committee for Standardization (CEN); 2004.

[25] ANSI/AISC 360-16. Specification for Structural Steel Buildings. American Institute of Steel Construction, Chicago, USA, 2016.

[26] X.F. Yan, Y.G. Zhao, Compressive strength of axially loaded circular concrete-filled double-skin steel tubular short columns, J. Constr. Steel Res. 170 (2020) 106114.

[27] JIS G 3444-2015. Carbon steel tubes for general structure. Japanese Standards Association, 2015 [In Japanese]

[28] ACI-318. Building code requirements for reinforced concrete. Michigan, USA, Farmington Hills; 2014.

[29] ABAQUS Standard User's Manual. The Abaqus Software is a product of Dassault Systemes Simulia Corp. Providence, RI, USA Dassault Systemes, Version 6.8, USA, 2008.

[30] L.H. Han, G.H. Yao, Z. Tao, Performance of concrete-filled thin-walled steel tubes under pure torsion, Thin-Walled Struct. 45 (2007) 24–36.

[31] H. Huang, L.H. Han, Z. Tao, X.L. Zhao, Analytical behavior of concrete-filled double skin steel tubular (CFDST)stub columns, J. Constr. Steel Res. 66(3) (2010) 542–555.

[32]F.C. Wang, L.H. Han, W. Li, Analytical behavior of CFDST stub columns with external stainless steel tubes under axial compression, Thin-Walled Struct. 127 (2018) 756–768.

[33]M.F. Hassanein, O.F. Kharoob, Q.Q. Liang, Circular concrete-filled double skin tubular short columns with external stainless steel tubes under axial compression, Thin-Walled Struct. 73 (2013) 252–263.

[34]L.H. Han, Z. Tao, H. Huang, X.L. Zhao, Concrete-filled double-skin (SHS outer and CHS inner) steel tubular beam-columns, Thin-Walled Struct. 42(9) (2004) 1329–1355.

[35]K. Uenaka, H. Kitoh, K. Sonoda, Concrete filled double skin circular stub columns under compression, Thin-Walled Struct. 48 (2010) 19–24.

[36]Q.Q. Liang, Nonlinear analysis of circular double-skin concrete-filled steel tubular columns under axial compression, Eng. Struct. 131 (2017) 639–650.

[37]T.M. Chan, L. Gardner, Compressive resistance of hot-rolled elliptical hollow sections, Eng. Struct. 30 (2) (2008) 522–532.

[38]BS 5950-1, Structural Use of Steelwork in Building- Part 1: Code of Practice for Design—Rolled and Welded Sections, The Standards Policy and Strategy Committee, 2000.

[39]Z. Tao, Z.B. Wang, Q. Yu, Finite element modelling of concrete-filled steel stub columns under axial compression, J. Constr. Steel Res. 89 (2013) 121–131.

[40]Z. Tao, L.H. Han, X.L. Zhao, Behavior of concrete-filled double skin (CHS inner and CHS outer) steel tubular stub columns and beam columns, J. Constr. Steel Res. 60(8) (2004) 1129–1158.

[41]M.L. Lin, K.C. Tsai, Behavior of double-skinned composite steel tubular columns subjected to combined axial and flexural loads. In: Proceedings of the first international conference on steel and composite structures; (2001) 1145–1152.

[42]J.S. Fan, M.N. Baig, J.G. Nie, Test and analysis on double-skin concrete filled tubular columns. In: Shen ZY, Chen YY, Zhao XZ, editors. Tubular structures XII - proceedings of the 12th international symposium on tubular structures, ISTS 2009, Shanghai, China. 2009. p. 407–411.

[43]U.M. Sulthana, S.A. Jayachandran, Concrete confinement effect in circular concrete sandwiched double steel tubular stub-columns, Int. J. Steel Struct. 20 (2020) 1364–1377.

[44]W. Li, D. Wang, L.H. Han, Behaviour of grout-filled double skin steel tubes under compression and bending: Experiments, Thin-Walled Struct. 116 (2017) 307–319.

[45]M.A. Rashid, M.A. Mansur, P. Paramasivam, Correlations between mechanical properties of high-strength concrete, J. Mater. Civil Eng. ASCE 14 (2002) 230–238.

[46]Z.H. Lu, Y.G. Zhao, Suggested empirical models for the axial capacity of circular CFT stub columns, J. Constr. Steel Res. 66 (2010) 850–862.

CHAPTER 5. FIBER-BEAM ELEMENT MODEL FOR CIRCULAR ENTIRE-SECTION AXIALLY LOADED CFDST SHORT COLUMNS

5.1. Introduction

Concrete-filled steel tubular (CFST) columns are widely utilized as various modern building structures, especially in high-rise buildings, owing to their excellent structural performance, which includes large energy-absorption capacity, high ductility and stiffness [1-2]. As a member of CFST column family, recently, an innovative composite structure referred to as concrete-filled double-skin steel tubular (CFDST) columns with concrete infilled between the two centric tubes has captured the interests of researchers [3-4]. CFDST columns not only share the excellent high strength and ductility performance of conventional CFST columns, but also reduce its weight and relies on its own internal voids to supply dry space for engineering installation.

So far, several experimental and numerical investigations on axially loaded CFDST columns have been conducted by researchers. Zhao et al. [5-6], Han et al. [7], Tao et al. [8-9], Uenaka et al. [10], Essopjee and Dundu [11], Ekmekyapar and Hasan [12], and Wang et al. [13] experimentally investigated the effects of different sectional dimensions and combinations on the strength and ductility of CFDST columns in bending or compression, and developed the corresponding strength prediction models. Huang et al. [15], Wang et al. [16], Li and Cai [14], Hu and Su [17], Hassanein and Kharoob [18], Liang [19], and Hassanein et al. [20] numerically investigated the effects of the key variables on the strength and ductility of circular CFDST columns concentrically compressed by using the ABAQUS software [21].

Generally, in order to fully comprehend the structural performance of CFDST columns, two investigation methods may be utilized, namely experimental test [3,13] and numerical analysis [17,19]. In some cases, experimental method is restricted owing to expenses and capability of test equipment. Therefore, numerical analysis (includes finite element (FE) simulation and fiber element (FBE) analysis) is considered as an alternative and efficient method if the appropriate material models can be obtained. Compared with the FE simulation, the FBE analysis can accurately and effectively simulate the axial responses of steel-concrete composite columns owing to their simplicity in simulation and high computational efficiency [8]. Hence, in the recent research works, the FBE analysis is more and more favored and utilized by researchers [8,19].

One important issue on circular CFDST columns is the axial load-deflection relationship, to efficiently obtain which, some fiber-beam element (FBE) models were empirically developed based on the individual experimental database [8,19]. The accuracy of a FBE model depends mainly on the suitable input material models of the steel and confined concrete. It has been shown that the compressive strength model of confined concrete acts a vital role in the constitution of stress-strain relationship of confined concrete [19]. However, existing compressive strength models of confined concrete in circular CFDST columns were developed and verified based on the limited experimental data (i.e., low concrete and steel strengths, etc..) [8,19]. As mentioned in Chapter 4, an effective concrete strength should be employed rather than directly using the concrete strength obtained from material property tests. However, such effect has not been considered in the existing empirical models. Therefore, the reasonability of these models for the CFDST columns with a wide range of column parameters, especially HSC or UHSC, is doubtful. For well modelling the load-deflection

relationships of CFDST columns under axial compression, a general compressive strength model of confined concrete should be developed and incorporated in the FBE model.

The purpose of this study is to develop an accurate FBE model for the nonlinear analysis of circular CFDST short columns under central compression. The composition of this paper is summarized as below: In Section 2, a new FBE model is proposed for the nonlinear analysis of the studied CFDST columns, and the accurate stress-strain relationships of steel and confined concrete are presented. A novel strength degradation coefficient for quantitatively determining the post-peak characteristics of confined concrete in the studied CFDST columns is derived on the basis of experimental results and consolidated in the FBE model; In Section 3, the proposed FBE model is validated through comparisons with the axial ultimate loads and axial load vs. strain curves of the test results; Finally, Section 4 draws the conclusions.

5.2. Fiber-beam element (FBE) model

5.2.1. General

In order to fully comprehend the behavior of the studied CFDST columns under central compression, a FBE model incorporating the size and effective concrete strength is proposed for nonlinear analysis of the kind of columns. This method is an accurate and computationally efficient numerical technique for analyzing the behavior of composite columns [8,19]. The method discretizes the cross-section of the studied CFDST column into fine fiber elements, as illustrated in Fig.5.1. Each fiber element can be specified different material properties such as steel or concrete. Utilizing the material uniaxial stress-strain relationships of concrete and steel presented in Section 2.2 and 2.3, the fiber stresses of cross-section are determined from corresponding fiber strains. The axial load of the column cross-section is calculated by means of the stress resultant [19]. The computer flow chart for calculating axial load vs axial strain curves of the studied CFDAT columns is illustrated in Fig.5.2. Currently, the following assumptions have been adopted in the FBE modeling for examining the compressive behavior of the studied CFDST columns: (1) the bond at the interface between the sandwich concrete and steel tubes is perfect; (2) the strain of fibers is distributed homogeneously throughout the entire cross-section; (3) the effects of creep and shrinkage of the concrete are not considered; (4) steel fracture is not accounted for because it happens at very late stage in the load history; and (5) the cross-section always keeps a plane during deformation.

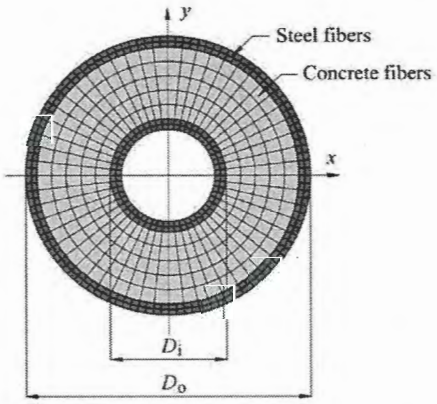

Fig.5.1 Effect of compressive strength of concrete

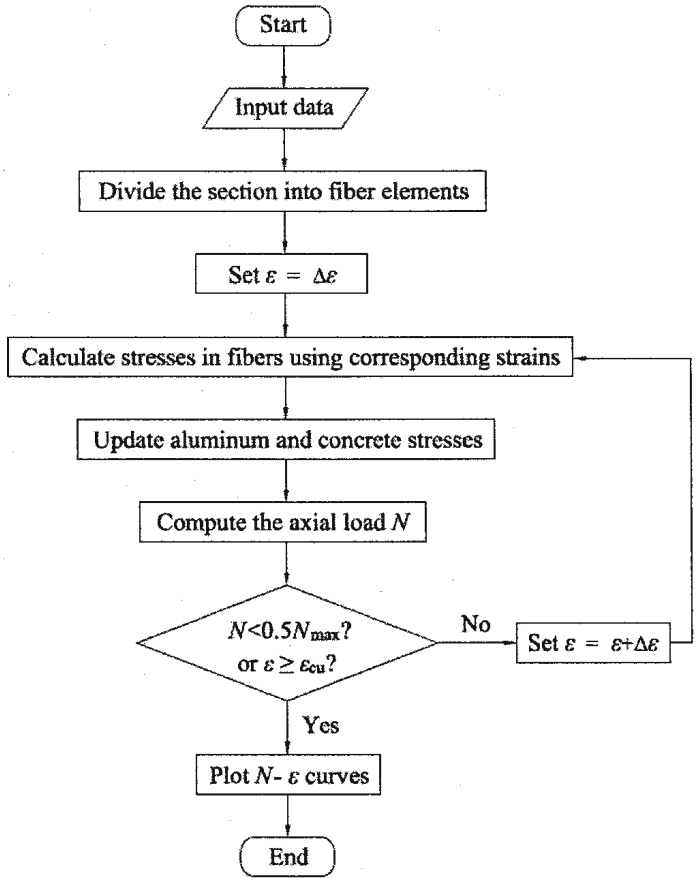

Fig.5.2 Computer flow chart for calculating axial load vs axial strain curves

In this method, the axial load imposed on the cross-section of the studied CFDST columns is obtained by means of stress resultant as follows:

$$N = \sum_{i=1}^{n_{so}} \sigma_{so,i} A_{so,i} + \sum_{j=1}^{n_{sc}} \sigma_{sc,j} A_{sc,j} + \sum_{k=1}^{n_{si}} \sigma_{si,k} A_{si,k} \tag{5.1}$$

where N stands for the axial load imposed on the cross-section of the CFDAT column; $\sigma_{so,i}$ represents the stress of fiber element of outer steel tube; $\sigma_{sc,j}$ represents the stress of fiber element of sandwiched concrete; $\sigma_{si,k}$ represents the stress of fiber element of inner steel tube; $A_{so,i}$ represents the area of fiber element of outer steel tube; $A_{sc,j}$ represents the area of fiber element of sandwiched concrete; $A_{si,k}$ represents the area of fiber element of inner steel tube; n_{so}, n_{sc} and n_{si} are the total number of fiber elements of outer and inner steel tubes and infilled concrete, respectively.

5.2.2. Material model for confined concrete

In general, two measures have been applied to simulate the behavior of concrete, namely unconfined and confined concrete models [20-25]. However, the interest of this paper is confined concrete model, which is widely applied in numerical analysis [17-20]. In the present paper, in order to simulate the axial responses of confined concrete in the studied CFDST columns under central compression, the idealized stress-strain relationships are illustrated in Fig.5.3. From this figure, it can

be found that the stress-strain curve of the confined concrete comprises of the two parts: the rising segment OA and declining segment AB.

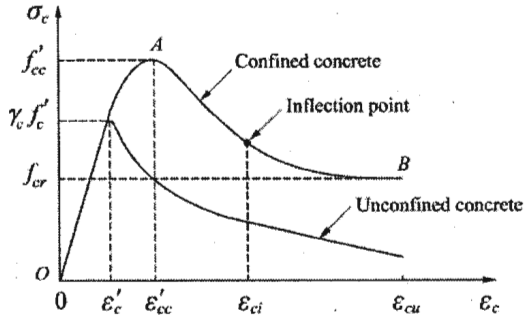

Fig.5.3 Stress-strain curves for confined and unconfined concrete

5.2.2.1. The rising segment *OA*

Various confined concrete models [17,19,24] were used to determine the stress-strain function of the rising segment *OA* ($0 \le \varepsilon_c \le \varepsilon'_{cc}$), in this paper, the equation developed by Mander et al. [26] is employed to trace the stress-strain behavior of the rising segment *OA*, as:

$$\sigma_c = \frac{f'_{cc}\lambda(\varepsilon_c/\varepsilon'_{cc})}{(\varepsilon_c/\varepsilon'_{cc})^{\lambda} + \lambda - 1} \tag{5.2}$$

in which σ_c denotes the axial compressive stress of concrete and its corresponding strain is ε_c; f'_{cc} is the compressive strength of confined concrete when the axial strain is up to ε'_{cc}; λ symbolizes the material constant which characterizes the curvature and slope of the rising segment *OA*, and its expression is as:

$$\lambda = \frac{E_c\varepsilon'_{cc}}{E_c\varepsilon'_{cc} - f'_{cc}} \tag{5.3}$$

where E_c stands for the Young's modulus of the infilled concrete, which is defined by ACI 318-14 [27] as:

$$E_c = 3320\sqrt{\gamma_c f_c} + 6900 \quad (\text{MPa}) \tag{5.4}$$

It should be noted that the effective concrete strength $\gamma_c f_c$ is applied in the present paper. Thereinto, γ_c represents the reduction factor of infilled concrete given by Liang [19], in which the effects of the column size, load rates and concrete quality were accounted for, and its expression is as follows:

$$\gamma_c = 1.85t_c^{-0.135} \quad (0.85 \le \gamma_c \le 1.0) \tag{5.5}$$

in which t_c stands for the wall thickness of concrete filled between external and internal steel tubes, and it is computed by $t_c = D_o/2 - t_o - D_i/2$; where D_o and D_i are the diameters of external and internal steel tubes, respectively, and t_o is the wall thickness of external steel tube.

On the other hand, in order to calculate the values of the compressive strength f'_{cc} and strain ε'_{cc} in Eqs. (5.2) and (5.3), the equations proposed by Mander et al. [26] and Richart et al. [28] are modified and expressed as below:

$$f'_{cc}=\left(1+\frac{k_1 f_{rp}}{\gamma_c \eta_r f_c}\right)\gamma_c \eta_r f_c \tag{5.6}$$

$$\varepsilon'_{cc}=\varepsilon'_c+\frac{k_2 f_{rp}\varepsilon'_c}{\gamma_c \eta_r f_c} \tag{5.7}$$

where the value of k ($k_1 = k$ and $k_2 = 5k$), which ranges from 2.6 to 7 for ordinary and high strength concrete, has been experimentally determined [29]. Recent researches have shown that k is a comprehensive factor and depends on the stress path of confined concrete [1]. In this paper, the values of k_1 and k_2 adopted 4.1 and 20.5, respectively [28]. η_r represents the reduction factor of concrete strength reflecting the effective use of concrete strength, as given in Eq. (4.7). ε'_c is the axial strain when the stress σ_c reaches the concrete strength f_c, herein, it is computed by the formula defined by De Nicolo et al. [30] as below:

$$\varepsilon'_c=0.00076+\sqrt{(0.626\gamma_c f_c-4.33)\times 10^{-7}} \tag{5.8}$$

In addition, the lateral confining pressure model holds the post of important role in simulating the compressive behavior of sandwich concrete in the studied CFDST columns under central compression. In this paper, the previous experimental results [3,8,10,12,14,31-38] and conducted test results given in Chapter 4 were collected and formed a database. Generally, the limitations of all the experimental data about the studied CFDST columns are described as follows:

(1) The hollow ratio χ (D_i/D_o) varies from 0.18 to 0.89;

(2) The unconfined concrete strength (f_c) ranges from 18.7 MPa to 141.0 MPa;

(3) The diameter-to-thickness ratios of the outer and inner steel tubes range from 18.7 to 176.7 and 10.5 to 146.0, respectively;

(4) The yield strengths of the outer and inner steel tubes range from 221.0 MPa to 618.0 MPa and 216.0 MPa to 520.0 MPa, respectively.

From the above summary, it can be found that the current test database not only consists of a wide range of concrete strengths, but also a wide-scope of yield stresses and diameter-to-thickness ratios of outer and inner steel tubes as well as hollow ratios. Based on the regression analysis of the above database, the confining pressure f_{rp} on the sandwich concrete in the studied CFDST columns can be expressed by:

$$f_{rp}=19.6\times\left(\frac{t_o}{D_o}\right)\times\left(\frac{f_{syo}}{\gamma_c \eta_r f_c}\right)+0.08\eta^2-0.07\chi^2+0.4 \tag{5.9}$$

5.2.2.2. The proposed model for the declining segment *AB*

From the investigations described in the last section, in order to accurately simulate the post-peak behavior of confined concrete in the studied CFDAT columns, one need to incorporate the concrete strength f_c into the strength degradation factor β_c, which is better to express the relationship as curve instead of straight lines. For this object, a novel model for the declining segment AB is proposed as:

$$\sigma_c=f'_{cc}\left(1-(1-\beta_c)\frac{(\varepsilon_c-\varepsilon'_{cc})}{\varepsilon_c+\varepsilon_{ct}-2\varepsilon'_{cc}}\right)\ (\varepsilon_c\geq\varepsilon'_{cc}) \tag{5.10}$$

in which the compressive stress f'_{cc} and its corresponding strain ε'_{cc} are determined by Eqs. (5.6) and (5.7); the strength degradation coefficient β_c determining the post-peak behavior of the confined concrete is derived based on the regression analysis of the collected test results, and its expression is as follows:

$$\beta_c = 2.85\times\left(\frac{t_o}{D_o}\right)\times\left(\frac{f_{syo}}{\gamma_c\eta_r f_c}\right)+0.03\eta^2-0.08\chi^2+0.01\times\left(\frac{t_i}{D_i}\right)\times f_{syi}-0.11 \tag{5.11}$$

Additionally, ε_{ct} depicted in Fig.5.3 is the strain at the turning point, in which the curvature of the descending segment of the stress-strain curves varies from negative to positive. Utilizing the built database, the regression analysis was conducted and the determination of ε_{ct} is expressed as a function of the peak strain ε'_{cc}, unconfined concrete strength f_c, strength degradation coefficient β_c, size effect γ_c, and the reduction factor of concrete strength η_r, as shown in the following equation:

$$\varepsilon_{ct} = 3.8\beta_c\varepsilon'_c\left(\gamma_c\eta_r f_c\right)^{-0.12}+10\left(1-\beta_c\right)\varepsilon'_{cc}\left(\gamma_c\eta_r f_c\right)^{-0.35} \tag{5.12}$$

5.2.3. Material model for steel

The internal and external steel tubes in a CFDST column with circular section are under biaxial stresses resulting from the longitudinal compression and either hoop compression or tension which lowers the yield stress of the steel tubes. To consider this effect, the yield stress is reduced by a factor of 0.9 in the constitutive model for structural steels as shown in Fig.5.4.

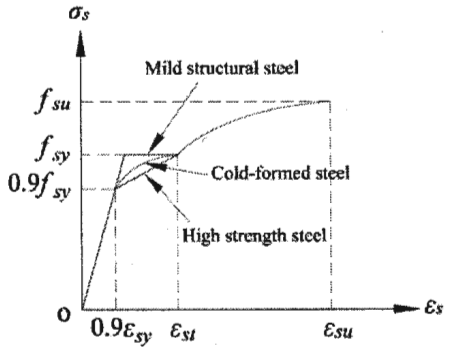

Fig.5.4 Stress-strain curves for structural steels

The parabolic curve in the strain range of $0.9\varepsilon_{sy} < \varepsilon_s \leq \varepsilon_{st}$ applied to cold-formed steels is defined using the expression proposed by Liang [22] as:

$$\sigma_s = f_{sy}\left(\frac{\varepsilon_s-0.9\varepsilon_{sy}}{\varepsilon_{st}-0.9\varepsilon_{sy}}\right)^{\frac{1}{45}} \tag{5.13}$$

where σ_s is the stress in a steel fiber, ε_s is the strain in the steel fiber, f_{sy} is the yield strength of steel, ε_{sy} is the yield strain of steel, ε_{st} is the steel strain at the onset of strain hardening and is taken as 0.005. For the stress-strain relationship of steel in the range of $\varepsilon_{st} < \varepsilon_s \leq \varepsilon_{su}$, the expressions given by Mander et al. [26] are employed as:

$$\sigma_s = f_{su}-\left(\frac{\varepsilon_{su}-\varepsilon_s}{\varepsilon_{su}-\varepsilon_{st}}\right)^n\left(f_{su}-f_{sy}\right) \tag{5.14}$$

$$n = E_{st}\left(\frac{\varepsilon_{su} - \varepsilon_{st}}{f_{su} - f_{sy}}\right) \tag{5.15}$$

where f_{su} is the steel tensile strength, ε_{su} is the strain at f_{su}, E_{st} is the steel modulus at the onset of strain hardening and is taken as $0.2E_s$.

5.3. Verification of the proposed FBE model

The proposed FBE model incorporating the accurate material models is verified through comparisons with the ultimate loads and axial load vs strain curves of the selected test results from Tao et al. [8], Ekmekyapar and Hasan [12], and Chapter 4, which covers a wide range of column parameters, as shown in Table 4.1 and Table 4.8.

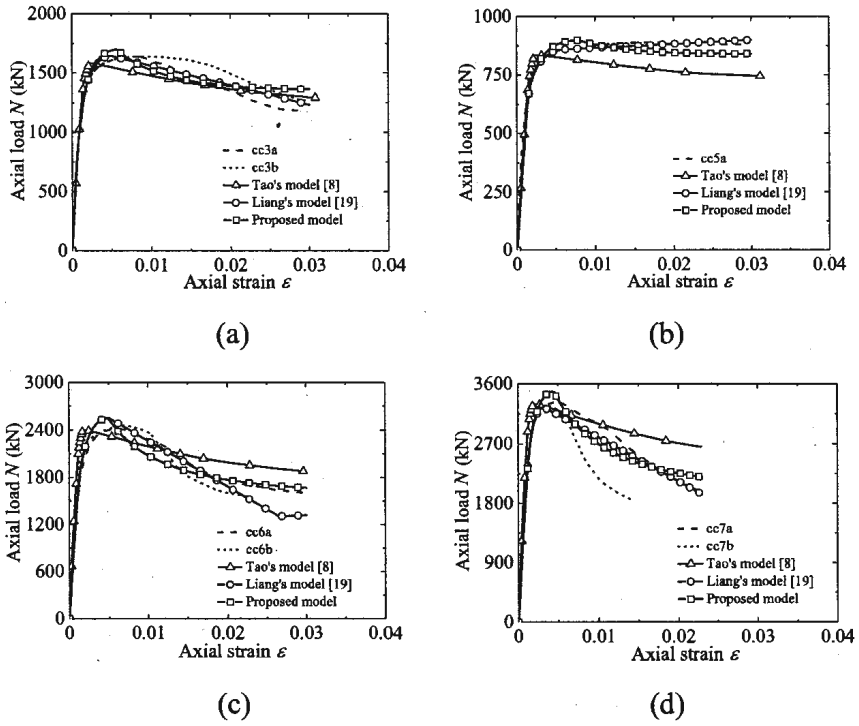

Fig.5.5 Predicted N-ε curves versus test results (NSC-f_c = 39.7 MPa)

Comparisons of the axial load (N) vs strain (ε) curves from the experimental results with those simulated by the proposed FBE model, Tao et al.'s model [8], and Liang's model [19] are depicted in Fig.5.5 and Fig.5.6. From Fig.5.5, it can be found that, the predictions of the proposed FBE model and Liang's model are well agreement with the axial load-strain curves of the tested CFDST columns with NSC. Although Tao et al.'s model is accurate in the pre-peak stage, there is a large deviation in the post peak stage. Generally, the proposed FBE model and Liang's model can effectively predict the axial load vs. strain curves of the columns with NSC. From Fig.5.6, it can be seen that the proposed FBE model can predict the axial load vs. strain curves of the columns with HSC or UHSC more accurately than Tao et al.'s model and Liang's model. A slight discrepancy is found in the prediction of the initial stiffness of the proposed FBE model. This discrepancy may have been due to the fact that the real f_c values of the concrete infill may also differ from those obtained from the cylindrical material tests due to differences in the curing methods used in both specimens.

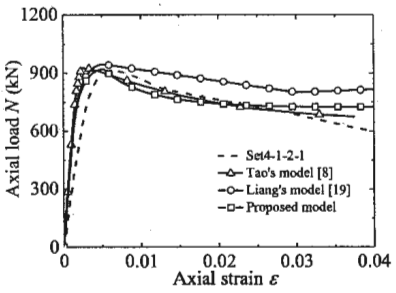

(a) (f_c = 64.6 MPa)

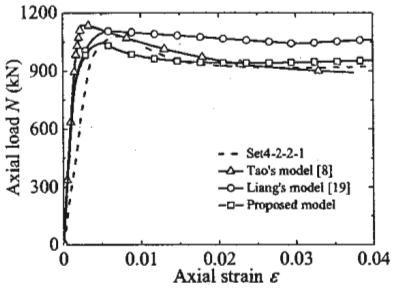

(b) (f_c = 64.6 MPa)

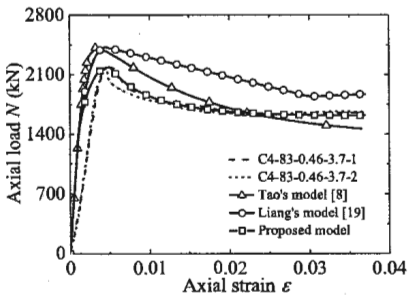

(c) (f_c = 90.7 MPa)

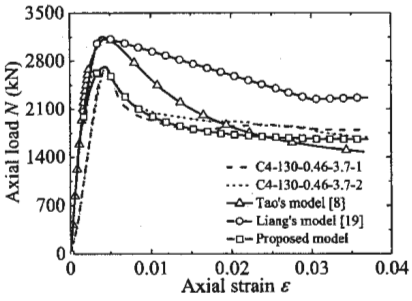

(d) (f_c = 141.0 MPa)

Fig.5.6 Predicted N-ε curves versus test results (HSC and UHSC)

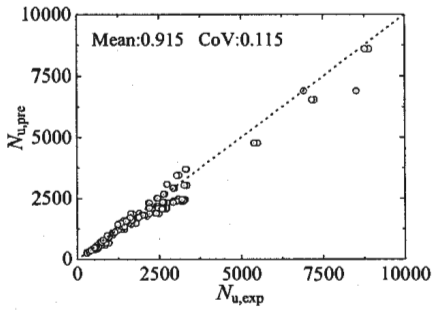

(a) Tao et al.'s model

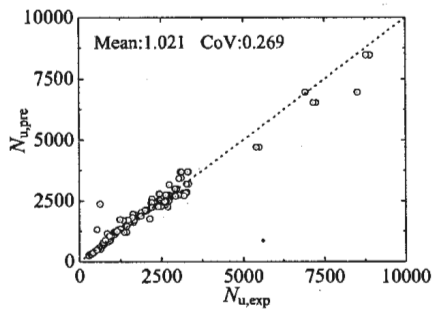

(b) Liang's model

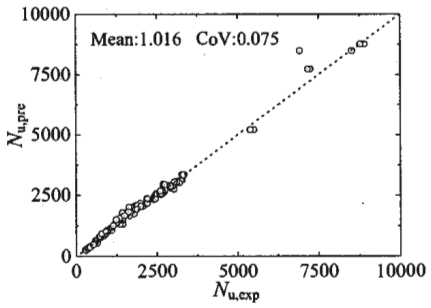

(c) Proposed model

Fig.5.7 Comparison of predicted-to-test strengths

Utilizing the experimental data listed in Table 4.1 and Table 4.8 in Chapter 4, comparisons of the test strengths with the predictions by the proposed FBE model, Tao et al.'s model and Liang's model are illustrated in Fig.5.7. From Fig.5.7, it can be observed that the mean of the predictions of the proposed FBE model to test strengths is 1.016, which is closer to the unity than other two models.

Additionally, the coefficient of variation (CoV) is 0.075 for the proposed FBE model, which is smaller than those of Tao et al.'s model and Liang's model. This confirms that, compared with other two methods, the proposed FBE model can estimate the ultimate axial strengths of the studied CFDST columns more accurately.

Overall, the proposed FBE model can accurately predict the compressive behaviour of the studied CFDST columns with a wide range of column parameters.

5.4. Conclusions

This paper proposes a comprehensive FBE model for the nonlinear analysis of circular CFDST short columns under central compression. Based on the scope of the current study, the following conclusions could be found:

1. The effect of concrete strength on its effective utilization rate is not considered in Liang's model and Tao et al.'s model, thus a large deviation is found when they predict the compressive behavior CFDST columns with HSC or UHSC.

2. The proposed FBE model can predict the compressive behaviour of circular CFDST short columns made with a wide-range of column parameters more accurately than the existing models.

References

[1] Y.G. Zhao, X.F. Yan, S.Q. Lin, Compressive strength of axially loaded circular hollow centrifugal concrete-filled steel tubular short columns, Eng. Struct. 201 (2019) 109828.

[2] J. F. Yang, X.F. Yan, P.P. Hu, G.P. Zhang, Z.H. Xi, Study on the bending performance of cantilever concrete-filled circular steel tubular long columns, J. Xi'an Univ. Arch. Tech. (Natural Science Edition) 48(5) (2016) 654–660.

[3] X.F. Yan, Y.G. Zhao, Compressive strength of axially loaded circular concrete-filled double-skin steel tubular short columns, J. Constr. Steel Res. 170 (2020) 106114.

[4] X.F. Yan, Y.G. Zhao, Experimental and numerical studies of circular sandwiched concrete axially loaded CFDST short columns, Eng. Struct. 230 (2021) 111617.

[5] M. Elchalakani, X.L. Zhao, R. Grzebieta, Tests on concrete filled double-skin (CHS outer and SHS inner) composite short columns under axial compression, Thin-Walled Struct. 40(5) (2002) 415–441.

[6] X.L. Zhao, R. Grzebieta, Strength and ductility of concrete filled double skin (SHS inner and SHS outer) tubes, Thin-Walled Struct. 40 (2002) 199–213.

[7] L.H. Han, Z. Tao, H. Huang, X.L. Zhao, Concrete-filled double skin (SHS outer and CHS inner) steel tubular beam-columns, Thin-Walled Struct. 42(9) (2004) 1329-1355.

[8] Z. Tao, L.H. Han, X.L. Zhao, Behavior of concrete-filled double skin (CHS inner and CHS outer) steel tubular stub columns and beam columns, J. Constr. Steel Res. 60(8) (2004) 1129–1158.

[9] Z. Tao, L.H. Han, Behavior of concrete-filled double skin rectangular steel tubular beam columns, J. Constr. Steel Res. 62(7) (2006) 631–646.

[10] K. Uenaka, H. Kitoh, K Sonoda, Concrete filled double skin circular stub columns under compression, Thin-Walled Struct. 48 (2010) 19-24.

[11] Y. Essopjee, M. Dundu, Performance of concrete-filled double skin circular tubes in compression,

Compos. Struct. 133 (2015) 1276–1283.

[12]T. Ekmekyapar, H.G. Hasan, The influence of the inner steel tube on the compression behavior of the concrete filled double skin steel tube (CFDST) columns, Mar. Struct. 66 (2019) 197–212.

[13]F.Y. Wang, B. Yong, L. Gardner, Compressive testing and numerical modelling of concrete-filled double skin CHS with austenitic stainless steel outer tubes, Thin-Walled Struct. 141 (2019) 345–359.

[14]W. Li, Y.X. Cai, Performance of CFDST stub columns using high-strength steel subjected to axial compression, Thin-Walled Struct. 141 (2019) 411–422.

[15]H. Huang, L.H. Han, Z. Tao, X.L. Zhao, Analytical behavior of concrete-filled double skin steel tubular (CFDST)stub columns, J. Constr. Steel Res. 66(3) (2010) 542–555.

[16]F.C. Wang, L.H. Han, W. Li, Analytical behavior of CFDST stub columns with external stainless steel tubes under axial compression, Thin-Walled Struct. 127 (2018) 756–768.

[17]H.T. Hu, F.C. Su, Nonlinear analysis of short concrete-filled double skin tube columns subjected to axial compressive forces, Mar. Struct. 24 (2011) 319–337.

[18]M.F. Hassanein, O.F. Kharoob, Compressive strength of circular concrete-filled double skin tubular short columns, Thin-Walled Struct. 77 (2014) 165–173.

[19]Q.Q. Liang, Nonlinear analysis of circular double-skin concrete-filled steel tubular columns under axial compression, Eng. Struct. 131(15) (2017) 639–650.

[20]M.F. Hassanein, O.F. Kharoob, Q.Q. Liang, Circular concrete-filled double skin tubular short columns with external stainless steel tubes under axial compression, Thin-Walled Struct. 73 (2013) 252–263.

[21]ABAQUS Standard User's Manual. The Abaqus Software is a product of Dassault Systemes Simulia Corp. Providence, RI, USA Dassault Systemes, Version 6.8, USA, 2008.

[22]Q.Q. Liang, S. Fragomeni. Nonlinear analysis of circular concrete-filled steel tubular short columns under axial loading. J. Constr. Steel Res.65 (2009) 2186–2196.

[23]H.T. Hu, C.S. Huang, M.H. Wu, Y.M. Wu, Nonlinear analysis of axially loaded concrete-filled tube columns with confinement effect, J. Struct. Eng. 129(10) (2003) 1322–1329.

[24]Z. Tao, Z.B. Wang, Q Yu, Finite element modelling of concrete-filled steel stub columns under axial compression, J. Constr. Steel Res. 89 (2013) 121–131.

[25]L.H. Han, Concrete Filled Steel Tubular Structures-Theory and Practice, Third. China Science Publishing & Media Ltd., 2016 (In Chinese).

[26]J.B. Mander, M.J.N. Priestley, R. Park, Theoretical stress-strain model for confined concrete, J. Struct. Eng. 114(8) (1988) 1804-1826.

[27]ACI 318-14. Building code requirements for structural concrete and commentary. American Concrete Institute, Farmington Hills, MI; 2014.

[28]F.E. Richart, A. Brandtzaeg, R.L. Brown, A Study of the Failure of Concrete Under Combined Compressive Stresses. University of Illinois at Urbana Champaign, College of Eng. Eng. Exp. Station;1928.

[29]D.P.G. Sugupta, P.A. Mendis, Design of high-strength-concrete filled tube column. In: Proceedings of the fifth East-Asia-Pacific conference on structural engineering and construction. Australia: Griffith University;(1995) 427-432.

[30]B. De Nicolo, L. Pani, E. Pozzo, Strain of concrete at peak compressive stress for a wide range of compressive strengths, Mater. Struct. 27(4) (1994) 206–210.

[31]T. Ekmekyapar, O.H. Alwan, H.G. Hasan, B.A. Shehab, B.J.M. Al-Eliwi, Comparison of classical, double skin and double section CFST stub columns: Experiments and design formulations, J. Constr. Steel Res. 155 (2019) 192-204.

[32]M.L. Lin, K.C. Tsai, Behavior of double-skinned composite steel tubular columns subjected to combined axial and flexural loads. In: Proceedings of the first international conference on steel and composite structures; (2001) 1145–1152.

[33]J.S. Fan, M.N. Baig, J.G. Nie, Test and analysis on double-skin concrete filled tubular columns. In: Shen ZY, Chen YY, Zhao XZ, editors. Tubular structures XII - proceedings of the 12th international symposium on tubular structures, ISTS 2009, Shanghai, China. 2009. p. 407–411.

[34]W. Li, D. Wang, L.H. Han, Behaviour of grout-filled double skin steel tubes under compression and bending: Experiments, Thin-Walled Struct. 116 (2017) 307–319.

[35]U.M. Sulthana, S.A. Jayachandran, Concrete confinement effect in circular concrete sandwiched double steel tubular stub-columns, Int. J. Steel Struct. 20 (2020) 1364–1377.

[36]X.L. Zhao, L.W. Tong, X.Y. Wang, CFDST stub columns subjected to large deformation axial loading, Eng. Struct. 32 (2010) 692-703.

[37]X.L. Zhao, R.H. Grzebieta, M. Elchalakani, Tests of concrete-filled double-skin CHS composite stub columns, Steel Compos. Struct. 2(2) (2002) 129–146.

[38]S. Wei, S.T. Mau, C. Vipulanandan, S.K. Mantrala, Performance of new sandwich tube under axial loading: Experiment, J. Struct. Eng. 121(12) (1995) 1806–1814.

CHAPTER 6. SUMMARIES

In this research, the compressive behaviours of the entire-section and concrete axially loaded circular CFDST short columns are experimentally and numerically investigated. A FBE model incorporating an effective concrete strength is developed for capturing the load-deflection relationships of CFDST columns. The conclusions obtained in the current study will be briefly summarized as follows:

Chapter 2. Compressive behavior of circular sandwiched concrete axially loaded CFDST short columns

1). The concrete strength generates a negligible effect on the failure mode. With the increase of the wall thickness and yield stress of outer steel tube, the failure mode of the specimens gradually changes from diagonal shear failure to axial compression failure.

2). The tested CFDST columns show good ductility performance similar to that of circular STCC columns.

3). The ultimate strength of specimens with C9 outer steel tube is about 20% to 26% than that of ones with C4 outer steel tube. With an increase in the wall thickness of outer steel tube and concrete strength, the ultimate strength of specimens is improved by 32% and 43%, respectively. The ultimate strength of specimens first increases and then decreases with the increase of the hollow ratio. Generally, the concrete strength, wall thickness and yield stress of outer steel tube, and hollow ratio affect significantly the ultimate strength of columns.

4). A material model suggested by Han et al. was adopted in this study to model the behavior of concrete in the concrete axially loaded CFDST columns. It can be found that established FE model can almost replicate the axial compression response and failure modes of the columns.

5). Based on the numerical and test results, a novel formula was suggested to predict the ultimate strength of the studied CFDST columns. Excellent agreement was found between the predicted strengths and numerical and test strengths.

6). The proposed formula can accurately predict the ultimate strength of concrete axially loaded CFDST short columns. By setting the hollow ratio as zero, it can be also applicable for the strength prediction of STCC short column.

Chapter 3. Compressive behaviour of circular entire-section axially loaded CFDST short columns

1). The hollow ratio and yield strength of the external steel tube considerably affected the ultimate axial strengths of circular CFDST short columns. An increase of concrete strength and wall thickness of the external steel tube can effectively improve the compressive strengths of circular CFDST short columns.

2). For the specimens with the hollow ratio of 0 and 0.19, the ultimate strength of the entire-section axially loaded specimens is larger than that of the concrete axially loaded ones, while the opposite result is found for the specimens with the hollow ratio of 0.34 and 0.56. This indicates that the lateral confinement effect of outer and inner steel tubes to sandwiched concrete decreases as the hollow ratio increases.

3). The ultimate strength of the entire-section axially loaded specimens with the hollow ratio of 0.34 is larger than that of the concrete axially loaded ones. The ultimate strength of the entire-section

axially loaded specimens is smaller than that of the concrete axially loaded ones at first, and then larger than that of the concrete axially loaded ones with the increase of the D_o/t_o ratio. This is mainly due to the stronger lateral confinement effect of the specimens with smaller D_o/t_o ratio (thicker wall thickness).

4). The external CSPs of CFDST columns are remarkably affected by the column variables investigated, i.e., χ, f_{syo}, f_c and D_o/t_o ratio, but less effects on the internal CSPs.

5). Similar to CFST columns under different types of loading, the effect indices of CFDST columns with a smaller η are smaller than the unity, which suggests that the compressive strength of confined concrete in the column with a smaller η is CSP-dependent.

6). The effect indices of CFDST column are generally less than those of CFST columns, which implies that the confinement effects of CFDST columns are weaker than those of CFST columns. Note that when the η is smaller than about 0.2, the effect indices of CFDST columns are nearly the same as those of CFST columns, which implies that the confinement effects for both are almost identical.

7). As the η enhances, the effect indices of CFST and CFDST columns become the unity in turn, which suggests that the confinement effects for both are identical. In other words, the compressive strength of confined concrete in the column with a larger η is CSP-independent.

8). A CSP-based compressive strength model of axially compressed circular CFDST short columns is proposed, and comparisons with existing models against the collected test data indicate a higher degree of accuracy and consistency of the predictions for the proposed model.

Chapter 4. Compressive strength of circular entire-section axially loaded CFDST short columns

1). The outer and inner tubes of the CFDST columns buckle outward and inward at near the mid-height, respectively. The CFDST columns tend to the brittleness failure with the increase in the concrete strength.

2). As the concrete strength increases, the cross-sectional resistances of the CFDST columns increase linearly. With the increase of the wall thickness and yield stress of the outer tube, the cross-sectional resistances of the CFDST columns increase, whereas they decrease with the increase in the hollow ratio.

3). The FE models are developed and verified against the conducted experimental results. It can be found that established FE models can effectively predict the axial compression response and failure modes of the studied CFDST columns with a reasonable accuracy.

4). Based on the numerical analysis, it can be found that the concrete strength, hollow ratio, and yield stress and diameter-to-thickness ratio of the outer steel tube significantly affect the initial stiffness, ductility, and ultimate strengths of the CFDST columns, while the yield stress and diameter-to-thickness ratio of the inner steel tube exhibit insignificant effect.

5). A novel strength prediction model is suggested to evaluate the cross-sectional resistances of CFDST columns, and a higher prediction performance is achieved for the proposed model than the existing design models.

Chapter 5. Fiber-beam element model for circular entire-section axially loaded CFDST short columns

1). The effect of concrete strength on its effective utilization rate is not considered in Liang's model and Tao et al.'s model, thus a large deviation is found when they predict the compressive behavior CFDST columns with HSC or UHSC.

2). The proposed FBE model can predict the compressive behaviour of circular CFDST short columns made with a wide-range of concrete strengths more accurately than the existing models.

LIST OF PUBLICATIONS

Journal papers

[1]. Yan-Gang Zhao, Xi-Feng Yan, Siqi Lin, Compressive strength of axially loaded circular hollow centrifugal concrete-filled steel tubular short columns, Engineering Structures 201 (2019) 109828.
[2]. Xi-Feng Yan, Yan-Gang Zhao, Compressive strength of axially loaded circular concrete-filled double-skin steel tubular short columns, Journal of Constructional Steel Research 170 (2020) 106114.
[3]. Xi-Feng Yan, Yan-Gang Zhao, Experimental and numerical studies of circular sandwiched concrete axially loaded CFDST short columns, Engineering Structures 230 (2021) 111617.
[4]. Xi-Feng Yan, Yan-Gang Zhao, Siqi Lin, Compressive behaviour of circular CFDST short columns with high- and ultrahigh strength concrete, Thin-Walled Structures. (Under revision)
[5]. Xi-Feng Yan, Yan-Gang Zhao, Siqi Lin, Haizhong Zhang, Confining stress path-based compressive strength model of axially compressed circular CFDST short columns, Thin-Walled Structures. (Under review)
[6]. Siqi Lin, Yan-Gang Zhao, Xi-Feng Yan, Theoretical model for axially loaded concrete-filled rectangular steel tube stub columns, Steel and Composite Structures. (Under review)
[7]. Siqi Lin, Yan-Gang Zhao, Zhao-Hui Lu, Xi-Feng Yan, A unified theoretical model for axially loaded concrete-filled steel tube stub columns with different cross-sectional shapes, Journal of Structural Engineering. (Under review)

International Conference:

[8]. Xi-Feng Yan, Overall buckling analysis on different formed circular steel tubular columns under axial compression, 2018 International Conference on Civil, Architectural and Environmental Engineering (ICCAEE 2018) (Wellington, New Zealand, 2018.12).
[9]. Xi-Feng Yan, Yan-Gang Zhao, Experimental investigation on longitudinal residual stress distribution of circular steel tube sections, 9th International Conference on Steel and Aluminium Structures (University of Bradford, UK, 2019.07).
[10]. Xi-Feng Yan, Yan-Gang Zhao, Strength design of circular hollow centrifugal concrete-filled steel tubular stub columns under central compression, 7th International Symposium on Reliability Engineering and Risk Management (ISRERM2020) (Beijing, China, 2020.11)

Domestic Conference:

[11]. Xi-Feng Yan, Yan-Gang Zhao, Overall buckling study on different formed circular steel tubular columns under axial compression, *Summaries of Technical Papers of Annual Meeting, AIJ 2018*, pp.,417-418, Tohoku.
[12]. Xi-Feng Yan, Yan-Gang Zhao, A simple formula for predicting compressive strength of circular HCCFST stub columns under axial compression, *Summaries of Technical Papers of Annual Meeting, AIJ 2019*, pp. 1323-1324, Tokuriku.

[13]. Xi-Feng Yan, Yan-Gang Zhao, A practical formula for predicting compressive strength of axially loaded circular CFDST short columns, *Summaries of Technical Papers of Annual Meeting, AIJ 2020*, pp.,1401-1402, Kanto.